Turbulence and vortex dynamics

Javier Jiménez

July 26, 2004

Preface

In the following notes each of the seven chapters corresponds approximately to a lecture of the course at the Polytechnique, but the presentation has been kept descriptive to provide a connected narrative of the essence of each particular topic. There is more material in the notes that what will be covered in the lectures, but this extra material should be seen as providing the context for the subject.

In addition to the main part of the text, set in type of normal size, each chapter contains several numbered comments and problems, some of them solved, scattered within the text and set in smaller type. Many of the important demonstrations and details are contained in them. This material is part of the notes, which are probably best read in two stages. A first time in which the problems are skipped, taking 'on faith' the references to the results contained in them, and a second one including them. The first reading will give the student a qualitative understanding of how the subject 'works', while the second one will provide him, or her, with the analytical tools to do calculations. The unsolved problems included in the text are generally simple applications of the techniques developed in the rest of chapter, and can be used by the student to test his or her proficiency. They also generally contain results which generalize the discussion in the text to other cases of interest. There is finally at the end of some chapters a set of supplementary exercises. They provide extensions of the course material for those who are interested in probing the subject a little beyond the scope of the course. It should not be necessary for the students to solve all of these during the course, but those tackling them would certainly benefit from their effort.

Each chapter is preceded by a summary specifying which are the most important ideas explained in it, in which sections they are contained, and how they relate to the rest of the course.

The bibliographical references are collected at the end of the notes. They consist of original works of historical importance, reviews of subjects which are only broached within the notes, sources for the data used in the figures, and textbooks either on turbulence or on other areas of fluid mechanics. At the end of the introduction to chapter 1 there are some comments on which of the latter may be the best choices for further study.

Madrid and Stanford, 2004.

Contents

Chapter 1

Introduction

Summary

These notes deal both with vortex dynamics and with the turbulent motion in fluids, with emphasis on the latter. The reason why the two subjects are brought together in a single course will become clear after chapters 2 and 3, which contain most of the material on vorticity. In the mean time, you should take on faith that the reason why turbulent flows behave as they do is because they contain vorticity, and that turbulence is impossible in irrotational flows.

The present chapter describes the phenomenological observations that define turbulent flows (in §1.1), and explains (in §1.3) how turbulence works. In this sense, those two sections contain the whole course. We will however find that turbulence, when taken in the context of classical mechanics, appears to constitute a 'mystery'. In fact it was considered to be one by some people for a long time. The mystery is 'explained' in §1.3, but only at the expense of introducing velocity fields which are everywhere continuous but nowhere differentiable.

That conclusion sets the stage for one of the recurrent themes of the present course. Turbulence can only be described by mathematical concepts which are somewhat different from those of classical mechanics, and some sections of the course are devoted to making those concepts understandable, and to showing that their apparently abnormal character is more a question of historical accident than of physical or mathematical necessity. Those 'cultural' sections are only indirectly related to fluid mechanics but, without them, turbulence could be interpreted as an isolated pathological behaviour of high Reynolds number flows. It is shown in §1.4 that this is not the case, and that many familiar systems undergo 'turbulent' transitions.

Sections §1.2 and §1.4 constitute the cultural component of this chapter. In the first one we introduce *fractals*, which are the best-known examples of continuous but nowhere smooth geometrical objects, and which are therefore close *analogs* of turbulent velocity fields. Such objects have been known for more than a century, but they were considered for a long time to be mathematical curiosities. One of the themes of mathematical physics in the twentieth century was the recognition that

objects such as these, fractals or the chaotic systems introduced in chapter 2, are in fact generic solutions of physical systems, and that the belief that they constitute anomalies came more from a tendency to study first those phenomena which could be easily explained than from the nature of the phenomena themselves.

Turbulence affords a good opportunity to introduce some of those non-classical mathematical tools, and we will use it at various points along the course. It is possible to carry most engineering computations involving turbulent flows without knowing about fractals or about chaos, in the same way that it is possible to do agriculture without understanding molecular biology, but sooner or later a case always arises in which classical intuition fails, and where at least an awareness of the underlying complications is useful in developing a proper solution procedure.

1.1 Turbulence

It is a matter of common experience that flows, if they are sufficiently fast, become disordered. Smooth, or *laminar*, motion can only be maintained when it is sufficiently slow or when it happens on a sufficiently small scale. Otherwise, as in the case of rivers or of the wind, it becomes unstable, and *turbulent* fluctuations appear. While many factors contribute to the onset of the instabilities, in the simplest case of an initially steady Newtonian incompressible fluid, the only parameters are the geometry and the Reynolds number,

$$Re = UL/\nu, \tag{1.1}$$

where U and L are characteristic velocity and length scales, and ν is the kinematic viscosity (Reynolds 1883). The transition threshold varies from $Re \approx 10$ for flows away from walls, to $Re \approx 10^3$ in cases, such as in pipes, where the presence of the wall tends to inhibit the fluctuations.

Instability and the resulting disorder are not the only defining properties of turbulence. It became clear around the middle of the nineteenth century that laminar and turbulent flows were distinct regimes which differed in other important respects. The experiments had been done at about the same time by Darcy (1854) and by Hagen (1854), who were interested, for engineering reasons, in the pressure drop of water in pipes and channels. The related problem of the drag of a body moving in a fluid had been a recurring theme of hydraulics throughout the previous century, and it was known that it had two components: one which varies approximately linearly with the velocity of the fluid, and another one which varies quadratically. A few years before, Hagen (1836) and Poiseuille (1846) had studied the flow along thin capillaries, and had shown that the linear component of the drag was proportional to a property of the fluid which they named the viscosity coefficient. What was shown in 1854 by Hagen and by Darcy was that the quadratic component of the drag of a body, and of the pressure drop in a pipe, was independent of the viscosity.

The problem is one of energy dissipation. When a body moves with velocity U and suffers a drag D, it transfers to the medium an energy per unit time UD. In a pipe the work is done on the fluid by the pressure drop.

Consider the Navier Stokes equations for an incompressible flow,

$$\partial_t \boldsymbol{u} + \boldsymbol{u} \cdot \nabla \boldsymbol{u} + \frac{1}{\rho} \nabla p = \nu \nabla^2 \boldsymbol{u}, \tag{1.2}$$

$$\nabla \cdot \boldsymbol{u} = 0,$$

where p and $\boldsymbol{u}$ are the pressure and the vector velocity, and ρ is the constant fluid density. Consider a length of pipe, of cross-sectional area A and volume V, for which the velocity profile has reached equilibrium. To obtain an evolution equation for the kinetic energy per unit mass, $K = |\boldsymbol{u}|^2/2$, we multiply equation (1.2) by $\boldsymbol{u}$ and integrate over V,

$$\partial_t \int_V K \, \mathrm{d}^3\boldsymbol{x} = \frac{-\Delta p}{\rho} \int_A u \, \mathrm{d}^2\boldsymbol{x} - \nu \int_V |\nabla \boldsymbol{u}|^2 \, \mathrm{d}^3\boldsymbol{x}. \tag{1.3}$$

If we now average over times which are long enough for us to neglect the fluctuations of the different integrals, the left-hand side of (1.3) vanishes. The pressure drop $-\Delta p$ acts then as a source of energy, which has to be dissipated by the viscous term. The results of Hagen and Darcy were therefore paradoxical, because they implied that, even if the energy dissipation per unit mass

$$\varepsilon = \frac{-\Delta p}{\rho V} \int_A u \, \mathrm{d}^2\boldsymbol{x} = \frac{\nu}{V} \int_V |\nabla \boldsymbol{u}|^2 \, \mathrm{d}^3\boldsymbol{x}, \tag{1.4}$$

was due to the viscous forces, it was independent of the viscosity coefficient. Both authors speculated that the anomalous dissipation was connected with the energy needed to sustain the irregular velocity fluctuations that were also observed in turbulent flows.

The extra dissipation due to turbulence is substantial and, at large Reynolds numbers, overwhelms that of a comparable laminar flow. An example is given in figure 1.1, which shows the pressure drop in laminar and turbulent pipes for the same volume flux, as a function of the Reynolds number. For a laminar pipe the velocity profile is parabolic, and the pressure drop per unit length is given by

$$c_f = -\frac{R}{\rho U_b^2} \frac{\partial p}{\partial x} = \frac{8}{Re}, \tag{1.5}$$

where R is the radius of the pipe, U_b is the bulk velocity, which is defined so that the volume flux is $\pi R^2 U_b$, and $Re = U_b R/\nu$ is the Reynolds number. It follows from (1.4) that the mean energy dissipation per unit mass can be expressed in terms of the friction coefficient c_f as

$$\varepsilon = -\frac{U_b}{\rho} \frac{\partial p}{\partial x} = c_f \frac{U_b^3}{R}. \tag{1.6}$$

The friction coefficients in figure 1.1 are therefore normalized energy dissipation rates. Figure 1.1 includes smooth and rough turbulent pipes, as well as the theoretical result for laminar ones. In smooth pipes c_f drops as the Reynolds numbers

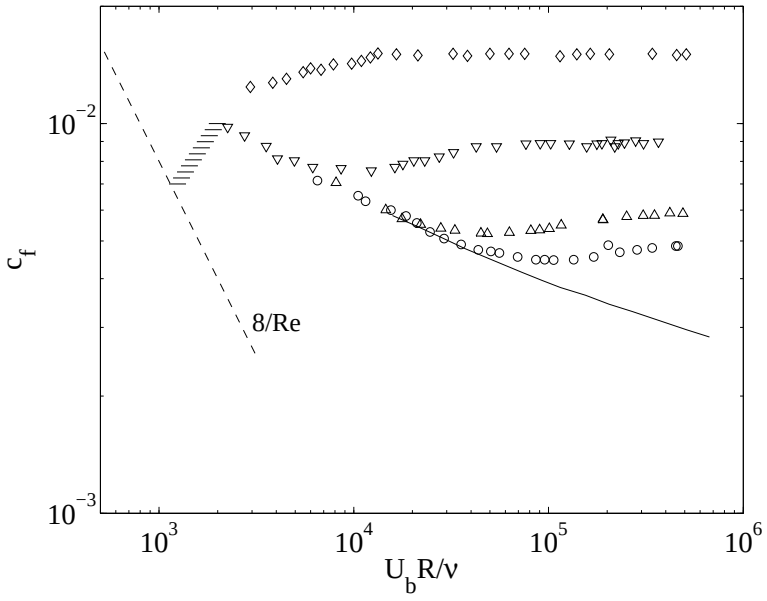

Figure 1.1: Friction coefficients in pipes as a function of the bulk Reynolds number. The solid line is for smooth pipes, while the symbols are for rough pipes in which the ratio of the radius to the roughness height is, from top to bottom, $R/k =$ 15, 60, 252, 507. The shaded area corresponds to transitional flows, while the dashed line to the left is equation (1.5) for laminar flow.

increases, although slower than in laminar ones, but in rough pipes it eventually becomes constant. This asymptotic behaviour is an example of the important, although empirical, property of fully turbulent flows that the energy dissipation rate becomes independent of the Reynolds number in the limit of vanishing viscosity. We will see in chapter 6 that the reason why the dissipation in smooth pipes does not reach a constant limit is that there is always a thin region near the wall where viscosity is important and which, although by no means laminar, is not really fully turbulent. Rough walls destroy this thin region, and the full pipe is turbulent.

Problem 1.1: Derive equations (1.5) and (1.6). The friction coefficient c_f is defined such that the shear stress at the wall is

$$\tau_w = \frac{1}{2} c_f \rho U_b^2.$$

The dissipation ε and the kinetic energy K define a decay time K/ε, which is the time in which the motion would be damped if there were no energy input. For rough pipes c_f is constant, and it follows from (1.6) that the characteristic turbulent decay time is proportional to $T_t = R/U_b$, while (1.5) implies that the laminar decay time is $T_\nu = R^2/\nu$. Note that T_t has the only dimensionally correct expression which does not involve viscosity. Laminar dissipation, on the other hand, is due to the molecular motions that are responsible for the viscosity. The macroscopic motion is not involved, and T_ν is the only dimensionally correct combination in which the macroscopic velocity U_b does not enter. The Reynolds number is the ratio

of both time scales,

$$Re = T_\nu / T_t. \tag{1.7}$$

Reynolds numbers are typically large, and wall-bounded flows are rarely fully turbulent below $Re \approx 100$. The relation (1.7) implies that the turbulent macroscopic velocity fluctuations are more efficient in dissipating energy than viscous diffusion, and that, in any turbulent situation, viscosity does not have time to act. The true turbulent limit is that in which $\nu \to 0$, but the exact expression (1.4) for the dissipation should remind us that this limit is not equivalent to $\nu = 0$, and that viscosity, although apparently irrelevant in turbulent flows can never be truly neglected.

Comment 1.2: Viscosity is due to the thermal agitation of molecules. Consider a (laminar) parallel flow in which the mean fluid velocity, U, is only a function of the transverse coordinate y. If the fluid molecules were all traveling at the mean velocity in the direction of the flow, there would be no way to transfer momentum among the different fluid layers, and the tangential stresses would be zero. The flow would be inviscid.

In a real fluid molecules also move randomly, with speeds of the order of the speed of sound c. This random motion is what transports momentum among adjacent layers, and what causes the viscous stresses. Consider for example a gas with N molecules per unit volume, each one of them of mass m. The molecules move on the average a distance λ_m before colliding with other molecules. Consider now two adjacent fluid layers separated by a distance λ_m. The velocity difference between those layers is $\Delta U = \lambda_m \partial U/\partial y$. Molecules leave one layer and move into the other before colliding and depositing a momentum increment which is due to this velocity difference. The number of particles crossing from one layer to the other per unit time and per unit area is Nc, and they transport an excess momentum flux

$$\tau \approx mNc\Delta U = mNc\lambda_m \, \partial U/\partial y = \rho c \lambda_m \, \partial U/\partial y,$$

where ρ is the fluid density. This momentum flux is the force transmitted between the two layers by viscosity, which can then be equated to the macroscopic definition,

$$\tau = \rho \nu \, \partial U/\partial y,$$

to give an expression for the kinematic viscosity coefficient,

$$\nu \approx c \lambda_m. \tag{1.8}$$

The Reynolds number can then be approximately expressed as

$$Re \approx \frac{U}{c} \frac{L}{\lambda_m}. \tag{1.9}$$

For air at ambient temperature and pressure the mean free path is of the order of 5×10^{-8} m, while the speed of sound is of the order of 300 m/s. The main reason why Reynolds numbers of macroscopic bodies tend to be high is because their dimensions are usually much larger than the mean free path, so that the second factor in (1.9) is very large, while the Mach number in the first factor, although typically small, is not small enough to compensate for it. For example, for the Reynolds number of a ball, 1 cm in diameter, to be of order unity, its velocity would have to be of the order of 1 mm/s, which corresponds to a Mach number $U/c \approx 10^{-7}$.

The reason why some Reynolds numbers are small, and why some flows are therefore laminar, is usually because the velocities are small, or because the dimensions are short. As shown in the next problem, however, there are cases of engineering interest in which macroscopic bodies have low Reynolds numbers because the mean free itself becomes large.

Problem 1.3: The mean free path is inversely proportional to the gas density (can you see why?). What does that imply for the motion of spacecraft in the upper atmosphere, where the mean air density becomes low and the mean free path becomes macroscopic?

Assuming that a spacecraft has a characteristic size of 20 m, and re-enters the atmosphere at a Mach number of 25, estimate at which height its Reynolds number increases above $O(1000)$, and turbulence begins to be important.

The three properties of disorder, instability and anomalous dissipation describe what we empirically understand by turbulent flows. The first part of the these notes will be devoted to exploring the interrelations among the three; for example, we will ask ourselves whether disorder is a necessary part of the dissipation mechanism, or whether either of those two properties are exclusive to Navier-Stokes turbulence. This investigation will force us to develop techniques to analyze irregular and 'anomalous' systems, which we will find to be quite common in nature.

Once we have gained in this way an understanding of the 'essence' of turbulence, the rest of the course will be devoted to the phenomenological description of the variety of turbulent phenomena found in fluid flows, to the discussion of their importance to other sciences and to technology, and to a brief description of methods for their computation.

These lectures cannot give a complete account of the wealth of phenomena found in turbulent flows. The reader should consult some of the many books on the subject for a more in-depth study. Two classical books are those by Townsend (1976) and Tennekes & Lumley (1972). The last one, in particular, is still probably the best elementary introduction to the subject. There are few comparable modern general books on turbulence. The ones that might best fit that description are the one by Lesieur (1997), and the first half of the book by Pope (2000). A book that may become classical is Frisch (1995), which deals almost exclusively with isotropic turbulence, and cannot therefore be considered as a general book of the subject. It contains one of the best modern descriptions of the fundamentals assumptions of turbulence theory, of its early historical development and, very especially, of the subject of small-scale intermittency.

There are two books which, despite their age, are still indispensable. The short monograph by Batchelor (1953), although lacking by now in reliable experimental data, is still the reference work for the mathematical theory of isotropic turbulence. The situation is similar for the book on boundary layers by Schlichting (1968) which, even if not dealing exclusively with turbulent layers, is still the best survey of their behaviour.

There are many excellent textbooks in general fluid dynamics that can be consulted by those looking for more information on vortex dynamics. Perhaps the two which are closer to the spirit of the present notes are the introductory textbook by Batchelor (1967) and the more advanced monograph by Saffman (1992).

1.2 Fractals

It follows from (1.4) that the only way that the dissipation may remain non-zero in the limit of vanishing viscosity is for the square-averaged velocity gradient

$$\frac{1}{V}\int_V |\nabla \boldsymbol{u}|^2 \,\mathrm{d}^3\boldsymbol{x}, \tag{1.10}$$

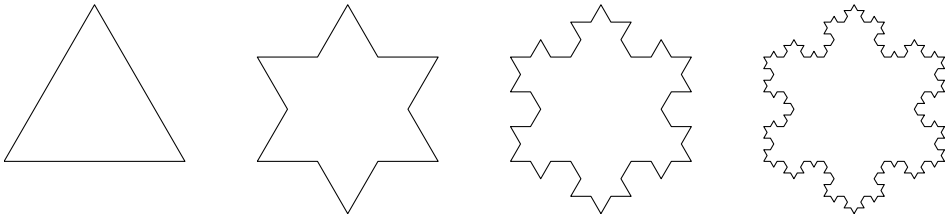

Figure 1.2: The first three iteration stages in the construction of a Koch flake with scaling factor $\beta = 1/3$. The dimension of the fractal limit would be $D = 1.2618\ldots$

to become infinite. The velocity field cannot then remain a differentiable function, and singularities must appear.

That some natural phenomena could have non-analytic descriptions was realized more than a century ago, and many examples of continuous but nowhere-differentiable functions were invented. The best known are geometrical fractals, popularized by Mandelbrot (1983) and Schroeder (1991). They are, for example, lines which enclose finite areas but which have infinite lengths, or sparse 'dusts' with an infinite number of elements, but whose volume is zero. An example of the construction of the first kind of fractal is given in figure 1.2. Begin with the triangle on the left of the figure, each of whose sides has length $\ell_0 = 1$, and whose perimeter is $L_0 = 3$, and substitute each side with four equal segments of length $\ell_1 = \beta\ell_0$. In the figure we have used $\beta = 1/3$, and the resulting line is a six-pointed star whose perimeter is $L_1 = 12\beta = 4$. If we iterate this procedure, substituting at every step each side, of length ℓ_n, with four segments of length $\beta\ell_n$, we get the increasingly complicated 'snowflakes' shown towards the right of figure 1.2. It is clear that, in the limit of an infinite number of iterations, the resulting line does not have a tangent anywhere, since there is a tiny 'peak' at every point. The length of the limiting line is infinite, although its area stays bounded [PROBLEM 1.5]. After n iterations, the line has $N_n = 3 \times 4^n$ sides, each of which has length $\ell_n = \beta^n$, so that the total length, $L_n = 3 \times (4\beta)^n$, increases without limit with n as long as $\beta > 1/4$.

One measure of the degree of complication of a geometrical fractal can be expressed as a 'dimension'. Consider a smooth line, such as the triangle in figure 1.2. If we divide it, for measurement purposes, into subsegments of length ℓ, the total number of segments needed to cover the line is $N_\ell = 3\ell^{-1}$. Similarly if we measure a smooth area with elements of diameter ℓ, we need a number of measuring elements which is proportional to $N_\ell \sim \ell^{-2}$. In both cases the exponent in the expression of the number of elements corresponds to the dimensionality of the figure, $D = 1$ for the line, and $D = 2$ for the surface. We have seen on the other hand that, to measure the fractal curve in figure 1.2, the number of rulers of length ℓ that we need behaves as

$$N_\ell \sim 4^n = \ell_n^{-D}, \qquad D = -\log 4/\log\beta \approx 1.26. \tag{1.11}$$

As in the two smooth cases mentioned above, we can interpret the exponent D as a 'fractal' dimension, which in the figure is intermediate between that of a line and that of an area. Fractal lines such as this one are more complicated than smooth

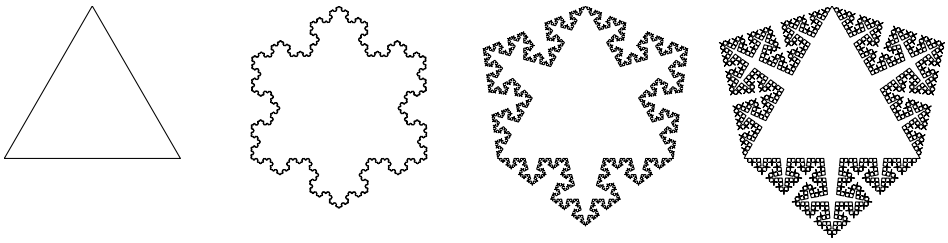

Figure 1.3: Four Koch flakes of increasing fractal dimensions. Each of them is shown after five iterations. A flake with D=2 would fill densely the area surrounding the initial triangle.

ones because, as one uses shorter measuring rulers, new details become relevant, requiring extra segments.

There are several definitions of fractal dimension, which are not always equivalent. The one that we have used here (the Kolmogorov capacity) is perhaps the simplest. For any set in a metric space, it is formally defined as the exponent of the minimum number, $N_\ell \sim \ell^{-D}$, of 'balls' of diameter ℓ which are needed to cover the set.

It has a probabilistic interpretation that is often useful in analyzing complex systems. Assume that one tries to find a set by the random application of a probe of resolution ℓ, and that the dimension of the imbedding space is D_0. For example, $D_0 = 3$ for sets in space, and $D_0 = 2$ for sets on a plane. One would need $N_0 = \ell^{-D_0}$ probe applications to scan the whole space, but only $N_\ell = \ell^{-D}$ of them will intersect the set. The probability of finding a member of the set with any given measurement is then

$$\frac{N_\ell}{N_0} \sim \ell^{D_0 - D}, \tag{1.12}$$

which is controlled by the difference $C = D_0 - D$ of the two dimensions, called the 'codimension'. The fractal codimension therefore determines how the probability of finding a set changes with the resolution. Alternatively, ℓ^C represent the fraction of the total volume that is filled by the set when it is uniformly 'thickened' to size ℓ.

If we consider a fractal whose dimension is the same as that of the imbedding space, such as the interior of a circle in the plane, the probability of finding it with a single observation is approximately independent of the resolution, and is $O(1)$. A smooth line, with $D = 1$, becomes harder to find within the plane as the probe becomes smaller, but the probability of finding it decreases more slowly than that of finding a single point whose dimension is $D = 0$. The difficulty of finding the Koch flake in figure 1.2 is between those of finding a smooth line and a surface patch.

By varying the scaling ratio β we can construct Koch flakes with different fractal dimensions, such as those in figure 1.3. When $\beta = 1/2$ the dimension (1.11) becomes $D = 2$, equal to that of the imbedding plane, and the resulting line is

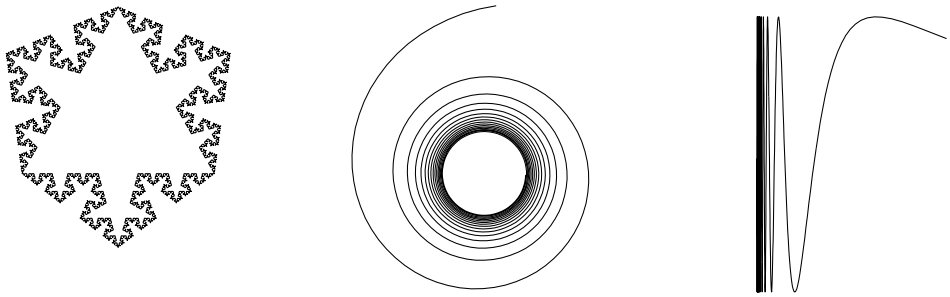

Figure 1.4: The three lines in this figure all have fractal dimension $D = 1.5$, although they look very different. Only the first few iterations of the Koch flake, or the first few oscillations of either the spiral or the oscillating line are drawn.

complicated enough to densely fill an area. For $D > 2$ the probability of finding the line *increases* as the probe becomes smaller. This can only be true if the line intersects itself, so that it an infinite number of sides go through some points of of the plane[1]. This argument shows that it is impossible to construct a non-self-intersecting object whose fractal dimension is larger than that of the imbedding space.

It is possible to imagine fractals in which the singularity is concentrated in a single point, instead of distributed more of less uniformly. This is for example the case with some spirals, whose length is infinite because they have infinitely many turns near the centre, but which are otherwise smooth [PROBLEM 1.6]. Other fractals may also look very different from those in figure 1.3, but still be fair representations of physical processes. Consider the accumulating oscillation defined by

$$y = \sin x^{-\alpha}, \qquad 0 \leq x < 1, \tag{1.13}$$

whose Kolmogorov capacity is $D = (2\alpha + 1)/(\alpha + 1)$ (can you prove it?). A Koch flake, a spiral and a line such as (1.13) are given in figure 1.4, which has drawn so that the three have the same fractal dimension. Examples such as these illustrate that the dimension characterizes only one aspect of a non-analytic set, and that the understanding of a singular phenomenon must take into account the full description of its singularities. Curves similar to Koch flakes appear in nature in such phenomena as crystal growth, from where they take their name, and in unstable surfaces such as flames. Accumulation points and lines are more commonly associated with the deformation of interfaces by complicated flows, such as turbulent ones, where they are important in promoting mixing by bringing different fluids into intimate contact. A discussion of the latter application can be found in Ottino (1989).

The fractal figures that we have discussed in this section are self-similar, by which it is meant that their construction rules look the same independently of the scale at which they are initiated. In the Koch flake, for example, the rules for

[1]Note that the rules for computing probabilities have to be changed in this case so that each individual side is counted as different when several of them are found overlapping each other.

segmenting one part of the curve are independent of its length, since everything is expressed in terms of fractions. A small part of the limiting curve would look identical to a larger one if it were scaled to the right overall dimension. Power laws such as (1.11) are characteristic of problems that have no intrinsic scale, and they are the hallmark of self-similarity. This can be proved quite generally and is not limited to geometrical fractals. Assume that a variable N is a function of another one ℓ. The example that we have encountered here is the number of sides at a given length scale, but the two variables could be anything else. The only assumption is that there are no natural units for any one of them, so that applying a scaling transformation to one of the variables results at most in a scaling transformation for the other. Formally, if we define λ as the scale chosen for ℓ, we can write

$$N(\ell) = A(\lambda)F(\ell/\lambda), \tag{1.14}$$

and scaling invariance means that the left-hand side of the equation should be independent of λ. Differentiating (1.14) with respect to λ and particularizing to $\lambda = 1$, we obtain the differential equation

$$A(1)\,\ell F'(\ell) = A'(1)F(\ell), \tag{1.15}$$

where the primes stand for derivatives, and which integrates immediately to the power law

$$F(\ell) \sim \ell^{A'(1)/A(1)}. \tag{1.16}$$

We will later have occasions to use arguments of this type to derive other similarity laws.

In reality no physical process can be fully self-similar. There are always scales which are relevant, even if only the size of universe and some atomic constant, but many processes have self-similar *ranges* in which lengths (or other variables) are small with respect to a large *(outer)* scale, and large with respect to a small *(inner)* one, so that the influence of both of them can be neglected. In the Koch flakes discussed above the size of the initial triangle is the relevant outer scale, and the length of sides in the last iteration is the inner one. Power laws such as (1.11) only work when ℓ is far from both limits.

In analogy to our definition in (1.7) of the Reynolds number as the ratio between the two time scales of a turbulent flow, we can introduce a 'Reynolds number' for any self-similar process as the ratio between its outer and its inner scales.

1.3 The self-similar energy cascade

While we have used geometric fractals in the previous section to introduce the concept of self-similarity, it should be clear that the same concept can be applied to more general situations. We cannot then use fractal dimensions, which are purely geometrical concepts, but we can expect power laws, and the place of the dimension is taken by the *scaling exponents*. Our purpose in this section will be to compute the scaling exponents that characterize the singularities of the turbulent velocity field.

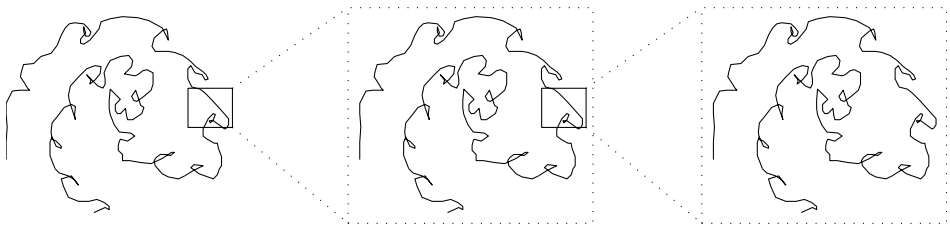

Figure 1.5: A self-similar cascade of eddies in a turbulent flow.

Note however that, as in the case of geometric fractal, such an exponent is at best only a partial representation of the structure of the velocity.

That the turbulent velocity was self-similar was first proposed by Richardson (1922), who imagined that large turbulent eddies, generated by the external forces acting on the flow, would become unstable and break into smaller ones, which would in turn break again, until the the eddies became small enough to be damped by viscosity. The implication was that the break-up process was self-similar for scales which were much smaller than the size of the large-scale forcing, but larger than some viscous limit (Figure 1.5).

Kolmogorov (1941) introduced the concept of an energy cascade, and computed the scaling exponent. He argued that the role of the break-up process is to transfer energy from the large scales, where it can not be dissipated, to the smaller ones where it can. Energy is injected by the forces into the largest eddies, whose Reynolds number is large if the flow is turbulent, and is transferred to the eddies that result from their break-up. This process is inviscid and no energy is dissipated, but the eddies become smaller with every cascade step and so do their Reynolds numbers. Eventually, the energy reaches an eddy size for which viscosity cannot be neglected any longer, and the right-hand side of equation (1.3) becomes appreciable. It is only at that stage that the energy is dissipated. The hypothesis of Kolmogorov is that the cascade is essentially one-directional, self-similar and uniformly distributed over the flow. Energy is predominantly transferred from larger to smaller eddies, and the flux of energy is independent of the eddy size at which it is measured.

These assumptions are enough to find a scaling exponent for the velocity and to estimate the inner viscous length where self-similarity ceases to hold. Label an 'eddy' by a velocity difference u_ℓ across a distance ℓ, leaving precise definitions for latter chapters. The argument depends only on scaling similarity, which is essentially the same as dimensional analysis, and is therefore independent of the details of how the velocities are measured. The kinetic energy per unit mass of the eddies of size ℓ is proportional to u_ℓ^2, and decays in a time which, in the absence of viscous effects, can only be of order $T_\ell = \ell/u_\ell$. The rate at which energy is transferred in the break-up process is then proportional to

$$\varepsilon \sim \frac{u_\ell^2}{T_\ell} = \frac{u_\ell^3}{\ell}. \tag{1.17}$$

For equilibrium flows, this quantity is the same as the rate of energy dissipation

that we have encountered above, when discussing viscosity dissipation, since the assumption is that the energy cannot reach the viscous scales unless it is transported there by the inviscid cascade. We are also assuming that the statistics of the flow vary slowly enough for the energy transfer rate ε to be independent of ℓ. Otherwise the energy could accumulate at some intermediate eddy size. Equation (1.17) then leads directly to a power law for the velocity increments,

$$u_\ell \sim (\varepsilon \ell)^{1/3}. \tag{1.18}$$

We will explore the consequences of this formula in chapter 5. We will just note here that it allows us to estimate the order of magnitude of the inner 'cutoff' scale for the self-similar range. We have assumed that the time scale of the decay of an eddy is ℓ/u_ℓ, which should be faster than the viscous decay time ℓ^2/ν. This is true as long as the Reynolds number of the eddy $u_\ell \ell/\nu$ is large, but it follows from (1.18) that this number decreases as the cascade proceeds to smaller sizes, until it becomes of order unity when

$$u_\ell \ell/\nu \approx 1, \qquad \ell \approx \eta = (\nu^3/\varepsilon)^{1/4}. \tag{1.19}$$

The velocity difference across these 'Kolmogorov' eddies is

$$u_K = (\varepsilon\eta)^{1/3} = (\varepsilon\nu)^{1/4}. \tag{1.20}$$

For large eddies equation (1.18) implies that the velocity 'gradient' u_ℓ/ℓ increases as ℓ decreases. There is no limit that can be interpreted as a derivative as long as $\ell > \eta$, which is the essence of our previous claim that the turbulent velocity field was singular everywhere. For distances shorter that this Kolmogorov scale, viscous forces dissipate the eddies before they have time to decay into smaller ones, and the flow is smooth. As the viscosity is made to vanish, the Kolmogorov scale tends to zero, and the velocity really becomes singular.

In general we can only say that, for eddies which are small enough for the effect of the large-scale forcing to be negligible,

$$u_\ell/u_K = F(\ell/\eta), \tag{1.21}$$

where F is some function that tends to $(\ell/\eta)^{1/3}$ when $\ell/\eta \gg 1$. It is in this latter range that the velocity field is fractal, although not a geometrical fractal in the sense of the previous section. The ratio between the size of an eddy and the Kolmogorov scale,

$$\frac{\ell}{\eta} = \frac{\ell}{(\nu^3/\varepsilon)^{1/4}} = \left(\frac{u_\ell \ell}{\nu}\right)^{3/4}, \tag{1.22}$$

can be expressed as a power of its Reynolds number. In the case of the eddies generated by the large-scale forcing, their Reynolds number determines the scale ratio across the self-similar range. Because viscous forces are not important in this range, these scales are usually called 'inertial'.

We have made several assumptions in deriving the results in this section. We have for example assumed that the energy cascade is uniformly distributed in space,

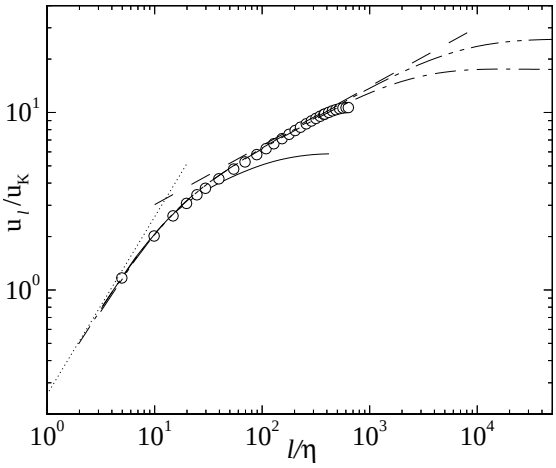

Figure 1.6: Root-mean-squared longitudinal velocity differences for several turbulent flows, displayed in Kolmogorov scaling. The dashed straight line is the self-similarity power law (1.18), and the dotted line to the left is the linear dependence $u_\ell \sim \ell$, which characterizes differentiable flows. The longer experimental lines correspond to higher flow Reynolds numbers.

which implies that the flow is disordered enough for the energy to be more or less uniformly distributed, and that an equilibrium cascade exists. Also, even if the only possible time scale for the inviscid decay of the eddies is ℓ/u_ℓ, we have not shown that there is a break-up mechanism that is able to act in that time scale. At present the only support for these assumptions is that experimental results agree with their consequences, as is shown in figure 1.6, but there is no adequate theoretical proof that the the same results could not be achieved in a different way. In fact the simple cascade model introduced here is known to be only an approximation, even if it happens to be a good one for three-dimensional incompressible isotropic turbulence. There are important cases in which one or another of the above assumptions fail and, in some of them, so do the conclusions that we have derived from them.

Comment 1.4: Although it is true that other cascades are possible, once we accept the basic experimental fact that the energy dissipation rate ε is independent of viscosity, many of the functional forms derived in this section become dimensional necessities.

Consider for example the velocity difference u_ℓ across a distance ℓ which is small enough for the overall dimensions of the system to be unimportant. Once we accept that different turbulent flows are distinguished by the magnitude of ε, and that the details of the large scales cannot influence the behaviour at scale ℓ, the only possible dimensionless group is

$$\frac{\varepsilon\ell}{u_\ell^3},$$

which cannot depend on anything, and therefore has to be a universal constant. This leads directly to (1.18). Note that this dimensional argument is equivalent to the similarity analysis in (1.16).

If we next want to estimate at which distance viscosity becomes important, and we assume that it can only depend on ε and ν, the only dimensionally correct combination is (1.19).

1.4 Other fractal processes in physics

The previous discussion would be interesting even if it only applied to turbulence in fluids, since most macroscopic flows are turbulent, and turbulence is therefore extraordinarily important in the natural sciences and in technology. But it turns out that the appearance of a non-analytic range of scales is actually a common response of physical systems to strong forcing, and not an exclusive property of the Navier–Stokes equations. We can interpret in this way the transition to turbulence in fluids. Assume that we have a smooth flow in a container, and inject energy into it by stirring with a paddle of size L at velocity U. The force on the paddle[2] is $F = O(\rho U^2 L^2)$, and the energy transferred to the fluid by unit time and unit mass is $\varepsilon = FU/\rho L^3 = O(U^3/L)$. If we now assume that the flow is smooth, the velocity gradients are $O(U/L)$, and the energy that the viscous forces can dissipate is $\varepsilon_\nu = O(\nu U^2/L^2)$. The ratio between the two, $\varepsilon/\varepsilon_\nu = UL/\nu$, is the Reynolds number and, as soon as the latter is large, viscosity cannot directly get rid on the energy that is being injected. The transition to turbulence is the response of the system to this extra energy by creating gradients that allow viscosity to do its job.

There are many other examples of fractalization in strongly forced systems. Perhaps the most familiar is the fracture of solids. When we inject an energy E into a brittle solid of diameter L, for example by hitting it, most of the energy goes into elastic deformation waves, and is eventually dissipated into heat. As in the case of viscosity, elastic deformation has its limits and, if enough energy is injected, molecular bonds break and the body fractures. Breaking bonds is equivalent to creating new surface area, and the energy absorbed in that way is $\sigma \Delta A$, where σ is the surface tension and ΔA is the area that has been created. If the body breaks into n pieces its volume is conserved, and the diameter of each piece is $L_n = Ln^{-1/3}$. The surface of the fragments is $nL_n^2 = L^2 n^{1/3}$. Equating the surface energy to the forcing we can estimate that $n \approx (E/\sigma L^2)^3$. The size of the final pieces and the total area of the broken body are then

$$L_n = \frac{L^3 \sigma}{E}, \qquad A_n = \frac{E}{\sigma}. \tag{1.23}$$

In the limit of infinite energy the body is reduced to dust, and its area becomes infinite. The process is similar to that in turbulent flows. Weak forcing can be dissipated while the system retains smoothness but, if the forcing is increased beyond the point in which this ceases to be possible, the system responds by fractalizing and creating singular mechanisms to accommodate the higher input. In this sense flows become turbulent because, beyond a certain energy input, they 'break'.

Other examples of fractalization are not necessarily destructive. Living beings, for example, need oxygen to generate the energy that they use. In the absence of other mechanism this oxygen reaches the interior of the body by diffusion through the skin. As the system becomes larger its oxygen requirements increase approximately as its volume, while the diffusion flux, which is proportional to the area and to the concentration gradient, increases only as its linear dimension. It can be shown

[2] This drag formula only assumes that the flow is separated, not that it is turbulent.

that this would limit the size of living beings to at most a few millimetres. Larger beings, like ourselves, have developed fractal exchange mechanisms, like vascular circulation, branching lungs or the leaves of trees, to handle the diffusion of gases. The two books cited above by Mandelbrot (1983) and Schroeder (1991) give other examples. It may be said that the reason why fractals, geometric or otherwise, are prevalent in nature is the need of handling solicitations that cannot be managed by smooth means.

SUPPLEMENTARY PROBLEMS

Problem 1.5: Show that the area enclosed by the Koch flakes discussed in figures 1.2 and 1.3 is

$$S = \frac{\sqrt{3}}{4}\left[1 + \frac{(12\beta - 3)^{1/2}}{2\beta + 1}\right].$$

Show that only the range $\frac{1}{4} \leq \beta \leq \frac{1}{2}$ makes geometric sense. What happens above and below that range? Show that any Koch flake for which $\beta > \frac{1}{2}$ is self-intersecting.

Problem 1.6: Show that the Kolmogorov capacity of the spiral defined in polar coordinates by

$$r = \theta^{-\alpha}, \qquad \theta > 0,$$

is $D = 2/(1 + \alpha)$, if $0 \leq \alpha \leq 1$. Justify these limits for α.

Hint: compute the radius below which a measuring circle of radius ℓ overlaps more than one neighbouring turn of the spiral, and approximate the length of tight spiral turns by that of circles.

Chapter 2

Vorticity and the origin of chaos

Summary

We have seen in the previous chapter that turbulent flows are complex, and we implicitly used that idea in describing the cascade in terms of 'typical' or 'average' eddies. That description only makes sense for systems in which elements take most possible configurations at some moment of their evolution. Their state can then, for many purposes, be described in terms of statistical properties, such as averages. Very ordered systems do not behave in that way, and their statistical description can lead to serious errors. Think for example of representing the position of the Earth by its mean value, which is somewhere in the vicinity of the Sun.

The present chapter does two things. In the first place it studies vorticity in a two-dimensional flow. This is important by itself, even independently of turbulence, because vorticity is an expression of the angular momentum of the fluid, and angular momentum, being a conserved quantity, determines in large part how the fluid moves.

The restriction to two-dimensional flows is artificial, and its effects can be very significant. Most flows of practical interest are three-dimensional, and vorticity behaves very differently in three dimensions than in two. The full equations for the evolution of three-dimensional vorticity will be given in the next chapter, but it is easier to analyze them in two stages, and what we learn here will help us later to understand the three-dimensional effects.

The second goal of this chapter is to understand how chaos originates in fluid dynamics. The Navier-Stokes equations are deterministic. They are essentially a restatement of Newton's law that force equals mass times acceleration, and it was not understood for a long time how such deterministic equations could give rise to the apparently 'unpredictable' turbulent flows. In fact some people felt that there was something incomplete in the Navier–Stokes approximation, and that extra terms were needed that would eventually account for the randomness.

The resolution of this apparent paradox is one of the success stories of twentieth-century mathematics. It turns out that unpredictability and chaos are common properties of most systems with many interacting degrees of freedom which, for a fluid, are intuitively the positions and velocities of its many 'particles'. The key is

the nature of the 'interactions', and it is for this reason that vorticity and chaos are brought together in the same chapter. It will become apparent below that turbulence is the behaviour of flows which become chaotic because they contain vorticity. An example of how this happens is developed in some detail in §2.4, which can be considered as a more 'cultural' section than the others in this chapter.

Vorticity, as developed in §2.1 to §2.3 and in chapter 3, is the key fluid-dynamical object used to describe turbulence, and as such it is crucial for the rest of the course. The origin of chaos in dynamical systems, as explained in §2.4, is less directly related to turbulence, and is not usually needed for the engineering computation of turbulent flows. But it is at the physical and mathematical roots of why turbulence exist, and is something that should be understood by anybody with a general interest in how the World works. In the same way that fractals, and the other non-analytic objects described in the last chapter, are some of the things that distinguishes twentieth-century geometry from its nineteenth-century predecessor, the appearance of chaos in deterministic systems plays much of the same role with respect to dynamics.

2.1 The origins of complexity in fluid mechanics

Not all flows are chaotic, even at the high Reynolds numbers characteristic of turbulence. Irrotational incompressible flows, for example, are simple. In them the velocity derives from a potential,

$$\boldsymbol{u} = \nabla\phi, \tag{2.1}$$

and the incompressibility condition can be written as

$$\nabla \cdot \boldsymbol{u} = \nabla^2\phi = 0. \tag{2.2}$$

These flows are therefore governed by Laplace's equation, whose solutions are smooth, and where the time dependence is not explicit. If the boundary conditions are stationary, so is the flow. Even when they are not, the flow is at any time the smoothest possible field which is consistent with the instantaneous boundary conditions. Incompressible potential flows can be understood as a series of unconnected snapshots, rather than as truly evolving systems. No chaos is possible in them.

There are many ways in which such simple behaviour can be broken. The first one is for the flow not to be incompressible, which leads to acoustics. The second one is for it not to be irrotational, which leads to turbulence. The effect of vorticity is most easily understood in two dimensions. Consider incompressible flow in the plane $(x,\, y)$. The velocity can be derived from a stream function ψ,

$$\boldsymbol{u} = [u,\, v] = [\partial\psi/\partial y,\, -\partial\psi/\partial x], \tag{2.3}$$

which automatically enforces continuity. The vorticity has a single non-zero component which can be expressed in terms of the stream function as

$$\omega = \frac{\partial v}{\partial x} - \frac{\partial u}{\partial y} = -\nabla^2\psi. \tag{2.4}$$

Its evolution, found by taking the curl of the momentum equation, is

$$\frac{\partial \omega}{\partial t} + \boldsymbol{u} \cdot \nabla \omega = \nu \nabla^2 \omega, \tag{2.5}$$

which, in the inviscid limit, reduces to

$$\mathrm{D}_t \omega = 0, \tag{2.6}$$

where D_t is the total derivative. This equation states that the vorticity of an inviscid constant-density fluid is conserved along trajectories.

The general mechanism of the flow is then that the vorticity is transported by the velocity, while the resulting vorticity distribution determines the velocity through Poisson's equation (2.4). Evolution and instabilities are possible because of this feedback, and the flow depends not only on the boundary conditions, but on its history.

There are many other ways of introducing complexity in a flow. Broadly speaking, what is needed is some property which is modified by the flow and whose distribution in turn modifies the flow.

We have already mentioned that compressibility, which is the interplay between internal energy and density, gives rise to acoustics. Another example is the flow around flexible structures, which often becomes unstable, as in the familiar case of flapping flags. Stratified flows, in which the 'active' interaction is between density differences and gravity, result in propagating interfacial waves.

The types of breakdown induced in each of those examples are different. We have seen that a good description of what happens if we force too strongly a vortical flow is that it creates distributed singularities where energy is dissipated independently of the magnitude of the viscosity. Acoustics responds differently. If a compressible fluid moves too fast around an obstacle, it forms shock waves. Those are localized two-dimensional singularities in which energy dissipation is also independent of viscosity [PROBLEM 2.8] but, in contrast to the more or less space-filling cascade of turbulence, there are typically only a few shocks in a given flow. Water waves, on their part, break when they are too high, and a choppy sea is full of whitecaps, each of which is an energy-dissipating 'point' singularity.

There is no universal way in which systems respond to strong forcing, even if we saw in the last lecture that they in general lose smoothness. If we want to go beyond broad generalities we have to understand how particular systems work and, for turbulence, that means understanding the behaviour of vorticity.

2.2 Vorticity in two dimensions

Equations (2.3) to (2.5) describe the evolution of an incompressible vortical two-dimensional flow. The first two are kinematic, and describe how the velocity is determined by the vorticity. They can be inverted to give an integral representation of the velocity,

$$\boldsymbol{u} = \frac{1}{2\pi} \iint \omega(x', y') \, \frac{[y' - y, \, x - x']}{(x - x')^2 + (y - y')^2} \, \mathrm{d}x' \, \mathrm{d}y' + \nabla \phi, \tag{2.7}$$

which is known as the Biot-Savart law. The kernel multiplying the vorticity in the integral can be interpreted as the velocity generated by a 'point vortex', and the integral expresses that the effects of the different vortices add linearly. There is in general a potential component, $\nabla\phi$, that is not directly determined by the vorticity, and which represents the effects of the walls and of the velocity at infinity. This component is not important in the absence of nearby boundaries, but it can become the dominant one in confined flows.

Comment 2.1: A useful way of studying two-dimensional irrotational flow is to introduce a complex spatial variable $z = x + \mathrm{i}y$. Because the velocities in irrotational flow derive from a potential which satisfies Laplace's equation, it is possible to represent that potential as the real part of a complex analytic function of $\Phi(z)$. It then follows from the Cauchy-Riemman relations that there is a complex 'velocity',

$$w = u - \mathrm{i}v = \frac{\mathrm{d}\Phi}{\mathrm{d}z}, \tag{2.8}$$

which is also an analytic function of z. Note the complex conjugation in the definition of w. Because the potential does not exist at those points at which the vorticity is not zero, vortices appear as singularities of both Φ and w.

The Biot-Savart law (2.7) can be written in this representation as

$$w(z) = \frac{1}{2\pi\mathrm{i}} \iint \frac{\omega(z')}{z - z'} \,\mathrm{d}x' \,\mathrm{d}y', \tag{2.9}$$

and the velocity field due to a point vortex of circulation γ located at z' is

$$w(z) = \frac{\gamma}{2\pi\mathrm{i}(z - z')}. \tag{2.10}$$

By expanding the kernel inside the integral in (2.9) as a Taylor series in $z' - z_g$, where z_g is some representative point inside a vortex 'blob', we can write a series expansion for the velocity in terms of the geometrical moments of the vorticity distribution,

$$w(z) = \frac{\gamma}{2\pi\mathrm{i}} \sum_m \frac{\Gamma_m}{(z - z_g)^{m+1}}, \tag{2.11}$$

where the circulation is

$$\gamma = \iint \omega(z) \,\mathrm{d}x \,\mathrm{d}y. \tag{2.12}$$

and the 'multipole' coefficients,

$$\Gamma_m = \frac{1}{\gamma} \iint \omega(z)(z - z_g)^m \,\mathrm{d}x \,\mathrm{d}y, \tag{2.13}$$

are geometrical properties of vorticity distribution. It is easy to see that $\Gamma_0 = 1$, and that Γ_1 can be made to vanish by choosing the point z_g to be the 'centroid' of the vorticity,

$$z_\gamma = \frac{1}{\gamma} \iint \omega(z) z \,\mathrm{d}x \,\mathrm{d}y \quad \Rightarrow \quad [x_\gamma,\, y_\gamma] = \frac{\iint [x,\, y]\, \omega \,\mathrm{d}x \,\mathrm{d}y}{\iint \omega \,\mathrm{d}x \,\mathrm{d}y}. \tag{2.14}$$

This is the basis for the 'point vortex' idealization (2.10), which is a singular vorticity distribution with zero radius but non-zero circulation, and which appears as the first term of the expansion (2.11). The velocity distribution in the far field of a single vorticity blob can then be approximated by the effect of a point vortex of the same circulation, located at its centroid, and decays as $|z - z_\gamma|^{-1}$. The next term in the expansion is $\gamma\,\Gamma_2/|z - z_g|^3$, where $\Gamma_2 = O(a^2)$ measures the ellipticity of the vortex [PROBLEM 2.2], and a is a measure of the vortex radius. This dipole correction becomes negligible when the distance to the vortex is $|z - z_g| \gg a$.

If the vorticity is concentrated in several blobs which are far away from each other, the velocity at any point which is not too close to any one of them can be approximated by the sum of the velocities induced by the point vortices which represent the individual blobs.

Problem 2.2: Show that the dipole coefficient for a vortex whose uniform vorticity is contained within the ellipse

$$\frac{x^2}{a^2} + \frac{y^2}{b^2} = 1,$$

is

$$\Gamma_2 = \frac{a^2 - b^2}{4},$$

and vanishes for a circular vortex patch. Show also that all the Γ_m with $m > 1$ vanish for a circular patch, which therefore acts exactly as a point vortex at distances greater than its radius.

The property mentioned at the end of the previous problem, that uniform circular vortex patches are *exactly* equivalent to point vortices when seen from the outside, generalizes to arbitrary axisymmetric vorticity distributions. If there are no other vortices or boundaries to break the symmetry, the velocity field is also axisymmetric. Define polar coordinates (r, θ) and velocity components u_r and u_θ. It follows from Stokes' theorem that the circulation around any circle enclosing the vortex is equal to the integral of the enclosed vorticity

$$2\pi r u_\theta = \gamma = 2\pi \int_0^r r\omega(r)\,\mathrm{d}r, \qquad u_r = 0. \tag{2.15}$$

The result for the radial velocity follows from continuity. A consequence is that, as soon as we move beyond the vortex itself, the velocity field becomes independent of how the vorticity is distributed, and depends only on the total circulation. We saw in comment 2.1 that this is also approximately true for vorticity distributions which are not axisymmetric, and that far enough from its centroid the velocity induced by a vortex blob always behaves approximately as γ/r.

For this approximation to be useful we need the make sure that compact vorticity blobs remain compact and relatively circular as they move. Equation (2.5) describes how vorticity moves, and we have seen that, in the absence of viscosity, it is simply advected without change. It is then clear that, if the velocity changes only slightly across a vortex blob, the vortex will keep its shape for long times, and it will move as an essentially rigid object with a velocity which is approximately that of the flow at its centroid. We may think that this would be the situation if vortices are far from each other, since the velocity field that they induce on each other would then be smooth. In fact, that is never true.

The problem is the effect of the vortices on themselves. It follows from (2.15) that the velocity due to a vortex whose characteristic vorticity and radius are Ω and R, is of the order of γ/r, where r is the distance to its centroid and $\gamma \sim \Omega R^2$ is the circulation. The gradient of that velocity is $|\nabla \boldsymbol{u}| \sim \gamma/r^2$. The dimensionless parameter which characterizes the nonuniformity of the velocity field with respect to a vortex blob is the ratio between the magnitude of the velocity gradient and of the vorticity, $S^* = |\nabla \boldsymbol{u}|/\Omega$, which should be small for the vortex to behave as if the flow were uniform. When considering the effect of a vortex γ_1 on another one, γ_2, we can estimate that strain parameter as

$$S^*_{12} \sim \frac{\gamma_1/r_{12}^2}{\Omega_2} \sim \frac{\gamma_1}{\gamma_2}\,\frac{R_2^2}{r_{12}^2}, \tag{2.16}$$

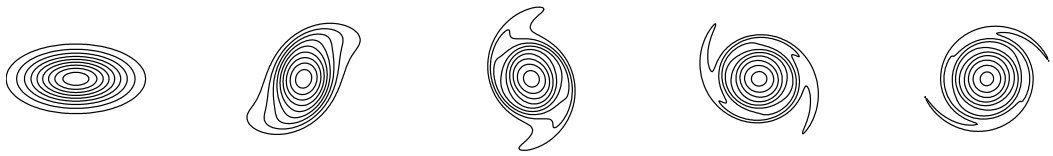

Figure 2.1: Evolution of an initially elliptic Gaussian vortex, as it circularizes under its own induction. Time is from left to right. $\gamma/\nu = 1.2 \times 10^4$.

so that comparable vortices perturb each other weakly if their distance r_{12} is large with respect to their radii. On the other hand, it follows from the same equation that $S_{11}^* \sim 1$, and that a vortex always perturbs itself strongly.

The reason why, in spite of this, the point vortex model is a useful approximation, is that circular vortices are exact equilibrium solutions of the inviscid equations so that, even if the effect of the vortex on itself is strong, it does not result in any distortion. If the vorticity and velocity distributions are axisymmetric, the inviscid vorticity equation becomes

$$\frac{\mathrm{D}\omega}{\mathrm{D}t} = \frac{\partial\omega}{\partial t} + u_r\frac{\partial\omega}{\partial r} + \frac{u_\theta}{r}\frac{\partial\omega}{\partial\theta} = \frac{\partial\omega}{\partial t} = 0. \tag{2.17}$$

In essence, a circular vortex induces on itself a very fast rotation but, since it is perfectly circular, it rotates on itself.

When the initial vorticity distribution is not exactly circular this self-induced rotation tends to circularize it, although some vorticity is generally lost in the process, as filaments and other debris (see figure 2.1). The end result is that, when a two-dimensional flow is initially seeded with a random vorticity distribution, it organizes itself after a while into a system of roughly circular independent cores.

There are several processes by which this happens. An specially important one is the break-up of a nonuniform vortex layer. Consider an infinitely-long uniform layer of vorticity $\omega = \omega(y)$, whose velocity field is found by integrating the kinematic equations,

$$\frac{\partial u_x}{\partial y} = -\omega, \qquad u_y = 0. \tag{2.18}$$

It follows that the velocity jump across the layer is its circulation per unit length, $\Delta u = \Gamma = \int \omega \,\mathrm{d}y$. Because the velocity is perpendicular to the vorticity gradient, the advection equation is trivially satisfied, and the layer is an equilibrium solution of the inviscid Euler equations. Whereas a circular vortex rotates without changing its shape, a uniform vortex layer shears itself without distortion. The former is a model for a localized eddy, while the latter represents a tangential velocity discontinuity of non-zero thickness.

Assume now that somewhere along the layer the circulation is locally stronger. That may happen because the vorticity is locally more intense, or because the layer is locally thicker. One can think of that configuration as a uniform layer on which a weak vortex blob is superimposed, such as on the left of figure 2.2. The velocity induced by the layer component is a simple shear; the fluid moves parallel to the

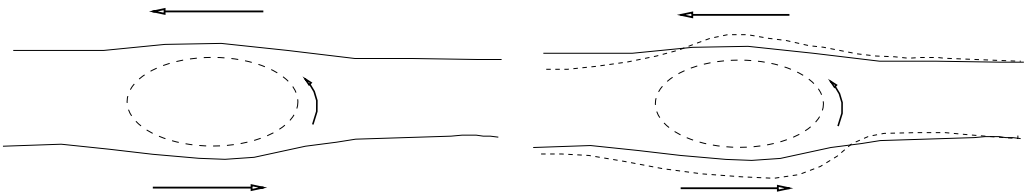

Figure 2.2: Sketch of the break-up of a slightly non-uniform vortex sheet into isolated vortex cores.

layer, and is slower above it than below. In the proper frame of reference the upper stream moves to the left, and the lower one to the right. The vortex that represents the local inhomogeneity induces an extra velocity which is approximately circular, and distorts the layer perpendicularly to the shear (see the two deformed dashed lines in the right-hand part of figure 2.2). To the right of the vortex, the layer moves into the the upper stream and is advected towards the left, and the opposite is true on the left side. The net effect is that extra vorticity is advected towards the inhomogeneity, which is in this way reinforced. The effect feeds on itself and ends up bleeding most of the vorticity from the neighbourhood of the initially stronger region, which becomes isolated, and circularizes. The original layer breaks in this way into approximately circular cores. This is the root of the Kelvin-Helmholtz instability of a uniform vortex sheet, which we will encounter later in connection with turbulent free shear flows.

The circular vortex and the vortex layer are therefore very different structures. Both are exact equilibrium solutions of the inviscid equations but, while the former is stable to most perturbations, the second one is not. The time that it takes for the instability to develop depends on the initial conditions, but it is of the order of L/Γ, where L is the length of the initial inhomogeneity. This is because the distortion of the layer by the instability requires that vorticity be transported over distances $O(L)$ by velocity differences which are $O(\Gamma)$. Shorter perturbations therefore develop faster, and the fastest ones are those whose lengths are of the order of the thickness h of the layer (the distinction between the uniform layer and the vortex blob cannot be made for shorter perturbations). The time for the breakup of a vortex layer is therefore $O(h/\Gamma) = O(1/\Omega)$, which is the basic 'eddy turnover' time scale for an inviscid vortical flow.

We have only considered up to now isolated structures. In practice vortex cores and sheets interact with one another, and the vorticities of different structures can have opposite signs. In some cases the point vortex approximation gives a qualitative idea of the behaviour of such arrangements. It is easy to see, for example, that two compact vortices of the same sign rotate around each other, while two vortices of opposite signs translate as a unit.

Problem 2.3: Consider two identical inviscid point vortices of circulation γ initially located a distance $2R$ from each other. Write the equation of motion for each vortex, and show that they rotate around their common centroid, while maintaining their initial distance. Repeat the

exercise with two vortices of opposite circulation.

Solution: Denote the complex position of the two vortices as z_1 and z_2. The velocity induced on z_2 by the vortex at z_1 is, from (2.10),

$$w(z_2) = u - \mathrm{i}v = \frac{\gamma}{2\pi\mathrm{i}(z_2 - z_1)}. \tag{2.19}$$

Since inviscid vorticity is simply advected by the flow, (2.19) is also the velocity with which the vortex moves,

$$\frac{\mathrm{d}z_2^*}{\mathrm{d}t} = \frac{\gamma}{2\pi\mathrm{i}(z_2 - z_1)}. \tag{2.20}$$

The * denotes complex conjugation, and is needed because of the form of the complex velocity. For similar reasons

$$\frac{\mathrm{d}z_1^*}{\mathrm{d}t} = \frac{\gamma}{2\pi\mathrm{i}(z_1 - z_2)}. \tag{2.21}$$

Adding and subtracting these two equations from each other, we obtain

$$\frac{\mathrm{d}}{\mathrm{d}t}(z_1 + z_2) = 0, \quad \Rightarrow \quad z_1^* + z_2^* = \text{constant} = 0, \tag{2.22}$$

and

$$\frac{\mathrm{d}}{\mathrm{d}t}(z_1^* - z_2^*) = \frac{\gamma}{\pi\mathrm{i}(z_1 - z_2)}, \quad \Rightarrow \quad |z_1 - z_2| = \text{constant} = 2R. \tag{2.23}$$

The first result shows that the centroid of the two vortices is stationary, while the second proves that their distance does not change. Writing then $z_1 = R\exp(\mathrm{i}\theta)$, and $z_2 = -z_1$, any of the two above equations of motion gives

$$\frac{\mathrm{d}\theta}{\mathrm{d}t} = \frac{\gamma}{4\pi R^2}, \tag{2.24}$$

which is a uniform angular velocity.

A similar derivation with $\gamma_1 = -\gamma 2 = \gamma$, and $z_1 = -z_2 = R$, shows that the two vortices of a counter-rotating vortex pair move parallel to each other with a uniform velocity,

$$\frac{\mathrm{d}z_1}{\mathrm{d}t} = \frac{\mathrm{d}z_2}{\mathrm{d}t} = -\frac{\mathrm{i}\gamma}{4\pi R}. \tag{2.25}$$

Once the vortices come close to each another, however, the analysis has to include a more complete description of the mutually induced velocity. Consider a vortex subject to the influence of its neighbours. If the vorticities don't overlap, the effect of the neighbouring vortices is described by an irrotational imposed flow, which can be expanded in a Taylor series near the vortex under consideration. The lowest order term in the series is a uniform velocity which simply advects the vortex as a unit. The next term is linear in the coordinates, and takes the form of a simple strain $\boldsymbol{u} = S\boldsymbol{x}$, where the matrix S is symmetric and trace-free (can you see why?). There are therefore axes in which the matrix is diagonal

$$S = \begin{pmatrix} \sigma & 0 \\ 0 & -\sigma \end{pmatrix}, \tag{2.26}$$

where the eigenvalue σ is real and positive. The streamlines of such a combination of a pure strain and a compact vortex are sketched in figure 2.3. The sketch on the left shows the situation when the strain is weak with respect to the vorticity $S^* = \sigma/\Omega \ll 1$. The flow far from the vortex looks like a pure strain, but near the vortex the streamlines are closed and almost circular. The two regions are separated by a streamline that passes through two stagnation points. The vortex is contained

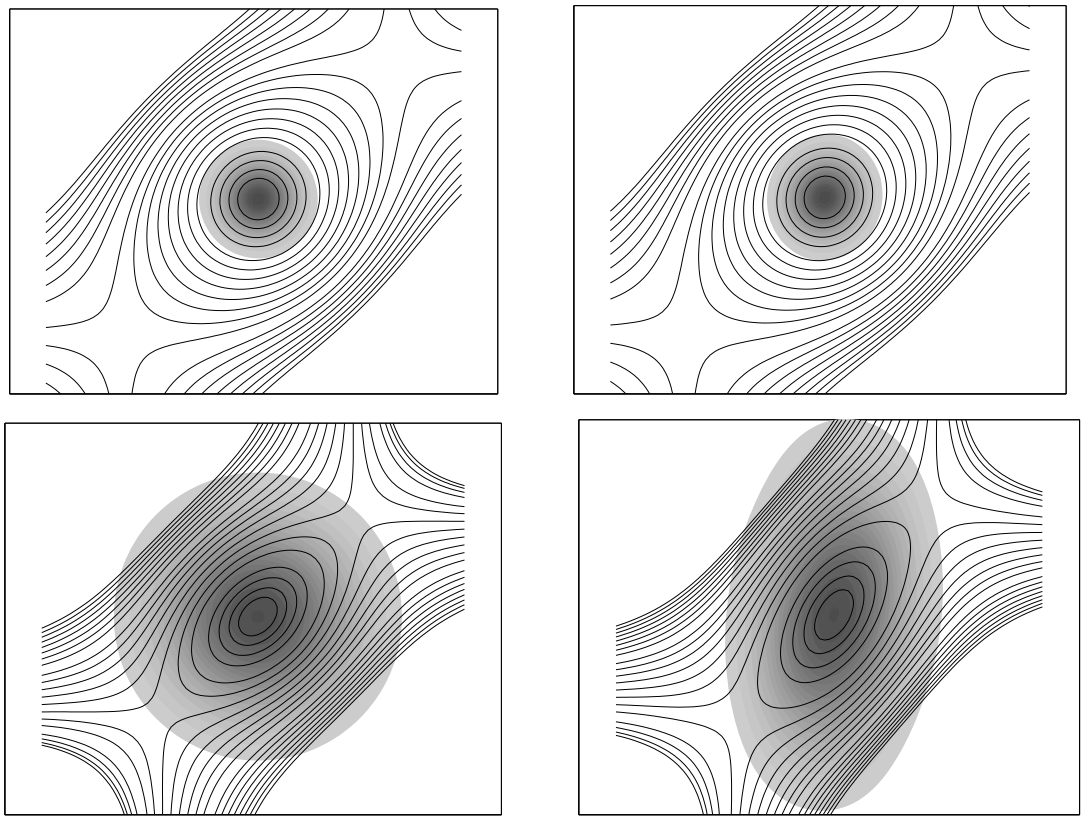

Figure 2.3: Sketch of the streamlines (solid lines) and vorticity (shaded area) of two vortices in an irrotational straining field. The strong, compact, gaussian vortex on the top row of figures shelters itself within its self-induced closed streamlines (left), and remains intact for long times (right). The weaker one on the bottom is not able to protect all of its vorticity (left), and is teared by the strain along the outgoing streamlines (right). For the top vortex $S^* = S/\omega_{max} = 0.016$. For the bottom one $S^* = 0.16$.

inside the central region, and its vorticity cannot cross the dividing streamline. In essence the vortex shelters itself from the strain by its own rotation. Such weakly strained vortices are stable, although their shape is elliptical rather than circular.

If the strain is stronger, the separating streamline moves inside the vortex, the vorticity escapes along the outgoing branches of the stagnation points, and the vortex is teared by the strain. In the particular case of a patch of uniform vorticity, for example, the limiting value of the strain is $S^* = 0.15$ (Saffman, 1992; pp. 168-171).

The combination of vortex interaction and mutual straining changes qualitatively the long term behaviour of vortex systems. An example that has some importance in real flows is vortex merging. We saw above that two compact vortices of the same sign rotate around each other. If their separation is comparable to their radii, they also strain each other. Below a critical distance, their vorticity bleeds

into a common structure, and the vortices merge. In systems with many vortices these interactions are inevitable, and result in an inverse cascade of vortex size in which the prevailing structures grow by amalgamation until they fill the boundary conditions or are stopped by some other physical mechanism. This is for example why in the atmosphere, which is essentially two-dimensional at large scales, storms and anticyclones grow until their characteristic sizes are of the order of the radius of the Earth, 10^3 Km.

If $S^* \gg 1$ the vorticity is essentially passive, and the vortex is deformed into long, thin, vortex layers along the outgoing branches of the imposed stagnation flow. The balance between vorticity and strain can be understood in terms of two competing time scales. The vortex rotates with a characteristic time scale $O(\Omega^{-1})$, and the strain deforms it on characteristic times $O(\sigma^{-1})$. The strain parameter S^* is the ratio of the two time scales, and the faster one wins.

An important result in two-dimensional vortical flows, and one that distinguished them from the three-dimensional ones, is that vorticity in two dimensions cannot be amplified. Viscosity can only smooth the initial vorticity extrema, at least when they occur away from the walls, and, although the vorticity of a given particle may increase as stronger vortices diffuse into weaker ones, the overall maximum of the vorticity magnitude can only decrease. Although general vortical flows can be very complex, this lack of a vorticity amplification mechanism means that the behaviour of two-dimensional vorticity configurations is relatively simple, and can often be understood in terms of a superposition of building blocks such as the ones studied in this section.

Problem 2.4: Assume a vorticity distribution decaying fast enough at infinity for all the necessary integrals to converge. Use incompressibility and the evolution equation (2.5) to show that

$$\Omega_m = \iint \omega^m \,\mathrm{d}x\,\mathrm{d}y, \tag{2.27}$$

decreases with time for all even orders m. Note that, in the limit of very large m,

$$\Omega_m \sim \max |\omega|^m, \tag{2.28}$$

where the maximum is taken over the whole integration domain, and use this result to conclude that the maximum of $|\omega|$ can only decrease. How would the presence of a wall change that conclusion?

Solution: Premultiplying (2.5) by $m\omega^{m-1}$, and using the incompressible continuity equation, $\nabla \cdot \boldsymbol{u} = 0$, we obtain

$$\frac{\partial \omega^m}{\partial t} + \nabla \cdot (\boldsymbol{u}\omega^m - \nu \nabla \omega^m) = -\frac{4\nu(m-1)}{m} |\nabla \omega^{m/2-1}|^2, \tag{2.29}$$

where the right-hand-side has been integrated by parts once. Integrating (2.29) over some domain in the plane, the divergence in the left-hand-side of the equation becomes a line integral,

$$\frac{\partial}{\partial t} \iint \omega^m \,\mathrm{d}x\,\mathrm{d}y + \oint \boldsymbol{n} \cdot (\boldsymbol{u}\omega^m - \nu \nabla \omega^m)\,\mathrm{d}\ell = -\frac{4\nu(m-1)}{m} \iint |\nabla \omega^{m/2-1}|^2 \,\mathrm{d}x\,\mathrm{d}y, \tag{2.30}$$

where $\boldsymbol{n}$ is the outer unit normal vector to the boundary ℓ of the integration domain. If the vorticity decays fast enough at infinity, the domain can be chosen so that it contains essentially all the vorticity. The line integral then vanishes, and we obtain

$$\frac{\partial \Omega_m}{\partial t} = -\frac{4\nu(m-1)}{m} \iint |\nabla \omega^{m/2-1}|^2 \,\mathrm{d}x\,\mathrm{d}y \le 0, \tag{2.31}$$

where the right-hand-side is negative because it is the integral of a square. This shows that (2.27) cannot increase with time.

When $m = 2$, this equation gives the evolution of the *enstrophy*, which is the mean-square value of the vorticity. The enstrophy equation (2.31) plays for vortical flows the same role as the energy dissipation equation (1.4) does for general ones.

For higher values of m the integrand of (2.27) becomes more and more concentrated near the extrema of ω, and (2.28) can be easily proved, showing that the maximum of $|\omega|$ cannot increase either. We will see in the next chapter that the same is not true for three-dimensional flows.

The previous argument relies on the vanishing of the contour integral in (2.30), which requires that an integration contour can be drawn such that both the vorticity and its gradient are zero. In the presence of a wall this is generally not possible. Although on a no-slip wall the velocity $\boldsymbol{u}$ is zero, and the first term in the contour integral vanishes, the vorticity gradient does not, and there is a *viscous flux* of vorticity into the domain. In the presence of walls, the previous proof does not apply, and both the maximum vorticity magnitude and the enstrophy can increase.

Note that, in the inviscid limit, there are no forces in equation (2.5). The only inviscid force in the Navier–Stokes equations, which is the pressure gradient, drops out of the vorticity equation (2.5) because the curl of a gradient vanishes identically. This is what makes vorticity specially significant in inviscid flows. Although the relation is not entirely straightforward, vorticity represents the density of angular momentum, and pressure, being a gradient, does not change it because it does not generate a torque.

2.3 The effect of viscosity

We can get a feeling for the effect of viscosity by looking at how it affects the inviscid structures studied in the previous section. Consider first a circular vortex. The kinematic equations are not modified by viscosity and the velocity field is axisymmetric. The advection terms in the dynamic equation are identically satisfied, and the only evolution is viscous,

$$\frac{\partial \omega}{\partial t} = \frac{\nu}{r} \frac{\partial}{\partial r} \left(r \frac{\partial \omega}{\partial r} \right). \tag{2.32}$$

Consider for example an initial vorticity distribution $\omega = \Omega(r/R)$, where R is an initial characteristic radius. Equation (2.32) can be rewritten in parameter-free form by defining a rescaled time $\hat{t} = \nu t/R^2$, and a rescaled length $\hat{r} = r/R$. The rescaled viscosity is then unity, and so is the initial size of the vortex, which therefore evolves in $\hat{t} = O(1)$. This fixes the viscous evolution time scale of any vortical flow of size R, which is $T_v = R^2/\nu$. This scale is short or long with respect to the inviscid 'turnover' time identified in the previous section, depending on whether the ratio $\Omega T_v = \Omega R^2/\nu \sim \gamma/\nu$ is small or large. This ratio is the Reynolds number of the vortex. As usual, low Reynolds number vortices decay viscously before they have time to deform themselves, while high Reynolds number ones evolve as if they were essentially inviscid.

The effect of viscosity is to spread and to weaken the vortices, while their total circulation is conserved. It is easy to see by integrating (2.5) that, in the absence of walls, the total circulation is independent of time even in the presence of viscosity.

Note that this implies that the Reynolds number γ/ν of a decaying circular vortex stays constant, and that vorticity blobs do not become 'more' or 'less viscous' as they dissipate. It is also easy to show that the 'radius of inertia' of the vortex increases as the square root of time, while the characteristic vorticity falls as t^{-1}.

Problem 2.5: Consider the axisymmetric vorticity evolution equation (2.32), and an isolated vortex whose vorticity decays fast enough at infinity for $r^4\omega(r) \to 0$. Show that its circulation

$$\gamma = 2\pi \int_0^\infty r\omega \, \mathrm{d}r, \tag{2.33}$$

is constant in time. Define a vortex 'radius' R_ω by

$$R_\omega^2 = 2\pi\gamma^{-1} \int_0^\infty r^3\omega \, \mathrm{d}r, \tag{2.34}$$

and show that it grows linearly with time

$$R_\omega^2 = R_\omega^2(0) + 4\nu t. \tag{2.35}$$

From those results conclude that the characteristic magnitude of the vorticity decays as t^{-1} for long times. As a particular example show that an initially Gaussian vortex

$$\omega = \frac{\gamma}{\pi R_\omega^2} \, \mathrm{e}^{-r^2/R_\omega^2}, \tag{2.36}$$

retains its form as it decays.

Solution: The problem itself is trivial. To obtain (2.33) and (2.35), premultiply (2.32) by the appropriate power of r, and integrate from $r = 0$ to $r = \infty$. Integrate the right-hand side by parts until it has be written as much as possible as a boundary term. Boundary terms cancel at the centre because $r = 0$, and at infinity because the vorticity vanishes. The result is

$$\frac{\partial \gamma}{\partial t} = 0, \tag{2.37}$$

and

$$\frac{\partial R_\omega^2}{\partial t} = 4\nu, \tag{2.38}$$

which establish the desired properties. The decay law for the characteristic vorticity follows from the order-of-magnitude argument that the circulation equals the vorticity times the vortex area. Since (2.35) shows that the latter increases linearly with time for large times, while (2.37) implies that the former stays constant, the vorticity has to behave as t^{-1}.

It is always important, when using this kind of arguments, to specify what a 'large' time means. In this case follows from (2.35) that, for the growth of the area to be linear, it has to be true that

$$4\nu t \gg R_\omega^2(0), \quad \Rightarrow \quad t \gg R_\omega^2(0)/4\nu. \tag{2.39}$$

Note that this is the same 'viscous' time already obtained at the beginning of this section from scaling arguments.

Comment: The interest of this problem resides in that the conservation laws derived in it for axisymmetric distributions also apply to more general cases. Consider for example the circulation of any vorticity distribution, not necessarily axisymmetric, decaying reasonably fast at infinity. Using continuity, we can write the vorticity evolution equation (2.5) as

$$\frac{\partial \omega}{\partial t} = \nabla \cdot (\nu \nabla\omega - \boldsymbol{u}\,\omega) \tag{2.40}$$

The right-hand side of this equation is a divergence, and becomes a contour integral when we integrate the equation over a large domain, as we did in problem 2.4,

$$\frac{\partial}{\partial t} \iint \omega \, \mathrm{d}x \, \mathrm{d}y = \oint \boldsymbol{n} \cdot (\nu\nabla\omega - \boldsymbol{u}\,\omega) \, \mathrm{d}\ell. \tag{2.41}$$

If the vorticity has decayed enough on the domain boundary, both its magnitude at its gradient are negligible in the right-hand side of this equation, and the total circulation in the left-hand side is conserved. If no contour satisfying that property can be found, such as in the presence of a wall, the first term inside the right-hand integral can be interpreted as the viscous vorticity flux into the domain, and the second one as the advective transport of vorticity through the boundary. Under those circumstances, the total circulation is not conserved.

The viscous spreading law (2.38) also applies to general vorticity distributions away from walls. The vortex radius is then defined as

$$\gamma R_\omega^2 = \iint |\boldsymbol{x} - \boldsymbol{x}_\gamma|^2 \omega \, \mathrm{d}x \, \mathrm{d}y, \tag{2.42}$$

where $\boldsymbol{x}_\gamma$ is the centroid defined in (2.14). Equation (2.38) is a statement on the evolution of angular momentum. For details on its derivation, and for a discussion of other conservation properties of two-dimensional vortex flows, see the book by Saffman (1992; §3).

The Gaussian vorticity distribution defined by (2.35) and (2.36) represents a self-similar axisymmetric viscous vortex which preserves its shape as it decays. It can be shown that a generic axisymmetric vorticity distribution, as long as it has non-zero circulation, eventually decays to that configuration (see the comment at the end of problem 2.9). Since we have seen that isolated vortices tend to circularize, a collection of spreading, approximately Gaussian, vortices is a common long-term limit for many vorticity distributions.

There are equivalent results for isolated vorticity layers [PROBLEM 2.9]. The main difference is that the characteristic vorticity decays in that case only as $t^{-1/2}$, so that the Reynolds number of a decaying sheet *increases* with time. Isolated sheets therefore eventually become inviscid, and break into individual cores through the Kelvin–Helmholtz instability mechanism.

In the case in which the flow brings together vorticities of opposite signs the damping effect of viscosity can be much faster than in the case of isolated structures. Consider for example the initial distribution

$$\omega = \omega_0 \sin(ky), \tag{2.43}$$

which models an array of vortex layers of alternating signs. The corresponding velocity is

$$u_x = \frac{\omega_0}{k} \cos(ky), \qquad u_y = 0. \tag{2.44}$$

The nonlinear term drops out of the evolution equation, which becomes

$$\frac{\partial \omega}{\partial t} = \nu \frac{\partial^2 \omega}{\partial y^2}, \tag{2.45}$$

and the vorticity decays exponentially, instead of algebraically as it did in the two previous cases

$$\omega = \omega_0 \mathrm{e}^{-k^2 t} \sin(ky). \tag{2.46}$$

This viscous vorticity cancellation is the key mechanism for the decay of two-dimensional vorticity distributions. While the energy moves to larger scales by amalgamation, the vortex debris that we saw being generated during circularization and merging is strained into thin layers, and cancels with other structures of the opposite sign by viscous diffusion.

2.4 Point vortex systems

We have seen that a system of small Gaussian vortices is a reasonable long-term limit for two-dimensional vortical flows. If the Reynolds number is large enough, viscosity spreads the vortices only slowly, and its effects can be neglected in the short term. If the resulting blobs are far apart from each other, they still interact as points, and such systems are often simpler to analyze than more general vorticity distributions, and can be used to gain insight on them. We have for exmaple used that simplification in problem 2.3 to study the behaviour of vortex pairs.

We saw in comment 2.1 that point vortices can be described compactly in terms of complex variables. If we consider a collection of inviscid vortices with circulations γ_j, located at $z_j = x_j + \mathrm{i}y_j$, the complex velocity induced by them on a point z' is

$$w(z') = \frac{1}{2\pi\mathrm{i}} \sum_j \frac{\gamma_j}{z' - z_j}. \tag{2.47}$$

A fluid particle at position z' would then move with that velocity and, since we have seen that the vorticity is advected by the fluid velocity, the equation of motion of the vortex at z_j is

$$\frac{\mathrm{d}z_j^*}{\mathrm{d}t} = \frac{1}{2\pi\mathrm{i}} \sum_{k\neq j} \frac{\gamma_k}{z_j - z_k}, \tag{2.48}$$

where the asterisk stands for complex conjugation. Note that in the sum of the right-hand side of this equation, the effect of the vortex on itself has not been included. As we noted above, the only effect of the self-induction is to make the point 'rotate' on itself, and it has no effect on the vortex position.

The equations (2.48) are conservative, since they are inviscid, and conserve the linear and angular momenta of the flow velocity field, as well as its kinetic energy. The calculation of these quantities needs in general some care because the integrals have to be extended to the whole plane, and some of them diverge formally, but they can be regularized by considering the *changes* in the invariants as the vortices move around, instead the invariants themselves. In point vortex systems, on the other hand, the invariants are easily checked by substituting them into the equations of motion. The result is that the conservation of linear and angular momenta corresponds to the invariance of the centroid and of the moment of inertia of the vortex system, where each vortex is treated as a point of mass γ_j. The energy becomes an expression that looks roughly like the mutual potential energy of a set of point charges.

Problem 2.6: For a system of point vortices satisfying equations (2.48) show directly that the following quantities are constant,

$$\textbf{Linear momentum:} \qquad M = \sum_j \gamma_j z_j, \tag{2.49}$$

$$\textbf{Angular momentum:} \qquad I = \sum_j \gamma_j |z_j|^2, \tag{2.50}$$

$$\textbf{Energy:} \qquad E = -\sum_j \sum_{k\neq j} \gamma_j \gamma_k \log|z_j - z_k|. \tag{2.51}$$

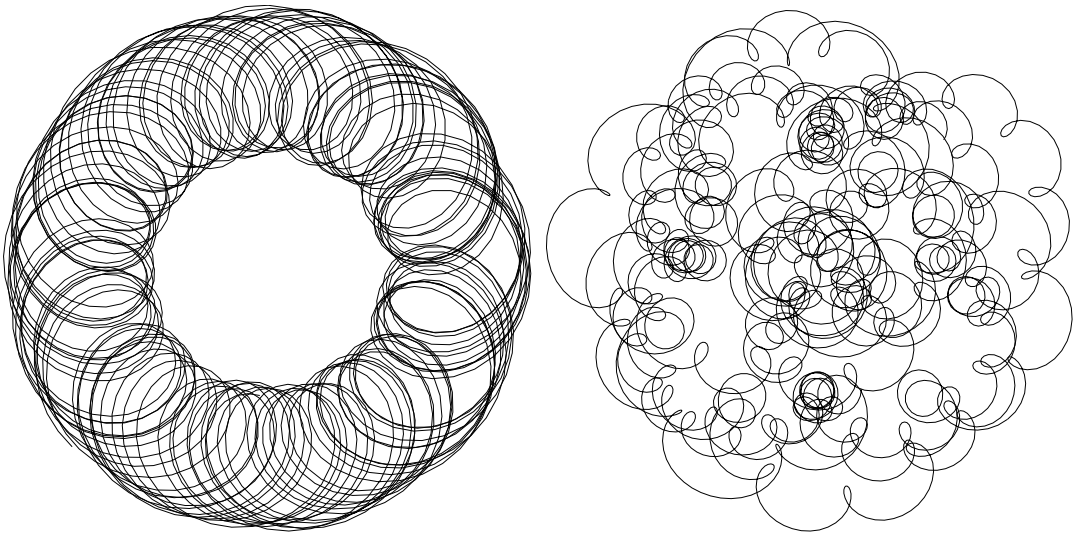

Figure 2.4: Trajectories of a vortex in a system of identical vortices initialized from random initial positions. Left: From a non-chaotic system of three vortices. Right: From a chaotic system of six vortices.

Give dimensional justifications for the names given above to the different invariants, note that, because the linear momentum is a complex quantity, these three equations define four different invariants.(*Hint*: You may find it easier to do first the case of two vortices, and later generalize the procedure).

The basic properties of two-dimensional vortices are described in the book by Batchelor (1967; pp. 527–532), and the behaviour of point vortex systems are reviewed in more detail by Aref (1983). The invariants cited above strongly constrain the motion of the vortices. Conservation of angular momentum, for example, ensures that the system stays confined in a radius comparable to its original size, while energy conservation prevents vortices of the same sign from coming too close to each other, so that the *mean* separation between vortices stays roughly constant.

Comment 2.7: An important exception to the restrictions imposed by the invariants on the separation among the vortices, is the behaviour of tight pairs of vortices of opposite signs, which carry essentially zero momentum and energy. Such *dipoles* form spontaneously, and essentially decouple from the rest of the system, becoming for example able to escape to infinity or to come very close to other vortices without expending too much energy or angular momentum. They are like neutral atoms forming in a highly ionized plasma, which can free themselves from the electromagnetic interactions which affect charged particles.

Consider for example an isolated point vortex of circulation γ, whose complex position is z, trying to move apart from a collection of vortices $(\gamma_j,\, z_j)$. The energy due to its interaction with the vortex system is given by (2.51) as

$$E_0 = -\gamma \sum_j \gamma_j \log|z - z_j|. \tag{2.52}$$

If $|z| \gg |z_j|$, we can expand it to lowest order as

$$E_0 \approx -\gamma \log|z| \sum_j \gamma_j. \tag{2.53}$$

Since the system conserves the total energy, this logarithmically decreasing negative energy can only come from 'cooling' the rest of the vortices, and the stray vortex is unable to move farther away when all the energy in the system has been used.

Consider on the other hand the same situation for a counter-rotating vortex pair $\pm\gamma$ at $z \pm h$. Assume that $|h| \ll |z|$. The interaction energy is now

$$E_0 = -\gamma \sum_j \gamma_j \log \frac{|z + h - z_j|}{|z - h - z_j|} \approx -2\gamma \sum_j \gamma_j \mathrm{Re}(z_j/z). \tag{2.54}$$

In contrast with the case of the isolated vortex, the interaction energy now decreases as the pair moves away, and there is no impediment to it flying to infinity. The intuitive reason for that is that the velocities induced by the members of the pair tend to cancel each other, so that they are not seen once the pair is far away from the rest of the vortices.

2.4.1 *The emergence of chaos*

We are now ready to return to the question of chaos in deterministic systems, and in particular to whether the behaviour of systems of point vortices can become complex. The governing equations (2.48) are easily programmed in a computer and allow us to study their behaviour in arbitrary cases, even if analytic solutions are not easily found. In figure 2.4 we show the trajectory of one particular vortex in two different point vortex systems. The one in the left of the figure belongs to a system of three identical vortices, while the one in the right belongs to one with six. They are clearly different. While the trajectory in the left looks ordered, and it is conceivable that we could find an analytic description for it, the one on the left looks chaotic.

The qualitative difference between both systems can be understood in terms of their respective number of degrees of freedom. A system of N vortices can be described with $2N$ numbers, which correspond to their coordinates, but not all of them are independent. The invariants (2.49)–(2.51) represent four constraints (two linear momentum components, one angular momentum, and the energy), and the number of independent coordinates is only $2N - 4$. The three-vortex systems therefore lives in a two-dimensional surface, while the six-vortex one moves in an eight-dimensional space.

Systems with two independent degrees of freedom are constrained to be simple. Equations (2.48) are an example of a dynamical system,

$$\frac{\mathrm{d}\boldsymbol{z}}{\mathrm{d}t} = F(\boldsymbol{z}), \tag{2.55}$$

whose evolution is fully determined by the state $\boldsymbol{z}$ in 'phase' space. We can trace the trajectory $\boldsymbol{z}(t)$ of the system for each initial condition, and the evolution of the system is completely described by the set of all such 'orbits'. Because the tangent to a given orbit is determined at each point by (2.55), it is unique. Orbits cannot cross each other except at the small number of critical points for which $F(\boldsymbol{z}) = 0$, where the tangent is not defined. It is easy to see that this is a strong topological constraint on the behaviour of a system moving on a two-dimensional phase space. Any orbit in such a system divides the phase space into two halves. Any other trajectory has to remain in one of those halves without crossing into the other.

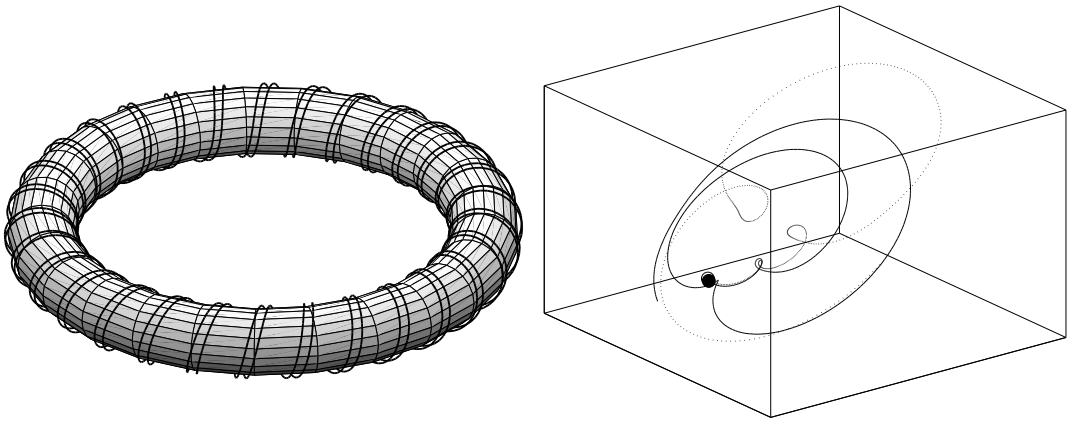

Figure 2.5: Left: Two trajectories on a two-dimensional manifold, such as the surface of this torus, cannot diverged too much from one another without intersection. Their behaviour is then limited to be relatively simple. Right: Two trajectories starting close to each other at the points marked with circles. Since there are no restrictions on lines crossing each other when the dimension of the embedding space is at least three, trajectories with three or more degrees of freedom can intertwine and diverge exponentially, allowing chaotic behaviour. The two cases in these figures correspond qualitatively to those in figure 2.4.

Two such trajectories define a 'corridor', and any trajectory in this corridor stays within it forever. Even a cursory attempt to draw a set of non-intersecting infinitely long, or closed, lines in a paper convinces oneself that their behaviour cannot be too complicated. In particular two trajectories which are initially close to each other cannot separate too much without intersection some other neighbouring trajectory. Note that a two-dimensional phase space is not necessarily a plane, and that any projection of the trajectories may appear to intersect each other, but that there is always a representation in which the trajectories are simple and non-intersecting (see the left parts of figures 2.4 and 2.5, and PROBLEM 2.10).

When the number of independent degrees of freedom is three or more, this topological constraint on the trajectories disappears, and they can intertwine in arbitrary ways (see the right part of figure 2.5). This is the situation for the six-vortex system. One of the surprising discoveries of the last fifty years has been that deterministic systems with relatively few degrees of freedom can behave in very complex ways, and that as soon as the topological restriction of two-dimensional systems is removed, the generic behaviour of an arbitrary system is to be chaotic. A semi-popular but rigorous account of the genesis of chaos is given by Lorentz (1993).

The key property of chaotic systems is their sensitivity to initial conditions. Two trajectories with initial conditions which differ only by a small amount diverge exponentially, and soon become completely decorrelated. It is as if the trajectories, free from the need of remaining close to each other, chose to diverge in arbitrary ways. This behaviour can be proved rigorously, and its plausibility can be seen by

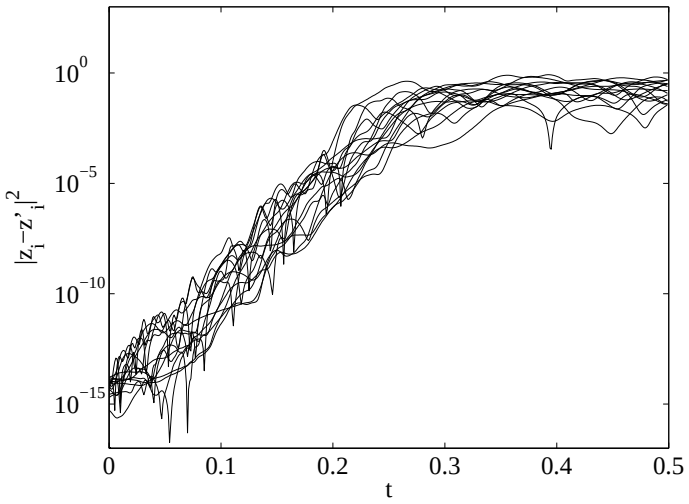

Figure 2.6: Evolution of the distance by which the corresponding vortices in two systems of fifteen vortices, whose initial conditions differ by random small amounts, diverge from one another. Each line corresponds to a different vortex pair. The initial exponential divergence is typical of chaotic systems, while the later saturation happens when the separations are large enough that the two systems can be considered uncorrelated from one another.

the following argument. Write a linearized equation for the difference between two neighbouring trajectories of (2.55), $\boldsymbol{z}(t)$ and $\boldsymbol{z}(t) + \boldsymbol{\delta}(t)$. Neglecting higher-order terms, the evolution of $\boldsymbol{\delta}$ is given by

$$\frac{\mathrm{d}\delta_j}{\mathrm{d}t} = F_{jk}\delta_k, \tag{2.56}$$

where the Jacobian, $F_{jk} = \partial F_j/\partial z_k$, is evaluated at the trajectory $\boldsymbol{z} = \boldsymbol{z}(t)$, and is independent of $\boldsymbol{\delta}$. This is a linear set of equations which in general has exponential solutions with exponents that correspond to the eigenvalues of F_{jk}. If any of them has a positive real part, the magnitude of $\boldsymbol{\delta}$ increases exponentially with time. The proof of why this happens in conservative systems is beyond the scope of this notes, but the essence is the following. In the previous construction, the real parts of the different eigenvalues represent how the separations in different directions grow or shrink as the two neighbouring systems evolve. The sum of all the real parts measures the rate of growth of the volume of phase space defined by the N separation eigenvectors. But the evolution of conservative systems conserves volume in phase space, so that the sum of the real parts of the eigenvalues has to vanish, and if one of them happens to be contracting (negative), some other has to be expansive (positive). This is the reason why conservative systems, if they have enough degrees of freedom, tend to become chaotic and to amplify any exponentially small differences in the initial conditions (figure 2.6).

The consequence of this divergence is that the influence of the initial conditions is lost very quickly, and that all the systems with the same values of whichever

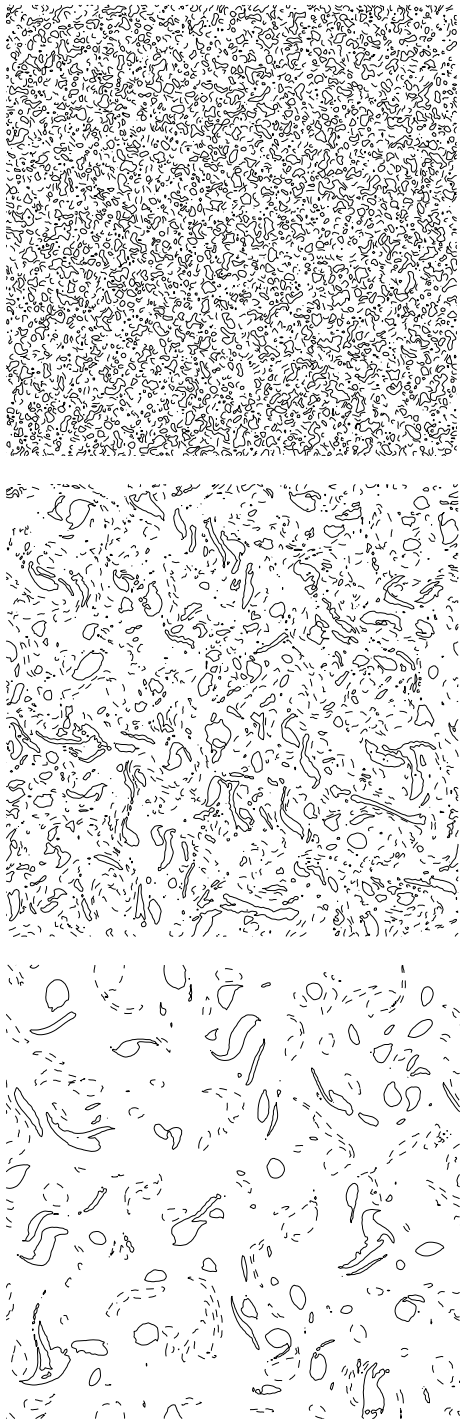

Figure 2.7: Decay of a two-dimensional random vorticity distribution in a doubly-periodic box. The Reynolds number, based on the box side, is $\langle u^2\rangle^{1/2}L/\nu = 1.2\times10^4$, and the time between the first (top) and last (bottom) snapshots is $\langle u^2\rangle^{1/2}t/L = 0.5$, or $\langle \omega^2\rangle^{1/2}t = 45$ based on the initial vorticity field. Solid contours are positive vorticity; dashed ones are negative.

invariants are conserved, are equivalent. Statistics then become relevant. Observing many experiments with different slightly initial conditions becomes equivalent to studying a single experiment for a long time. It is also of little interest to follow individual vortices, since relabeling vortices with different names is a particular case of different initial conditions, and those are all equivalent to one other. Because they are conservative, point vortex systems become chaotic as soon as their number of degrees of freedom, and the topology of their phase space, allows them to. Systems of real vortices are more complicated, because the close interactions that we have mentioned above makes them not exactly conservative, but vortices interact only occasionally. The reason why real two-dimensional turbulence becomes quickly chaotic is the same as for the simplified systems studied here. We have in fact seen that random initial vorticity distributions tend to organize themselves into systems of compact vortex cores. The decay of the resulting flow is well described, to a first approximation, by the chaotic evolution of those cores, although modified by the processes of amalgamation, filamentation into sheets and viscous cancellation described above (figure 2.7)

SUPPLEMENTARY PROBLEMS

Problem 2.8: A simple one-dimensional model for the nonlinear acoustic effects responsible for the formation of shock waves is Burgers' equation

$$\frac{\partial \rho}{\partial t} + \rho \frac{\partial \rho}{\partial x} = \nu \frac{\partial^2 \rho}{\partial x^2}. \qquad (P2.1)$$

If we define the 'mass' in the interval $x \in (a,\, b)$ as the integral

$$M = \int_a^b \rho \, \mathrm{d}x,$$

and the 'energy' as

$$E = \int_a^b \rho^2 \, \mathrm{d}x,$$

show that, except for boundary terms which can be interpreted as boundary fluxes, (P2.1) conserves mass but not energy, and that the rate of change of the latter is proportional to the 'viscosity' ν.

Define a steady 'shock wave' as a smooth solution, steady in a frame of reference moving with an advection velocity U_s, and connecting two uniform states $\rho(-\infty) = U_a$ and $\rho(\infty) = U_b$. Working in that frame of reference reduce (P2.1) to an ordinary differential equation, compute the form of the shock wave, and show that $U_s = (U_a + U_b)/2$.

Show that the viscosity determines the thickness of the shock. Using the formula obtained above for the rate of change of the energy, compute the energy dissipated by the shock per unit time, and show that it approaches a non-zero limit as $\nu \to 0$. Note that the solution only makes sense if $\nu(U_a - U_b) > 0$, and that this implies that energy is dissipated by the shock if $\nu > 0$, and created otherwise. Can you think of physical situations, not necessarily in a viscous flow, in which energy is created within very thin regions?

Before concluding that mass conservation and the dissipation of energy within discontinuities are properties of the 'inviscid' equation

$$\frac{\partial \rho}{\partial t} + \rho \frac{\partial \rho}{\partial x} = 0,$$

repeat the same calculations for the equations

$$\rho\left(\frac{\partial\rho}{\partial t}+\rho\frac{\partial\rho}{\partial x}\right)=\nu\frac{\partial^2\rho}{\partial x^2}.$$

and

$$\frac{\partial\rho}{\partial t}+\rho\frac{\partial\rho}{\partial x}=\nu\frac{\partial^3\rho}{\partial x^3}.$$

both of which have the same inviscid limit as (P2.1). What do the results suggest about the relationship between the high-Reynolds number limit of the Navier-Stokes equations, $\nu\to 0$, and the Euler equations in which $\nu=0$? Would it make sense to study turbulence as a property of the Euler equations?

Problem 2.9: Repeat exercise 2.5 for a uniform vortex layer $\omega(y,\,t)$, whose evolution equation is (2.45).

$$\frac{\partial\omega}{\partial t}=\nu\,\frac{\partial^2\omega}{\partial y^2}.$$

Devise suitable definitions for the circulation per unit length, Γ, and for the layer 'thickness' δ_ω, and show that the former is constant while the square of the latter grows linearly with time. Show also that an initially Gaussian layer decays self-similarly.

Note that, in this case, the Reynolds number of the self-induced motion of the layer grows with time, so that any isolated vortex layer can, for long times, be expected to become unstable and break into more-or-less circular vortices. Estimate that this happens when the thickness reaches $\delta_\omega=O(\nu/\Gamma)$.

(The following part is hard:) It is relatively easy in this case to prove that the asymptotic state of arbitrary initial vorticity is a Gaussian sheet. Define the Fourier transform of the vorticity distribution,

$$\Omega(k,\,t)=(2\pi)^{-1}\int_{-\infty}^{\infty}\omega(y,\,t)\mathrm{e}^{-\mathrm{i}ky}\,\mathrm{d}y,$$

and show that its evolution equation is

$$\frac{\partial\Omega}{\partial t}=-\nu k^2\Omega.$$

Integrate it, and note that, for long times, only the wavenumbers $k\ll(\nu t)^{-1/2}$ remain, for which $\Omega(k,\,0)\approx\Omega(0,\,0)$. Make this approximation, and invert the Fourier transform

$$\omega(y,\,t)=\int_{-\infty}^{\infty}\Omega(k,\,t)\mathrm{e}^{\mathrm{i}ky}\,\mathrm{d}k.$$

Extend this argument to a higher order approximation by expanding $\Omega(k,\,0)$ as a Taylor series in k, and use the first few terms of this series to estimate how long it would take for a given vortex layer to become approximately Gaussian.

The same procedure can be used to prove that an axisymmetric vortex decays to Gaussian, but one must then use the axisymmetric version of the Fourier transform, called the Haenkel transform, in which exponentials are substituted by Bessel functions.

Problem 2.10: Consider three identical vortices whose complex positions are z_j, $j=1\ldots 3$. As seen in exercise 2.6, their evolution conserves

$$z_1+z_2+z_3=0,$$

$$|z_1|^2+|z_2|^2+|z_3|^2=I,$$

$$|z_1-z_2|^2|z_2-z_3|^2|z_3-z_1|^2=E.$$

Show that these conservation properties define a two-dimensional surface. In the case that $E/I^3 = \epsilon^2 \ll 1$, show that two of the three vortices have to remain close to each other. Name them z_1 and z_2 and show that the surface is given to lowest order in ϵ by

$$|z_3| = (2I/3)^{1/2} + O(\epsilon^2),$$

$$|z_1 - z_2| = \frac{2I^{1/2}\epsilon}{3} + O(\epsilon^2).$$

Interpret geometrically the motion of the system. Set up a simple numerical simulation and check the prediction of the two previous equations. In particular check that z_3 and $z_1 - z_2$ describe approximate circles of very different radii, and interpret those circles as sections of a long thin torus. Interpret the trajectory in the left of figure 2.4, which apparently intersects itself, as the projection over z_1 of a non-intersecting trajectory on the surface of such a torus, such as sketched in figure 2.5.

Chapter 3

Vorticity in three dimensions.

Summary

Each of the two previous chapters had to accomplish at least two things. In the first chapter, for example, we introduced turbulence and the concept of the energy cascade, but we also had to get acquainted with fractal objects and with non-analytic functions. In the second chapter we studied the behaviour of vorticity in two dimensions, but part of the discussion had to be devoted to the concept of chaos, and to how deterministic equations sometimes lead to apparently non-deterministic solutions.

The present chapter is simpler. In it we discuss the differences between the behaviour of vorticity in two and in three dimensions, and show that those differences are at the root of the energy dissipation mechanism of turbulent flows.

There are two crucial sections in this chapter. In §3.2, and in particular in §3.2.1, we describe how three-dimensional vorticity can be stretched, and how that leads to an overall growth of the enstrophy. Since we will also show, in comment 3.2, that the mean dissipation is proportional to the mean enstrophy, that will give us the clue as to how energy dissipation is implemented in turbulence.

The second important section is §3.3, where we study the effect of viscosity. While in two dimensions viscosity always leads to the spreading of vortex cores, in three dimensions it interacts with vortex stretching to determine the length scale at which the two effects balance. We will show that all the vorticity in a sufficiently complicated three-dimensional viscous flow will eventually evolve into objects with that particular length scale. We will then see that this scale is nothing but the Kolmogorov viscous length that we had already introduced in chapter 1 as the distance below which turbulent flows have to be smooth. At the end of that section we will find, in §3.4, that we are ready to justify the qualitative cascade model used in the introduction to explain the anomalous behaviour of the dissipation at vanishing viscosities.

The other three sections in this chapter are either auxiliary or more qualitative. Section 3.1 describes the kinematic differences between two- and three-dimensional vorticity, and introduces some elementary vortical objects that can be used to sim-

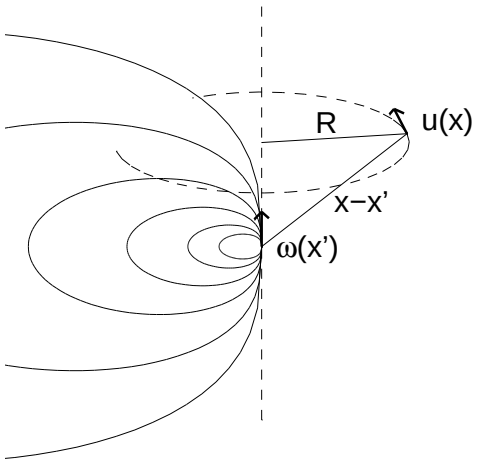

Figure 3.1: Velocity induced by a vortex 'element' $\boldsymbol{\omega}(\boldsymbol{x}')$. Because of the vector product in (3.1) the velocity is axisymmetric around the direction of the vorticity, and tangential to a circle centred at that axis. The velocity magnitude, which is proportional to $R/|\boldsymbol{x}-\boldsymbol{x}'|^3$, is plotted in the isolines to the left of the figure. It is highest near the vortex and decays roughly as $|\boldsymbol{x}-\boldsymbol{x}'|^{-2}$.

plify the discussion of the latter case. As such, that section is needed to understand the rest of the chapter. The last two sections are descriptive. The subjects described in them are important to understand the behaviour of real flows, but their full discussion is beyond the scope of the present lectures. You should at least read them, and try to visualize the interactions that they describe.

3.1 Kinematics

As in two-dimensional flows there are two important aspects to vorticity: we can either see it as a descriptor of the flow, or as a dynamical quantity with its own evolution equation. The first aspect is the easiest to understand. Given $\boldsymbol{\omega}$, we can compute the velocity of the flow by a three-dimensional analog of the Biot–Savart law (2.7),

$$\boldsymbol{u}(\boldsymbol{x}) = \frac{1}{4\pi}\int \frac{\boldsymbol{\omega}(\boldsymbol{x}')\wedge(\boldsymbol{x}-\boldsymbol{x}')}{|\boldsymbol{x}-\boldsymbol{x}'|^3}\,\mathrm{d}^3\boldsymbol{x}' + \nabla\phi = \boldsymbol{u}_\omega + \nabla\phi. \tag{3.1}$$

There is an irrotational component $\nabla\phi$ which appears not to be directly determined by the vorticity, but that is not exactly true. The velocity $\boldsymbol{u}_\omega$ given by the integral in the Biot–Savart formula is solenoidal, and continuity requires that

$$\nabla^2\phi = 0. \tag{3.2}$$

We have already mentioned that the solutions of Laplace's equation are generally smooth and uninteresting from the dynamical point of view, but it should not be concluded that the potential ϕ is completely irrelevant. Consider (3.1) in a domain

with solid boundaries. In an inviscid flow, the only requirement at the boundary is that the normal velocity should vanish, so that the boundary condition for ϕ is that

$$\frac{\partial \phi}{\partial \boldsymbol{n}} = -\boldsymbol{n} \cdot \boldsymbol{u}_\omega. \tag{3.3}$$

This uniquely determines the velocity potential [PROBLEM 3.5] and, since $\boldsymbol{u}_\omega$ changes with time as the vortices move around, the potential also evolves, and contributes to the flow dynamics. We will see in §3.6 that the effect of this potential component of the flow velocity is even more important in the viscous case.

As in two dimensions, the kernel in (3.1) can be understood as the velocity due to a 'point vortex', which is in this case an infinitesimal vector (figure 3.1). The situation is now however more complicated, because vorticity is solenoidal. The divergence of the curl of any vector is zero, and the vorticity flux through any closed surface must vanish. As with the streamlines of an incompressible fluid, the vortex lines, which are the streamlines of the vorticity field, cannot end within the flow, and either have to be infinite or closed. In the case of an inviscid flow, in which a slip velocity is allowed between the fluid and the wall, there is the third possibility that vortex lines end at the wall. This is however only an idealization since. In real viscous flows in which there is no slip in the boundaries between two media, the normal vorticity component has to vanish at the wall and vortex lines have to be be parallel to it.

Problem 3.1: Note that if the wall itself is rotating, the no-slip condition requires that the wall-normal component of the vorticity of the fluid has to match the wall-rotation. Vortex lines then leave or enter the body to accommodate this vorticity. Show that, if the wall belongs to a solid whose angular velocity in $\boldsymbol{\Omega}$, the wall-normal vorticity component at the wall is

$$\omega_n = 2\boldsymbol{\Omega} \cdot \boldsymbol{n}, \tag{3.4}$$

where $\boldsymbol{n}$ is the outer unit normal vector to the body.

A useful concept in describing the geometry of vortical flows is the vortex tube, which is a surface which is everywhere tangent to the vorticity vector, and which is thus formed by vortex lines. Since there is no vorticity flux through the surface of the tube, the vorticity flux across any of its cross-sections has to be the same, and Stokes' theorem,

$$\int_A \boldsymbol{\omega} \cdot \boldsymbol{n} \, \mathrm{d}^2\boldsymbol{x} = \oint_{\partial A} \boldsymbol{u} \cdot \, \mathrm{d}\boldsymbol{x}, \tag{3.5}$$

ensures that the circulation around any section of the tube is constant.

A thin vortex tube inside which the vorticity magnitude is much higher than in the surrounding fluid is the closest equivalent to the point vortices that we used in two dimensions, and can be visualized as a tight 'bundle' of vortex lines. The velocity induced by such a 'line' vortex can be found by integrating (3.1) for a vorticity distribution which is zero outside a thin cylinder surrounding the vortex axis. It follows from solenoidality that the vorticity vector inside the cylinder has to be approximately parallel to the axis, and that the circulation Γ is constant along the vortex, even when the cross-sectional area is not. If we apply (3.1) at a point $\boldsymbol{x}$

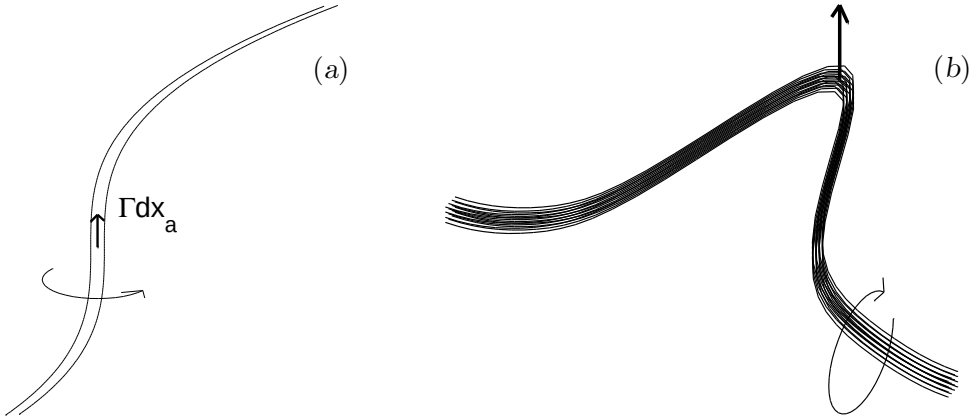

Figure 3.2: A compact vortex tube, like the one in (a), is approximately equivalent to a vortex line of constant circulation Γ aligned with the axis of the tube. In (b) the local induction of the curved vortex line tends to raise the head of the 'hairpin'.

which is far from the vortex, we can substitute to lowest order the vector $\boldsymbol{x} - \boldsymbol{x}'$ by $\boldsymbol{x} - \boldsymbol{x}_a$, where $\boldsymbol{x}_a$ is a point on the vortex axis. Integrating first over the cross-section of the tube and then along its axis, we obtain the velocity as a line integral (figure 3.2.a)

$$\boldsymbol{u}(\boldsymbol{x}) = -\frac{\Gamma}{4\pi} \int \frac{(\boldsymbol{x} - \boldsymbol{x}_a) \wedge \mathrm{d}\boldsymbol{x}_a}{|\boldsymbol{x} - \boldsymbol{x}_a|^3} + \nabla\phi, \tag{3.6}$$

In the particular case of an infinite straight vortex along the x_3 axis, it is easy to show that (3.6) reduces to the two-dimensional Biot–Savart law (2.7), and that the velocity is azimuthal and decays as $\Gamma/2\pi R$, where R is the shortest distance to the vortex axis. In other cases, as long as R is much smaller than the radius of curvature ρ_0 of the axis of the vortex, the same approximation holds, and the velocity induced by a line vortex is roughly the same as if it were straight.

At distances to the axis of the same order as the radius a of the vortex core, the line-vortex approximation breaks down. This is in part the same phenomenon that we found in computing the self-interaction of a compact vortex in two dimensions, and also leads to the preferential formation of circular cross sections, but there is in this case a new, and more important, effect.

The formal approximation used in deriving the velocity due to a line vortex is an expansion in a/R, which is assumed to be a small quantity. We saw in comment 2.1, in chapter 2, that the correction to the two-dimensional point-vortex approximation is $O(a^2/R^3)$ but, in three dimensions, the first correction to (3.6) is

$$\boldsymbol{u}_{loc}(\boldsymbol{x}) = -\frac{\Gamma}{4\pi\rho_0} \log(R/a)\boldsymbol{b}, \tag{3.7}$$

where $\boldsymbol{b}$ is the local binormal to the vortex axis[1]. This is a relatively large term, that actually becomes infinite as we approach the axis. It has the effect of making

[1]The derivation of (3.7) is straightforward but laborious, and can be found in the book by Saffman (1992, pg. 36–39).

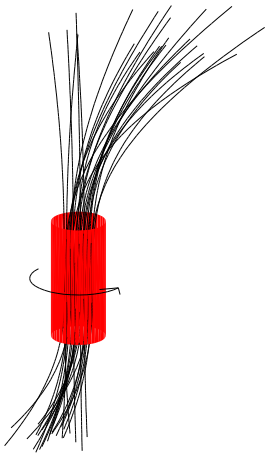

Figure 3.3: A coherent line vortex of finite length can be created if vortex lines bundle only along a short segment, but the individual vortex lines cannot end within the fluid.

curved parts of a line vortex rotate out of their plane (figure 3.2.*b*). The infinity is avoided because (3.7) is not applicable when $R \approx a$ but, at intermediate distances where $a \ll R \lesssim \rho_0$, this 'local induction' term is the dominant one. One of its consequences is that infinitely thin line vortices are formally ill-posed and physically meaningless, and that the only case in which they can be used is when their radii of curvature are known for other reasons to be everywhere large with respect to their radii. In particular they have to be used with care in turbulent flows, where we have seen that smooth geometries are rare.

It is also possible to create 'finite' equivalents of line vortices in which the vortex lines are tightly bundled only for a finite length and then splay open (figure 3.3), although the finite length is only apparent because the total circulation in the tube, whether compact or diffuse, has to remain constant. The closest equivalent to a compact vorticity source is a vortex ring, which is a vortex tube closing on itself, but its effect is weaker than that of the kernel of (3.1) because the vorticities on both sides of the ring have different signs, and their effects tend to cancel.

Another kinematic approximation that is sometimes useful is the vortex layer, which is the three-dimensional extension of the vortex sheets found in the last chapter. These are now oriented surfaces formed by vortex lines, and are subject to the same Kelvin-Helmholtz instability discussed in §2.2, which now leads to their break-up into arrays of vortex tubes. If we consider for example a flat uniform vortex layer, it is easy to show from symmetry considerations, and from the application of Stokes' theorem, that the velocity field is simply a velocity jump $\Delta U = \Gamma$ across the layer, where Γ is the circulation along a circuit surrounding a unit length of the layer in the direction normal to the vorticity. Note that, as opposed to the case of vortex tubes, there is no kinematic reason why Γ should be constant along a vortex layer.

Comment 3.2: A kinematic aspect of vorticity that is sometimes found to be useful in the

study of turbulent flows is that it gives a global measure of the viscous energy dissipation rate, which was found in (1.4) to be

$$\varepsilon = \frac{\nu}{V} \int_V |\nabla \boldsymbol{u}|^2 \, \mathrm{d}^3\boldsymbol{x}. \tag{3.8}$$

The following is a vector identity,

$$|\nabla \boldsymbol{u}|^2 = |\boldsymbol{\omega}|^2 + (\nabla \cdot \boldsymbol{u})^2 + \nabla \cdot (\boldsymbol{u} \cdot \nabla \boldsymbol{u} - \boldsymbol{u} \nabla \cdot \boldsymbol{u}). \tag{3.9}$$

In the incompressible flows which are the main subject of these notes, the divergence $\nabla \cdot \boldsymbol{u}$ of the velocity vanishes, and the squared magnitude of the velocity gradient differs from the enstrophy only by a quantity which is the divergence of a scalar. When we integrate both sides of the equation over a large volume for which the boundary fluxes are negligible, it therefore follows that

$$\varepsilon = \frac{\nu}{V} \int_V |\boldsymbol{\omega}|^2 \, \mathrm{d}^3\boldsymbol{x}. \tag{3.10}$$

Note that this does not mean that only the rotational parts of the velocity gradients contribute to the dissipation. Equation (3.10) expresses only a kinematic relation between the mean values of two quantities taken over a large volume. Locally the boundary fluxes are important, and the two quantities are not equal.

In fact, the average dissipation rate can equally well be expressed in terms of the *symmetric* part of the velocity gradient, which is locally independent of the vorticity. Define the rate of strain tensor $\boldsymbol{S}$ as

$$\boldsymbol{S} = (\nabla \boldsymbol{u} + \nabla \boldsymbol{u}^T)/2, \tag{3.11}$$

where the ^{T} superindex denotes the transpose. The following identity holds,

$$|\nabla \boldsymbol{u}|^2 = |\boldsymbol{S}|^2 + \frac{|\boldsymbol{\omega}|^2}{2}, \tag{3.12}$$

and can be combined with (3.10) to give

$$\varepsilon = \frac{2\nu}{V} \int_V |\boldsymbol{S}|^2 \, \mathrm{d}^3\boldsymbol{x}, \tag{3.13}$$

which is an expression for the dissipation that now appears to be independent of the vorticity.

A further consequence of (3.9) and (3.13) is that the *averaged* norms of the vorticity and of the rate of strain are kinematically proportionally to each other in an incompressible fluid,

$$\frac{1}{V} \int_V |\boldsymbol{S}|^2 \, \mathrm{d}^3\boldsymbol{x} = \frac{1}{2V} \int_V |\boldsymbol{\omega}|^2 \, \mathrm{d}^3\boldsymbol{x}, \tag{3.14}$$

even if they represent essentially independent aspects of the velocity gradient tensor.

In compressible flows there is an extra contribution to the energy dissipation rate which comes from the divergence of the velocity, and which is for example responsible for the dissipation in shock waves.

3.2 Dynamics

The main difference between two-dimensional and three-dimensional vorticity is however not in its kinematics, but in its dynamics. The reason why vorticity plays a special role in high Reynolds number flows is that it is proportional to the angular momentum of the fluid, and that the pressure gradient, which is the only force force in an incompressible inviscid fluid, is irrotational and unable to influence the angular momentum. Vorticity thus represents a conserved quantity, at least in the inviscid limit, and vortices are good candidates for the equivalent of 'objects' that can be individually followed as the fluid moves around.

Consider for example an ellipsoidal fluid volume, centred at $\boldsymbol{x} = 0$, which is small enough for the velocity to be well approximated by the first two terms of its Taylor expansion. The angular momentum with respect to the centre of the ellipsoid is

$$\boldsymbol{J} = \int \boldsymbol{x} \wedge \boldsymbol{u} \, \mathrm{d}^3\boldsymbol{x} = \int \boldsymbol{x} \wedge [\boldsymbol{x} \cdot \nabla \boldsymbol{u}(0)] \, \mathrm{d}^3\boldsymbol{x}, \tag{3.15}$$

which can be written as

$$\boldsymbol{J} = \int \boldsymbol{x} \wedge [\boldsymbol{S}(0) \cdot \boldsymbol{x}] \, \mathrm{d}^3\boldsymbol{x} - \frac{1}{2} \int \boldsymbol{x} \wedge [\boldsymbol{\omega}(0) \wedge \boldsymbol{x}] \, \mathrm{d}^3\boldsymbol{x}, \tag{3.16}$$

because it is true for any vector $\boldsymbol{b}$ that

$$\boldsymbol{b} \cdot \nabla \boldsymbol{u} = \boldsymbol{S} \cdot \boldsymbol{b} + \frac{1}{2} \boldsymbol{\omega} \wedge \boldsymbol{b}, \tag{3.17}$$

where the rate of strain tensor $\boldsymbol{S}$ is the symmetric part of the velocity gradient.

The first integral in (3.16) cancels because of symmetry, and the second one can be recognized as the classical expression for the angular momentum of a rigid body, with $\boldsymbol{\omega}/2$ playing the part of the angular velocity.

A similar argument shows that pressure forces cannot change $\boldsymbol{J}$. If $\boldsymbol{n}$ is the outer normal to the surface of the fluid element, the torque of the pressure forces is

$$-\int \boldsymbol{x} \wedge \boldsymbol{n} p(\boldsymbol{x}) \, \mathrm{d}^2\boldsymbol{x} \approx -p(0) \int \boldsymbol{x} \wedge \boldsymbol{n} \, \mathrm{d}^2\boldsymbol{x} - \nabla p(0) \int \boldsymbol{x} \cdot \boldsymbol{x} \wedge \boldsymbol{n} \, \mathrm{d}^2\boldsymbol{x}. \tag{3.18}$$

The first term cancels by a straightforward application of Gauss' theorem, and the triple product in the integrand of the second one is trivially zero. In general, forces which derive from gradients do not interact with the angular momentum.

3.2.1 *Vorticity stretching*

The fact that the conserved quantity is the angular momentum, and not the angular velocity, that is conserved means that three-dimensional vorticity can be amplified or damped if the shape of the fluid particles is changed by the flow. This most important effect is contained in the differences between the two- and three-dimensional evolution equations for the vorticity. Taking the curl of the Navier-Stokes equations we obtain

$$\partial_t \boldsymbol{\omega} + \boldsymbol{u} \cdot \nabla \boldsymbol{\omega} = \boldsymbol{\omega} \cdot \nabla \boldsymbol{u} + \nu \nabla^2 \boldsymbol{\omega} = \boldsymbol{S} \cdot \boldsymbol{\omega} + \nu \nabla^2 \boldsymbol{\omega}, \tag{3.19}$$

where we have used (3.17) for the second part of the equation. Be aware that, from now on, we will often abbreviate ∂_t for $\partial/\partial t$, and ∂_j for $\partial/\partial x_j$. The left-hand side of (3.19) is the same as in two dimensions, and states that the vorticity is advected by the local velocity, but the first term in the right-hand side is new, and modifies the advected vorticity even in the inviscid case.

To understand the importance of the new term, let us write the equation for the vorticity magnitude, $W = |\boldsymbol{\omega}|^2 = \omega_i \omega_i$, which is the three-dimensional generalization of the *enstrophy* that we already found already in problem 2.4. Multiplying (3.19) by $\boldsymbol{\omega}$, we obtain

$$\mathrm{D}_t W = 2\boldsymbol{\omega} \cdot \boldsymbol{S} \cdot \boldsymbol{\omega} + \nu(\nabla^2 W - 2|\nabla \boldsymbol{\omega}|^2). \tag{3.20}$$

The viscous part of this equation contains a diffusion term and an enstrophy dissipation similar to those in the energy equation. We will neglect them for the moment and concentrate on the new inertial term in the right-hand side. In that limit,

$$\mathrm{D}_t W = 2\boldsymbol{\omega} \cdot \boldsymbol{S} \cdot \boldsymbol{\omega}. \tag{3.21}$$

Comparing this equation with its two-dimensional counterpart (2.6) we encounter the main difference between two- and three-dimensional flows. While in the latter there is a mechanism for modifying the enstrophy, in the former there is none. This completely changes the behaviour of the flow with respect to energy conservation. Vorticity is part of the velocity gradient, and we have seen in comment 3.2 that, except for boundary terms, the magnitude of the velocity gradient and of the vorticity are equal in the mean. Having a way of modifying the latter means having a way of changing the former, and therefore having a mechanism for increasing the energy dissipation. While in two dimensions there was no obvious way of creating infinite velocity gradients, in three dimensions there is one, and a dissipation independent of viscosity becomes possible.

The behaviour of the enstrophy is best understood by studying the vorticity equation in the frame of reference formed by the eigenvectors of the rate of strain tensor. Since $\boldsymbol{S}$ is a real symmetric tensor, it has three orthogonal eigenvectors and three real eigenvalues. We will call them α_1, α_2 and α_3, in decreasing order. Since the diagonal elements of S_{ij} are $\partial_i u_i$, and we are assuming the fluid to be incompressible,

$$\alpha_1 + \alpha_2 + \alpha_3 = 0, \tag{3.22}$$

so that $\alpha_1 \geq 0$, $\alpha_3 \leq 0$ and α_2 can be either positive or negative. The inviscid form of (3.19) decouples in these axes into three independent equations,

$$\mathrm{D}_t \omega_{\alpha_j} = \alpha_j \omega_{\alpha_j}, \tag{3.23}$$

where no index summation is intended. Their solutions are

$$\omega_{\alpha_j} = \omega_{\alpha_j}(0) \mathrm{e}^{\alpha_j t}. \tag{3.24}$$

The behaviour of the enstrophy depends on the initial orientation of the vorticity vector. The vorticity components aligned with eigenvectors with positive eigenvalues are amplified exponentially, while those aligned with negative ones are damped. A randomly chosen initial vorticity vector will almost surely get eventually amplified, although it may initially be damped. This is because it would most likely have some component along α_1 which will grow indefinitely, while the other two can at most decay to zero. Note that this is not enough to conclude that vorticity is always amplified in the mean in real flows, since $\boldsymbol{S}$ is a function of time, and the exponential amplification may not have time to develop. Consider for example the case in which $\alpha_1 = \sin(\Omega t)$. The question of why gradients are preferentially amplified in real turbulence, driving energy towards the smaller scales, is discussed in some detail in chapter 5.

The intuitive reason for the change in the vorticity is explained in figure 3.4. Consider an initially spherical fluid particle whose vorticity $\boldsymbol{\omega}$ is aligned with the

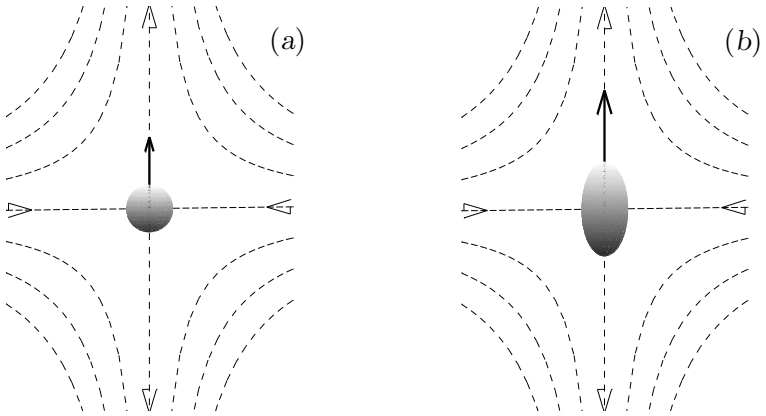

Figure 3.4: Stretching of vorticity by an irrotational straining field. An initially spherical fluid particle containing vorticity aligned with the stretching strain axis (a), is deformed into an ellipsoid whose moment of inertia decreases around that axis (b). Conservation of angular momentum then dictates that its angular velocity has to increase.

positive eigenvector of an irrotational straining field. Assume for simplicity that the strain is axisymmetric, so that $\alpha_2 = \alpha_3 = -\alpha_1/2$. This velocity will deform the fluid particle into an ellipsoid, stretching it along the positive eigenvector and compressing it along the other two. If the three semi-axes are called b_i, the two minor semiaxes evolve as

$$\mathrm{d}_t b_2 = -\alpha_1 b_2/2, \quad \Rightarrow \quad b_2 = b_3 = b_2(0)\mathrm{e}^{-\alpha_1 t/2}. \tag{3.25}$$

We saw in §3.2 that the angular momentum of a fluid particle is given by its vorticity times its moment of inertia, which is proportional to $b_2^2 \sim \exp(-\alpha_1 t)$. Since we also saw that pressure forces do not change the angular momentum, this implies that $\omega \sim b_2^{-2} \sim \exp(\alpha_1 t)$, in agreement with (3.24). Vorticity is amplified or damped because the flow stretches or compresses the fluid particles, changing their moment of inertia, and the corresponding vorticity components have to adjust. In two dimensions, the stretching and compression of the particles happen in the plane of the flow, while vorticity is always perpendicular to it. There is never a vorticity component in the direction of the stretching, and the enstrophy is conserved.

Note that the stretching term in (3.19) is linear in the vorticity, implying that the vorticity does not stretch itself. Vortices however generate velocities that may stretch other vortices, and this mutual interaction is the essence of the enstrophy amplification mechanism in turbulent flows.

As an example, the local induction velocity (3.7) of a line vortex does not stretch the line, because it is always directed along its binormal [PROBLEM 3.6], but parts of a line vortex generate velocities which stretch other parts. In the case of the hairpin-shaped vortex in figure 3.2(b) this means that the 'head' of the hairpin, where local induction is dominant, is not stretched as the vortex evolves but, as the head moves upwards, the trailing 'legs' behind it are stretched. Hairpin vortices

are important in the transition to turbulence in boundary layers and in other wall-bounded flows.

3.3 Viscosity and the Burgers' scale

Viscosity acts on three-dimensional flows in much the same way as it does on two-dimensional ones. A straight vortex line in a viscous fluid tends to get broader and weaker, as point vortices do in two dimensions. The same is true of vortex layers. The qualitative difference in three dimensions is that there is now another effect, stretching, which tends to make the vortex thinner, and the equilibrium between the two gives rise to a characteristic length scale which dominates vortical viscous flows. Consider for example a uniform vortex layer, defined by

$$\boldsymbol{\omega} = [0,\, 0,\, \omega(y)]. \tag{3.26}$$

This is essentially a two-dimensional object, and we saw in problem 2.9 that it evolves into a Gaussian vorticity profile whose width grows as $\delta \sim (\nu t)^{1/2}$. We can interpret this as defining a viscous time scale

$$T_\nu = \delta^2/\nu. \tag{3.27}$$

Note that this is the only time scale that can be formed with the layer thickness δ and the viscosity coefficient. Assume now that the layer is also subject to a straining field in the $x - z$ plane

$$\boldsymbol{u}_s = [0,\, -Sy,\, Sz]. \tag{3.28}$$

The vorticity equation (3.19) becomes

$$\partial_t \omega - Sy\partial_y \omega = S\omega + \nu \partial_{yy}\omega. \tag{3.29}$$

We have seen in (3.24) that, in the absence of viscosity, this would lead to an exponential growth of ω, with a characteristic time scale

$$T_S = S^{-1}. \tag{3.30}$$

From the conservation of the circulation, this implies that δ decreases exponentially with the same time scale. We can anticipate that, if the parameters are such that $T_S \ll T_\nu$, the stretching dominates and the layer gets thinner and stronger, while the opposite is true if $T_\nu \ll T_S$. The situation is sketched in figure 3.5, where the two time scales are plotted as a function of the thickness of the layer. It is clear from the figure that there is an intermediate thickness for which

$$T_S = T_\nu, \quad \Rightarrow \quad \delta = \delta_B = (\nu/S)^{1/2}, \tag{3.31}$$

where both effects are in equilibrium. Vortex layers of any initial thickness will tend to this state in times which are at most of the order of S^{-1}. The equilibrium 'Burgers' vortex layer has a Gaussian vorticity distribution, and the same is true of the corresponding axisymmetric equilibrium Burgers' vortex.

Problem 3.3: The results obtained in problem 2.5, in the previous chapter, can be generalized here to obtain the approach of a stretched vorticity layer to the Burgers' limit. Consider equation (3.29), and assume that the vorticity distribution is such that $y^n\omega(y)$ stays integrable at all times. Show that the circulation per unit length,

$$\Gamma = \int_{-\infty}^{\infty} \omega(y)\mathrm{d}y, \tag{3.32}$$

is constant. Define the layer thickness δ by

$$\Gamma\delta^2 = \int_{-\infty}^{\infty} y^2\omega(y)\mathrm{d}y. \tag{3.33}$$

Show that δ^2 satisfies a simple differential equation, independent of the detailed form of the initial vorticity distribution, and that its solution is

$$\delta^2 = \delta_B^2 + O\left(\mathrm{e}^{-2St}\right). \tag{3.34}$$

Compute the vorticity distribution for the equilibrium layer of thickness δ_B.

Solution: As in problem 2.5, the idea is to recast the evolution equation for the vorticity as a conservation equation for the different quantities of interest. For the circulation itself, for example, (3.29) can be written as,

$$\partial_t\omega = \partial_y(Sy\omega + \nu\partial_y\omega). \tag{3.35}$$

Upon integration in $y = (-\infty, \infty)$, the 'divergence' in the right-hand side vanishes, and (3.32) follows immediately.

In the same way, multiplying (3.29) by y^n, where $n \geq 0$, and integrating by parts, we obtain

$$\partial_\tau M_n + nM_n = n(n-1)M_{n-2}, \tag{3.36}$$

where $\tau = St$ is a dimensionless time based on the stretching rate, and

$$M_n = \frac{\int_{-\infty}^{\infty} y^n\omega(y)\,\mathrm{d}y}{\Gamma\delta_B^n}. \tag{3.37}$$

Note that $M_0 = 1$ and $M_2 = \delta^2/\delta_B^2$. Solving (3.36) for the latter yields directly (3.34). Assuming now in (3.35) that $\partial_t = 0$, the resulting ordinary differential equation is easily integrated to show that the vorticity distribution of the equilibrium Burgers' layer is Gaussian,

$$\omega(y) = \frac{\Gamma}{\sqrt{2\pi}\,\delta_B}\mathrm{e}^{y^2/2\delta_B^2}. \tag{3.38}$$

Comment: As in the second part of problem 2.9 it is possible to prove that any initial vorticity layer for which the moments (3.37) can be defined, tends eventually to the Gaussian Burgers' form (3.38). We will use a method which is slightly different from the one outlined for problem 2.9.

It is clear from the hierarchy of equations (3.36) that their solutions can be expanded in the form

$$M_n(\tau) = \sum_{m=1}^{n} A_{nm}\mathrm{e}^{-m\tau} + M_{nB} \tag{3.39}$$

where

$$M_{nB} = n(n-1)M_{n-2,B}, \tag{3.40}$$

and that there is a recursive hierarchy of equations that determines the A_{nm} as functions of the initial conditions. They are not needed for the long-term behaviour of the moments, since all the exponentials in the sum in (3.39) decay for long times, and the moments tend to M_{nB}. It follows from (3.32) and (3.34) that $M_{0B} = M_{2B} = 1$, and it is easy to show that $M_{1B} = 0$. The recursive formulas (3.40) then leads to

$$M_{2n,B} = 1 \times 3 \times \ldots (2n-1), \quad M_{2n-1,B} = 0. \tag{3.41}$$

It can be checked directly that these moments correspond to (3.38).

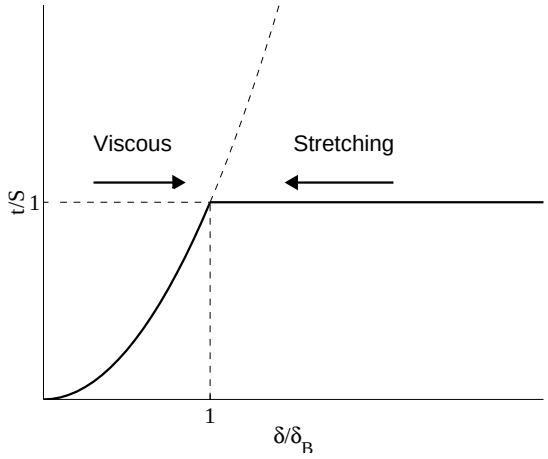

Figure 3.5: For a stretched viscous vortex layer, diffusion tends to thicken the layer, while stretching tends to thin it. The figure plots the time scales for both processes. For each layer thickness δ, the fastest process is dominant, and all the layers tend to the equilibrium situation at the Burgers' thickness δ_B.

The Burgers' length is the basic viscous length scale for vortical flows. If we know the magnitude S of the strains induced by a system of vortices on one another, we can conclude that structures which are much thinner or much broader than δ_B would not last for long times, and we should not expect to find them very often. In a random array of vortices most of the vorticity is at scales which are of the order of δ_B, and most of the coherent vortex structures are essentially equilibrium Burgers' vortices or layers. The only escape from this situation, which is not necessarily very uncommon, is for the time scale of the temporal variation of the straining velocity to be itself short or comparable to T_S, in which case there might not be time for the vorticity to reach its Burgers' limit.

We had already found in these notes the Burgers' length scale, although apparently in a different context. It follows from the expression (1.4) of the energy dissipation rate, and from the kinematic relations in comment 3.2, that the characteristic straining rate in a turbulent flow is $S = (\varepsilon/\nu)^{1/2}$, from where the Burgers' scale is

$$\delta_B = (\nu/S)^{1/2} = (\nu^3/\varepsilon)^{1/4}. \tag{3.42}$$

This is the Kolmogorov viscous length η defined in (1.19), and the time-scale arguments used in that occasion were essentially equivalent to the ones used here.

There is an interesting consequence of this equivalence between the Kolmogorov and the Burgers lengths. Consider the magnitude of the velocity gradient within an equilibrium vortex layer, which is $\Omega = \Gamma/\delta_B$, and compute the characteristic dissipation per unit volume,

$$\varepsilon = \nu\Omega^2 = \nu\Gamma^2/\delta_B^2 = \Gamma^2 S. \tag{3.43}$$

Note that this dissipation is independent of the viscosity coefficient, suggesting a possible mechanism for turbulent dissipation. Note also that we do not need any correction in this computation to account for the volume fraction filled by the layer, because volume is conserved in the deformation of incompressible fluids. An even more dramatic example is provided by the axisymmetric equilibrium Burgers' vortex, for which it can be shown that the dissipation becomes infinite as $\nu \to 0$.

Problem 3.4: Repeat exercise 3.3 for an axisymmetric vorticity distribution subject to the straining velocity field

$$\boldsymbol{u} = [-Sx/2,\, -Sy/2,\, Sz],$$

and compute the energy dissipation rate in a single Burgers' vortex when $\nu \to 0$.

3.4 The cascade argument revisited

We are now ready to revisit the Kolmogorov argument that was used in the introduction to justify the asymptotic behaviour of the energy dissipation. The main result was the scaling law for the velocity

$$u_\ell \sim (\varepsilon \ell)^{1/3}, \tag{3.44}$$

known as the Kolmogorov (1941) power law, and one of the few quantitative results in turbulence that were first derived theoretically and only later found to agree with experiments (see figure 1.6). No proof of (3.44) is known, but one of the lessons that we should draw from the course up to now is that Kolmogorov's arguments, even if not rigorous, were at least plausible. We saw in chapter 2, for example, that estimating the characteristic decay times for the eddies in terms of averages is justified, because systems with many degrees of freedom quickly lose memory of their origin, and can be treated as statistical ensembles. We also saw that vortices, which behave approximately as individual objects when seen from afar, provide the many degrees of freedom which are the causes of chaos.

We have seen that vortex sheets are unstable, and that they break down with characteristic times which are of the order $\tau_\ell \sim \ell/u_\ell$, which is the time scale needed to maintain a self-similar cascade. That, which confirms the dimensional argument, would still not guarantee that the net effect of the breakdown is to transfer energy to the smaller scales, which was the explanation given in the introduction for the non-zero limit of the energy dissipation rate when the viscosity vanishes. Two-dimensional turbulence, which is the chaotic evolution of two-dimensional vorticity briefly described in the discussion of figure 2.7, has all the characteristics mentioned up to now, but it does not dissipate energy when $\nu \to 0$. The reason is that there is no mechanism in two dimensions for increasing the magnitude of the vorticity, and, since it we have seen in this chapter that the vorticity modulus is a measure of the mean magnitude of the velocity gradients, the latter stay bounded, and the dissipation

$$\varepsilon = \nu \langle |\nabla \boldsymbol{u}|^2 \rangle, \tag{3.45}$$

vanishes when the viscosity does.

In fact, in two dimensions, the vortices increase their size as they merge, and the result is an *inverse* cascade of energy to larger scales. The similarity arguments used to derive (3.44) still apply, and the two-dimensional velocity fluctuations also satisfy that law for those distances at which the inverse cascade dominates. The energy is however not transferred towards the small scales subject to viscous dissipation, but away from them. If there is no mechanism to damp the flow without the help of strong gradients (e.g. bottom friction), the energy accumulates at the largest scales that fit into the particular system under consideration. This should warn us that the presence of chaos and the existence of instabilities are not enough to guarantee the presence of an energy cascade, or to determine its direction. They allow us to draw conclusions about how such a cascade behaves, but only once its existence is established by other mechanical arguments. The physical effects that determine the direction of the cascade in three-dimensional flows will be discussed in chapter 5. A good summary of the phenomenology of two-dimensional turbulence, which has many applications in meteorology and geophysics, can be found in the book by Lesieur (1997).

3.5 Vortex interactions

Although the examples given earlier in this chapter of the evolution of particular vortex structures are useful in understanding the general behaviour of three-dimensional vorticity, it is not clear how relevant coherent vortices really are in turbulent flows. Coherent vorticity filaments which are thin and very intense have been observed in turbulent flows, and they agree well with the Burgers' equilibrium analysis. It is on the other hand not clear whether there is enough of them to explain a substantial fraction of the energy dissipation, although it is known that they are relevant for the observations of strong intermittent events in high-Reynolds number turbulence (see the discussion in the book by Frisch, 1995).

A temptation that must be resisted is to consider either vortex layers or vortex lines as permanent 'objects'. We have seen that vortex layers are unstable to Kelvin–Helmholtz instabilities, and that they break into filaments. Filaments are formally stable to small perturbations (Saffman, 1992), and they have relatively long lifetimes when found in turbulent flows, but we have seen that they break down when they are deformed with a radius of curvature which is of the order of their thickness.

More importantly, they also deform when they come close to each other and, as in two dimensions, they merge when their separation becomes too small. The consequences of the merging are different than in two dimensions. When two compact vortex cores merge in two dimensions, the result is a larger core, plus some debris. In three-dimensional space two line vortices only approach in general at a single crossing point, and the merging is local. The result is not a thicker vortex line, but that the two original vortices get tangled at the intersection, break momentarily, and then reconnect into new vortex lines (figure 3.6). These interactions, which change the topology of the flow, have been observed both experimentally and numerically, and appear to be the generic outcome when two line vortices approach

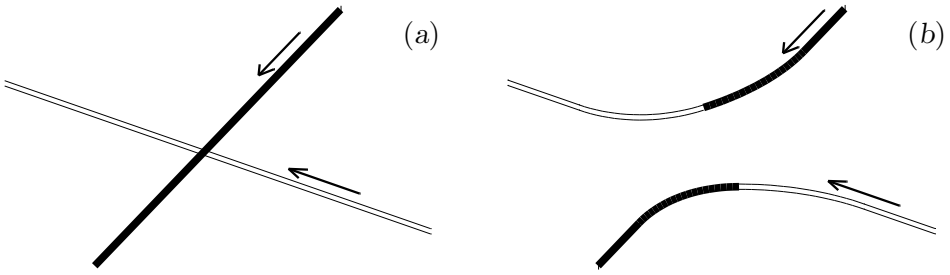

Figure 3.6: When two vortices come close to each other (a), they often reconnect (b), changing their topology.

each other.

They are fairly violent events generating a lot small-scale debris, and result in the dissipation of a substantial fraction of the energy, and in an appreciable reduction of the length of the original vortices. The fact that vortex filaments are observed to last for relatively long times in turbulent flows, in spite of all the possible interactions leading to their decay, suggests that they are relatively uncommon and interact fairly rarely.

3.6 The effect of walls

We saw in the discussion of the Biot–Savart law (3.1) that walls can influence the behaviour of an inviscid vortical flow through the generation of the boundary conditions for its potential component, and we have stated several of our results concerning the evolution of vorticity with the caveat that walls should not be present. We are now in a position to examine this limitation more carefully. Consider a vortical viscous fluid within a closed vessel. The boundary condition at the wall is that all the components of the velocity should vanish, implying that

$$\nabla\phi = -\boldsymbol{u}_\omega. \tag{3.46}$$

We are now in a quandary, because we have seen that Laplace's equation only admits one boundary condition, while (3.46) appears to give us three, one for each component. The problem is real, and implies that the vorticity distribution in a viscous fluid cannot be arbitrary in the presence of a wall.

The initial vorticity distribution, together with the impermeability condition, fully determines the velocity everywhere, including a tangential velocity at the wall which is in general not zero, and which does not therefore satisfy the viscous boundary condition. The problem is most easily seen in terms of circulation. Since the tangential velocity at the wall is zero, the circulation along any closed line in the boundary vanishes, and it follows from Stokes' theorem (3.5) that the vorticity flux across any surface which divides the vessel in two should also vanish. If the initial vorticity distribution does not satisfy that condition, as it generally would not, new vorticity has to be created. This happens near the wall in the form of thin boundary layers, which thicken under the action of viscosity and become part of the

general vorticity distribution within the vessel. As these new 'secondary' vortices move around, they create new boundary layers and new vorticity, leading in some cases to the complete modification of the initial vorticity distribution.

There is no a-priori limit to the amount of secondary vorticity generated in this way, except of course that the circulation has to remain compatible with the boundary conditions. There are examples, such as the collision of a diffuse vortex with a thin wire, in which the enstrophy at the end of the collision can exceed the initial one by orders of magnitude.

Note that this enstrophy production mechanism is not restricted to three-dimensional flows, and we already remarked in §2 that the monotonic decay of the vorticity extrema in two dimensions is not satisfied in the presence of walls. In fact, since Kelvin's theorem insures that an initially irrotational flow stays irrotational in the absence of walls and of body forces, most of the vorticity in both two- and three-dimensional constant-density flows originates at viscous walls.

SUPPLEMENTARY PROBLEMS

Problem 3.5: Show that the solution of Laplace's equation (3.2) in a closed domain, with a given wall-normal derivative, is unique except for an additive constant which does not influence the velocity.

Hint: Assume that there are two different solutions, ϕ and $\phi + \phi_1$. Their difference ϕ_1 would satisfy (3.2), with $\boldsymbol{n} \cdot \nabla \phi_1 = 0$ at the boundary. Apply the divergence theorem to the vector $\phi_1 \nabla \phi_1$.

Problem 3.6: Prove that a line which moves with a velocity directed along its binormal, such as in the local induction approximation (3.7), does not change its length. You will have to use the Frenet formulas for a line $\boldsymbol{x}(s)$, which relate the tangent vector $\boldsymbol{t}$ to the normal $\boldsymbol{n}$ and the binormal $\boldsymbol{b}$,

$$\mathrm{d}_s \boldsymbol{x} = \boldsymbol{t},$$

$$\mathrm{d}_s \boldsymbol{t} = \boldsymbol{n}/\rho_0, \qquad \mathrm{d}_s \boldsymbol{n} = -\boldsymbol{t}/\rho_0 + \tau \boldsymbol{b}, \qquad \mathrm{d}_s \boldsymbol{b} = -\tau \boldsymbol{n},$$

where s is the arc-length and τ is the torsion.

Hint: Define a Lagrangian coordinate ξ along the line, such that

$$\partial_t \boldsymbol{x}(\xi,\, t) = \boldsymbol{u},$$

and $\boldsymbol{u}$ is given by (3.7). Show that

$$\partial_t |\partial_\xi \boldsymbol{x}|^2 = 0,$$

and argue that this implies that the length of the line remains constant.

Chapter 4

Statistical tools

Summary

We mentioned at the end of chapter 2 that the sensitivity of turbulent flows to the details of the initial conditions makes them good candidates for a statistical description. In using statistics we drastically decrease the amount of information about the flow that we are willing to consider. In particular, the vortices that we studied in the last two chapters are lost as individual structures, and we are only left with collective trends. This is however all we may want in many cases. In designing a pipe, for example, we generally do not need to know the individual history of fluid particles, but only the mean pressure drop.

In this chapter we consider how to describe fields statistically. There are three sections. The first one studies how to characterize the flow at individual points, while the other two present two different ways of describing the relations between flow variables at two neighbouring locations.

Contrary to the three previous chapters, this one contains no physics. It deals with the language used in turbulence, and it is necessary to understand what will be said in the rest of the course. With this chapter we leave the field of fluid mechanics in general, and enter into subjects with are specific to turbulent flows as such.

The tools described here are not restricted to turbulence. They are also used in analyzing other complicated phenomena, from the variations of the climate (a consequence of atmospheric turbulence) to economic and social data (presumably a manifestation of a different kind of turbulence).

4.1 Statistical distributions

Before we discuss how to describe the statistical properties of a system, we have to define the nature of our statistics. Assume that we want to find the mean value of the velocity at one point. This only makes sense if we have several experiments to take the average, and if those experiments are in some sense equivalent and independent of each other. The discussion in chapter 2 gave us an example. Experiments which only differ in the initial conditions are in practice equivalent, because they only

differ in details which are outside of our control. This is not an absolute concept. We may find that different sets of initial conditions give results which are different for sufficiently long times to be relevant for some particular application, and we may therefore decide to subdivide our statistics into different classes. What constitutes a homogeneous statistical set depends on the application.

Consider for example the climate in some city. Policy-makers interested in the possibility of global warming may want to know how the year-round average temperature has changed during the past century. Tourists planning to visit the city for a few days in June would however not usually consider all the months in the year as equivalent, and would be more interested in what has been the mean temperature during the month of June in the last decade. Finally, for geologists studying slow processes such as the formation of clay, changes over a few centuries are irrelevant, but they may want to differentiate between the climate during glacial and inter-glacial periods, each lasting a few thousand years.

Whichever is our definition of statistical equivalence, it is often useful to think of a turbulent flow as a particular realization of a class of random fields, each of them originating from different initial conditions, and to use statistics over those different solutions to study the properties of the class. This *ensemble* average is in general the right definition to use but, in practice, other definitions are more useful. If the equations of motion and the boundary conditions are independent of time, different instants of a single history can be used as approximately uncorrelated initial conditions, each of them generating a time-shifted version of the same history. For such *statistically stationary* turbulent flows, an average taken over time at a given point can be used as a substitute for the ensemble average.

Similarly, flows whose boundary conditions are uniform in some spatial direction are often *statistically homogenous* in that direction, and spatially shifted versions of the same field can also be used as uncorrelated experiments. This would for example be the case along the axis of an infinitely long pipe, but not along its radius. In those cases spatial sampling along the homogeneous directions can be used as a substitute for ensemble statistics. The same is true for *statistically isotropic* conditions, in which the problem is invariant to changes in the orientation of the axes.

An extreme case is when the flow is both statistically homogeneous and isotropic. Ensemble, spatial and directional averaging are then all equivalent, and the statistical structure of the flow is specially simple. It may appear difficult to produce experimental situations with those characteristics, since some kind of inhomogeneity must be introduced to drive the turbulence, but we will see in the next chapter that such flows are useful representations of the small turbulent scales, because the small eddies have gone through enough stages of the cascade to forget their original locations and orientations. In these notes we will use whichever statistics make sense for the problem at hand, without specifying them in detail.

The simplest characterization of the statistics of a scalar quantity x at one point is its 'probability density function' (p.d.f.). Assume that we take a large number N of independent measurements of x, and classify the results into 'bins', such that a measurement is counted in bin i if $x_i - \Delta x/2 < x \leq x_i + \Delta x/2$. The

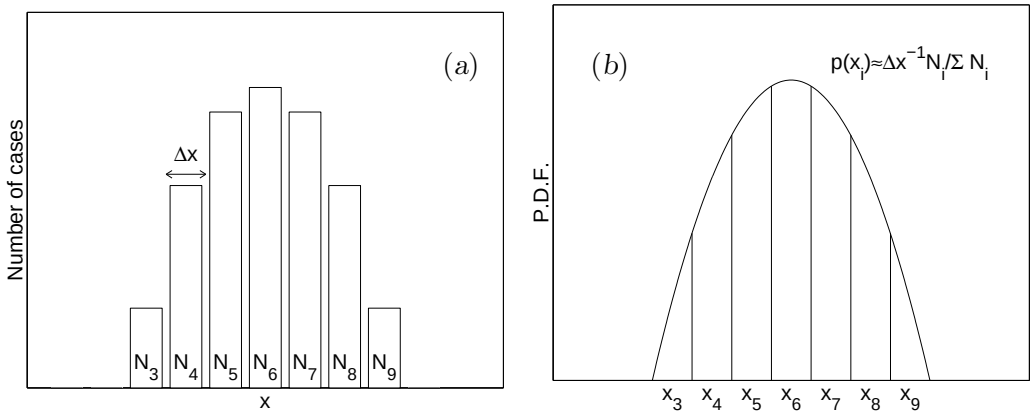

Figure 4.1: (*a*) Histogram of the measurements taken in a particular set of experiments. The *frequency* $N_i/\sum N_i$ with which past data fall in the i-th bin gives an idea of the *probability* that a future measurement will fall in that particular bin. (*b*) The probability density function of the variable x is designed to make histograms independent of the width of the bins used to compute them.

frequency $P(i;\, N) = N_i/N$ with which measurements fall in a given bin of such a 'histogram' gives an idea of the probability that any future measurement on the same system will give results falling in that bin (see figure 4.1-*a*). The central assumption of statistics is that the histogram converges to a limit

$$\lim_{N\to\infty} P(i;\, N) = P_i \tag{4.1}$$

when N is large enough, so that the probabilities P_i can be defined, and that, if we conducts two independent sets of experiments on a system, the two histograms converge to the same values. From their definition, probabilities satisfy

$$\sum_i P_i = 1. \tag{4.2}$$

The probabilities defined in this way are only moderately useful in describing physical systems because they depend on the way that the histogram has been constructed. It is clear that, if we had chosen fewer wider bins, the probability of getting measurements in a given bin would generally have been higher. It is often the case in physical systems that the dependence of the probability on the bin position is a smooth function, in which case P_i is approximately proportional to the width of the bin. In the limit of infinitesimally thin bins we can then define a 'density function' such that the probability of finding the variable in the interval $(x,\, x + \mathrm{d}x)$ is $p(x)\,\mathrm{d}x$ (see figure 4.1-*b*). The equivalent of the normalization condition (4.2) is then

$$\int_{-\infty}^{\infty} p(x)\,\mathrm{d}x = 1. \tag{4.3}$$

The p.d.f. completely characterizes the 'one-point' statistics of a variable. Assume for example that we need to compute the average value of x, which is defined for the N measurements $x^{(j)}$ as

$$\langle x \rangle = \frac{1}{N} \sum_j x^{(j)}. \tag{4.4}$$

Since the frequency of a given outcome of the experiment is proportional to $p(x)$, we can reorganize the results into 'bins' of size Δx, centred at x_k, and compute (4.4) as

$$\langle x \rangle \approx \sum_k x_k \, p(x_k) \Delta x \approx \int_{-\infty}^{\infty} x p(x) \, \mathrm{d}x. \tag{4.5}$$

The approximation can be made as good as required by taking smaller bins and performing more experiments. (**Question:** *Can you see why more experiments are needed when the bins are made smaller?*)

In general, the average of any function $F(x)$ is given by

$$\langle F(x) \rangle = \int_{-\infty}^{\infty} F(x) p(x) \, \mathrm{d}x, \tag{4.6}$$

and the statistics of a variable are often given by means of such averages. An important example are the 'statistical moments',

$$\langle M_n \rangle = \langle x^n \rangle = \int_{-\infty}^{\infty} x^n p(x) \, \mathrm{d}x, \tag{4.7}$$

the most common of which, and the only one we will use in these notes, is the 'centred' second order moment, or variance,

$$\sigma_x^2 = \left\langle (x - \langle x \rangle)^2 \right\rangle = \left\langle x^2 \right\rangle - \langle x \rangle^2. \tag{4.8}$$

Its square root is the standard deviation, often called in turbulence the root-mean-square 'intensity' and, in the same way that the mean value gives an idea of the general magnitude of x, the standard deviation characterizes the magnitudes of the fluctuations of x with respect to its mean.

Problem 4.1: The importance of the statistical moments comes from the following property. Show that the mean value of any function $F(x)$ whose Taylor series is convergent enough, can be expressed as a properly weighted series of the moments of x. In this sense, the set of all the statistical moments completely defines the p.d.f.

Problem 4.2: The mean values of other functions of x can also be used to characterize the p.d.f. The mean value of the harmonic function $\exp(\mathrm{i}\kappa x)$, is called the 'characteristic' of $p(x)$, and is a function of a wavenumber κ. It follows from (4.6), that the characteristic function,

$$\widehat{p}(x) = \langle \exp(\mathrm{i}\kappa x) \rangle = \int_{-\infty}^{\infty} p(x) \exp(\mathrm{i}\kappa x) \, \mathrm{d}x,$$

is the Fourier transform of $p(x)$, and that it can be expressed as a power series in κ whose coefficients are proportional to the statistical moments. Since Fourier transforms can in general be inverted, this is another way to prove that, if that series converges, the set of all the moments defines the p.d.f. For more information of the theory of probability, see Feller (1971).

4.2 Correlations and structure functions

The mean value, $U = \langle u \rangle$, and the standard deviation $u' = \langle (u - U)^2 \rangle^{1/2}$, are examples of 'one-point' statistics of the velocity. They give an idea of its local behaviour, but they tell us little about its spatial structure. To study the latter we need 'multi-point' quantities involving the instantaneous velocities at two or more points.

We have used velocity differences in several occasions. In homogenous flows, the mean velocity difference between two points is zero (**Question:** *why?*), but we can use its root-mean-square value to characterize its magnitude. This is actually a good definition for the 'characteristic' velocity difference over a given distance,

$$u_\ell^2 = S_2(\ell) = \langle [u(x+\ell) - u(x)]^2 \rangle, \tag{4.9}$$

and we can use it to express quantitatively the cascade argument given in the introduction. It is an example of a wider class of statistical measures, called 'structure functions', which are the statistical moments of the velocity differences,

$$S_n(\ell) = \langle [u(x+\ell) - u(x)]^n \rangle. \tag{4.10}$$

Different structure functions give information on different aspects of the statistics. We have seen that the second-order structure function gives an idea of the magnitude of the fluctuations. The third-order one, and all the structure functions of odd orders, quantify the asymmetry of the probability distribution with respect to the mean. Higher-order structure functions tell us how probable are strong fluctuations with respect to weak ones. In these notes the emphasis will be on the magnitude of the fluctuations at different scales, and second-order structure functions will be sufficient.

They are often expressed in the form of correlations

$$R(\ell) = \langle u(x)\, u(x+\ell) \rangle, \tag{4.11}$$

which, for homogeneous statistics, are related to the structure function by

$$R(\ell) = \langle u^2 \rangle - \frac{1}{2} S_2(\ell). \tag{4.12}$$

The correlation at zero separation is the variance $\langle u^2 \rangle$, and it follows from (4.12) that the correlation of a variable with itself is always maximum at $\ell = 0$. When the separation is large, on the other hand, it is often true that the values of the variable at the two points are statistically independent, in which case

$$R(\ell) = \langle u(x)\, u(x+\ell) \rangle = \langle u(x) \rangle \langle u(x+\ell) \rangle = \langle u \rangle^2. \tag{4.13}$$

For this reason, correlations are usually computed for variables whose mean is zero, in which case the correlation vanishes at large distances, and the separation at which it does can be used as a measure of the 'coherence length' of the variable [PROBLEM 4.3]. A common definition for the correlation length is

$$L_0 = \frac{1}{R(0)} \int_0^\infty R(\ell)\, \mathrm{d}\ell, \tag{4.14}$$

Problem 4.3: The correlation functions of fields which are not random may not decay to zero at long distances. Show for example that the correlation function of

$$u = \sin x \quad \text{is} \quad R(\ell) = \frac{1}{2}\cos \ell.$$

You may need to show first that $\langle \sin(kx)\sin(k'x)\rangle = 0$, unless $k = k'$. Interpret the reason for the periodic behaviour of $R(\ell)$. Show that the correlation function for

$$u = \sum_{k=1}^{\infty} a_k \sin(kx), \quad \text{which is} \quad R(\ell) = \frac{1}{2}\sum_{k=1}^{\infty} a_k^2 \cos k\ell, \tag{P4.1}$$

is also periodic in ℓ, but that the same is not true for

$$u = \sum_{k=1}^{\infty} a_k \sin(x/k).$$

Explain why. Write a computer program to plot the correlation of this function when

$$a_k = k\exp(-k/n),$$

and show that the correlation is noisy, but falls to small values outside a central peak whose half-width is approximately n. Interpret this result.

The quantity u_ℓ in (4.9) is usually taken to represent the magnitude of the velocity differences over a distance ℓ (although it is actually an integral of the velocity differences over distances equal or smaller than ℓ), but it is important to understand that neither the correlation nor the structure function say anything about the *location* of the structures. The correlation (4.11) would be exactly the same if the velocity were translated as a block by an arbitrary amount.

All these definitions can be generalized to inhomogeneous situations in which R is a function both of x and of ℓ, and to separations in time rather than in space, but it is more interesting for our purpose to extend them to vector quantities and to vector separations $\boldsymbol{\ell}$. If $\boldsymbol{u}$ is a vector with components u_i, we can define

$$R_{ij}(\boldsymbol{\ell}) = \langle u_i(\boldsymbol{x})\, u_j(\boldsymbol{x}+\boldsymbol{\ell})\rangle, \tag{4.15}$$

with an equivalent definition for the second-order structure function. For statistically homogeneous fields, R_{ij} is a symmetric tensor field, in the sense that $R_{ij}(\boldsymbol{\ell}) = R_{ji}(-\boldsymbol{\ell})$ (**Question:** *why?*).

The diagonal terms of the zero-separation correlation tensor are the mean-square intensities of the three vector components. In the case of the velocity, the sum $R_{ii}(0)/2$ is the kinetic energy. Here, and from now on, repeated indices imply summation. The cross terms $R_{ij}(0)$, with $i \neq j$, measure the correlation between different components of the velocity, and we will meet them again later. With the name of Reynolds stresses they measure the momentum fluxes due to the turbulent fluctuations. Note that the symmetry relations mentioned in the previous paragraph imply that the correlation tensor at zero separation is fully symmetric. They also imply but that the diagonal components of the correlation are even functions of $\boldsymbol{\ell}$, whose maximum is at the origin, but the same is not true for the off-diagonal components, which are not necessary symmetric functions of $\boldsymbol{\ell}$, and whose maxima can be anywhere.

It is intuitively clear that there are cases in which not all the components of the correlation tensor are independent, and in which their dependence on the separation vector is constrained. A case of some importance is when the underlying vector field is statistically isotropic, in which case the correlation can intuitively only depend on the magnitude $\ell = |\boldsymbol{\ell}|$ of the separation. The details are beyond the scope of these notes, but they are given in appendix B for reference. The result is that there are only two independent functions of ℓ, from which all the components of the correlation tensor can be derived. They are the 'longitudinal' structure function of the velocity component parallel to the separation vector, for example $R_{11}(\ell_1)$, and the 'transverse' structure function of the velocity components normal to the separation vector, such as $R_{22}(\ell_1)$. In the particular case of the velocity differences in incompressible flow, the extra constraint of incompressibility reduces these two independent functions to a single one.

The velocity differences plotted in figure 1.6 of chapter 1 were the square root of the second-order longitudinal structure function of the velocity differences in nominally isotropic turbulence, and equation (1.18) in chapter 1 can properly be expressed as

$$S_2(\ell) = C_1^2(\varepsilon\ell)^{2/3}. \tag{4.16}$$

The proportionality constant is empirically $C_1 \approx 1.4$.

In problem 4.6 at the end of this chapter you will find a worked example of how the structure functions of the velocity differences can be used to compute one-point statistics of the velocity gradients, such as the dissipation. It is clear that it has to be that way since, in the limit of very short separations, the structure functions describe the relative behaviour of points which are infinitesimally close to each other.

4.3 Spectra

The velocity distribution among eddies of difference sizes can also be expressed in terms of spectra. Fourier theory is a well-developed field of classical analysis, and the present summary is only a qualitative introduction to its application in the representation of turbulent velocities. We will assume that the flow is spatially periodic in some large box of size L^3, and approximate the resulting series by integrals. A discussion independent of that artifact can be found, for example, in §2 of Batchelor (1953) or in §6 of Monin & Yaglom (1975). A summary of the relevant formulas is given in appendix A.

Briefly, the wavenumber associated to a length scale ℓ is $\kappa = 2\pi/\ell$, and the velocity components, u_j, are expressed as Fourier series or integrals. For functions of a single spatial coordinate we can for example define

$$u(x) = 2\pi L^{-1} \sum_m \widehat{u}_m \exp(2\pi \mathrm{i} m x/L) \approx \int_{-\infty}^{\infty} \widehat{u}(\kappa) \exp(\mathrm{i}\kappa x)\, \mathrm{d}\kappa, \tag{4.17}$$

although, as explained in appendix A, other normalizations may sometimes be more convenient. For functions of the three spatial coordinates, (4.17) is trivially general-

ized by substituting κ by a three-dimensional wave-vector with components κ_n, and the argument of the exponential by the scalar product, $\mathrm{i}\kappa_n x_n$. The Fourier integral becomes a triple integral over the three-dimensional wavenumber space.

The Fourier representation is only practical for spatially homogeneous fields, since the exponentials on which it is based are essentially invariant to translations. If a flow is statistically homogeneous in some directions but not in others, it makes sense to use mixed expansions which are only Fourier-like over some coordinates.

The practical importance of Fourier expansions in signal representation is due to the simple way in which they express the energy associated to a given range of scales. The Fourier expansion (4.17) can be interpreted as the expression of the infinite-dimensional 'vector' $\boldsymbol{u} = u(x)$ in terms of a particular set of orthogonal basis vectors. The usual representation of a function by its value at each point can be seen as its expansion over the 'collocation' basis formed by Dirac delta functions, such that the value $u(x)$ is the 'component' of $\boldsymbol{u}$ over the basis vector $\delta(\xi - x)$. The Fourier coefficients $\widehat{u}(\kappa)$ can be similarly interpreted as the components of $\boldsymbol{u}$ over the exponential basis vectors $\boldsymbol{v}^{(\kappa)} = \exp(\mathrm{i}\kappa x)$, which are orthogonal with respect to the inner product

$$\boldsymbol{v}^{(\kappa')} \bullet \boldsymbol{v}^{(\kappa'')} = \langle v^{(\kappa')}(\boldsymbol{x}) v^{(\kappa'')*}(\boldsymbol{x}) \rangle. \tag{4.18}$$

The asterisk represents complex conjugation, and the average is taken over $\boldsymbol{x}$. The collocation basis is also orthogonal, so that the inner product of two vectors is in both cases a properly weighted sum of the products of their components. This leads to Parseval's theorem,

$$\boldsymbol{u} \bullet \boldsymbol{v} = \langle u(x)\, v^*(x) \rangle = 2\pi L^{-1} \int_{-\infty}^{\infty} \widehat{u}(\kappa)\, \widehat{v}^*(\kappa)\, \mathrm{d}\kappa. \tag{4.19}$$

In the particular case in which u is real and $u = v$, this formula represents the mean-square velocity, which can be expressed either as the sum of the squares of the velocity at each point, or as the sum of the squares of the absolute magnitudes of the Fourier transform. Note that this is just a generalization of Pythagoras theorem about the length of the hypotenuse in right-angled triangles.

It is then natural to interpret $|\widehat{u}(\kappa)|^2$ as an energy spectrum, proportional to the energy associated with the wavenumber κ. For real variables the energy spectrum is symmetric with respect to $\kappa = 0$, and is traditionally defined only for $\kappa \geq 0$. The proportionality constant in the definition of the spectrum is adjusted so that its integral is the mean-square value of the velocity. In the case of the one-dimensional spectrum of u_1 along x_1,

$$\langle u_1^2 \rangle = \int_0^{\infty} E_{11}(\kappa_1)\, \mathrm{d}\kappa_1. \tag{4.20}$$

Because u_ℓ, as defined in (4.9), is the contribution to the energy of the eddies up to size ℓ, the second order structure function and the spectrum contain identical information. This gives a practical way of computing the latter, which can be expressed as the Fourier transform of the correlation function,

$$E_{11}(\kappa_1) = \frac{2}{\pi} \int_0^{\infty} R_{11}(\ell) \cos(\kappa_1 \ell)\, \mathrm{d}\ell, \tag{4.21}$$

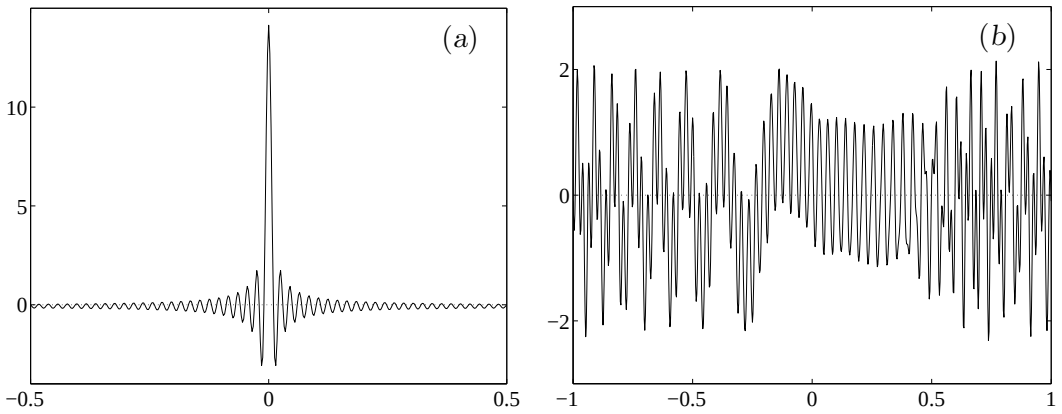

Figure 4.2: Two functions with identical power spectra but different relative phases of their Fourier components. (*a*) $u \sim \sum_{k=1}^{100} \cos k\pi x$. (*b*) $u \sim \sum_{k=1}^{100} \cos k\pi(x + k/57)$. Both functions are normalized to unit mean-squared amplitude.

Note that the inverse of this formula was already implicit in equation (P4.1) in problem 4.3.

It is possible to define one-dimensional 'cospectra' between different velocity components as

$$E_{ij}(\kappa_1) = \frac{1}{\pi} \int_0^\infty [R_{ij}(\ell) + R_{ji}(\ell)] \cos(\kappa_1 \ell) \, \mathrm{d}\ell = 4\pi L^{-1} \, \Re(\widehat{u}_i \widehat{u}_j^*), \tag{4.22}$$

where $\Re$ is the real part. The proportionally constant is again chosen so that

$$\langle u_i u_j \rangle = \int_0^\infty E_{ij} \, \mathrm{d}\kappa. \tag{4.23}$$

As in the case of the correlations, there is an underlying symmetric second-order spectral tensor which is discussed in more detail in appendix A. If the flow is statistically isotropic, not all the components of that tensor are independent, and the spectral energy density per unit volume in wavenumber space can only depend on the magnitude of the wavenumber. In that case, if the flow is also incompressible, all the components of the spectral tensor can be expressed in terms of a single 'three-dimensional' energy spectrum, $E(\kappa)$, whose interpretation is that the mean kinetic energy is

$$\frac{1}{2}\langle u_i u_i \rangle = \left(\frac{2\pi}{L}\right)^3 \iiint_\kappa |\widehat{u}_i^2|(\boldsymbol{\kappa}) \, \mathrm{d}^3\boldsymbol{\kappa} = \int_0^\infty E(\kappa) \, \mathrm{d}\kappa. \tag{4.24}$$

$E(\kappa) \, \mathrm{d}\kappa$ is the kinetic energy contained in the wavenumber 'shell' (κ, $\kappa + \mathrm{d}\kappa$). Details of the relevant formulas can be found in appendix B.

Most of the properties of correlations and structure functions have their counterpart in spectra. As was true of the former, spectra carry no information on the position of eddies within the velocity signal. Two Fourier expansions of the form (4.17) have the same spectrum if the magnitudes of all their coefficients are the same, but they may have very different forms if their phases are not (see figure 4.2).

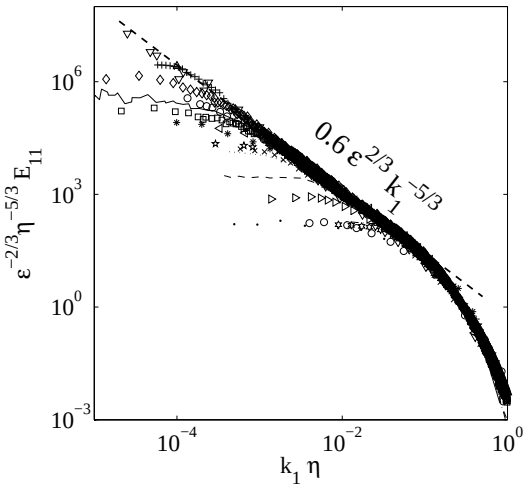

Figure 4.3: One-dimensional spectra of the longitudinal velocities for various shear flows and Reynolds numbers, displayed in Kolmogorov scaling. The dashed line is the inertial theory (4.25), with the constant in (4.16) set to $C_1 = 1.4$.

All the relations derived in the introductions for the structure functions of turbulent flows can be put in the form of spectra. In particular the cascade power law (1.18) or (4.16) corresponds to a different power law for the energy spectrum,

$$E_{11}(\kappa_1) = C_2 \varepsilon^{2/3} \kappa_1^{-5/3}, \tag{4.25}$$

where C_2 is an empirical constant which can be related to the one in (4.16). This is one of the most famous laws in turbulence, and it is how the results on the inertial cascade are usually presented. It is tested aginst experiments in figure 4.3. The details of how it is derived from (4.16) are instructive, specially regarding the treatment of the inner and outer cutoffs, and are given in the following problem.

Problem 4.4: Prove (4.25), find the interval of wavenumbers in which it is valid, and compute C_2 as a function of the constant C_1 in (4.16).

Solution: Write (4.16) as a correlation, using (4.12),

$$R_{11}(\ell) = \langle u_1^2 \rangle - \frac{C_1^2}{2} (\varepsilon \ell)^{2/3}, \tag{4.26}$$

and use the transformation formula (4.21) to obtain the spectrum. Assume that the velocities are normalized so that their mean value is zero. Note that (4.26) can only hold in a finite range $\eta < \ell < L_0$. At very short distances the velocity has to be differentiable (since it derives from the Navier-Stokes differential equations), and $S_2(\ell)$ has to be proportional to ℓ^2. For very long distances the two velocities in the definition of $R_{11}(\ell)$ are uncorrelated to each other and $R_{11}(\ell) = \langle u_1 \rangle^2 = 0$.

Observe that, if we forget those two limits and the presence of the additive constant $\langle u_1^2 \rangle$, the Fourier formula (4.21) becomes

$$E_{11}(\kappa_1) \approx -\frac{C_1^2 \varepsilon^{2/3}}{\pi} \int_0^\infty \ell^{2/3} \cos(\kappa_1 \ell)\, \mathrm{d}\ell. \tag{4.27}$$

The integral is convergent, and can be reduced be integration by parts to

$$E_{11}(\kappa_1) \approx \frac{2C_1^2}{3\pi}\varepsilon^{2/3}\kappa_1^{-5/3}\int_0^\infty x^{-1/3}\sin(x)\,\mathrm{d}x = \frac{\Gamma(2/3)C_1^2}{\pi\sqrt{3}}\varepsilon^{2/3}\kappa_1^{-5/3}, \tag{4.28}$$

where Γ is the gamma function, and which has the form of (4.25). If this approximation were accurate we would have

$$\frac{C_2}{C_1^2} = \frac{\Gamma(2/3)}{\pi\sqrt{3}} \approx 0.2488. \tag{4.29}$$

The additive constant $\langle u_1^2\rangle$ that we have neglected in (4.26) is of no importance, since the orthogonality of the Fourier components guarantees that its contribution to the integral vanishes except at $\kappa_1 = 0$. We however have to estimate the errors due to extending the integral beyond the range of validity of (4.26), and determine under what conditions they are negligible with respect to (4.28).

Since $S_2 \sim \ell^2$ near the origin, the correlation has the form $R_{11} \approx \langle u_1^2\rangle - C_\eta\ell^2$ for small ℓ, where C_η has to be chosen so that it matches (4.26) at $\ell \approx \eta$. This condition gives $C_\eta = O\left(C_1^2\varepsilon^{2/3}\eta^{-4/3}/2\right)$. The error in (4.27) due to this range is then of order

$$\frac{C_1^2\varepsilon^{2/3}\eta^{2/3}}{\pi}\int_0^\eta \left[(\ell/\eta)^{2/3} - (\ell/\eta)^2\right]\cos(\kappa_1\ell)\,\mathrm{d}\ell, \tag{4.30}$$

where, since $\ell < \eta$ in the integrand, the first term in the parenthesis is dominant. The relative error then becomes

$$\int_0^\eta \ell^{2/3}\cos(\kappa_1\ell)\,\mathrm{d}\ell, \quad \text{compared to} \quad \int_0^\infty \ell^{2/3}\cos(\kappa_1\ell)\,\mathrm{d}\ell, \tag{4.31}$$

or

$$\int_0^{\kappa_1\eta} x^{2/3}\cos(x)\,\mathrm{d}x, \quad \text{compared to} \quad \int_0^\infty x^{2/3}\cos(x)\,\mathrm{d}x. \tag{4.32}$$

Since the integrand is regular everywhere, the the relative error is only small if $\kappa_1\eta \ll 1$. A similar argument shows that the relative error due to the approximation made at large value ℓ is only small if $\kappa_1 L_0 \gg 1$, so that the range of validity of (4.25) is

$$\kappa_1\eta \ll 1 \ll \kappa_1 L_0, \tag{4.33}$$

which can be interpreted as those inertial wavenumbers whose wavelengths are much longer than the Kolmogorov eddies defined in chapter 1, and much shorter than the correlation length defined in (4.14).

Problem 4.5: Show, as in remark 1.4, in chapter 1, that (4.25) is the only dimensionally possible form for the spectrum if the only parameter available is the energy dissipation rate ε.

Anomalous power laws in structure functions indicate non-differentiable velocities, and the same is true for spectra. It can easily be proved that, if all the derivatives of a function are continuous, its spectrum decays at high wavenumbers faster than any power of κ. Power laws such as (4.25) indicate non-smoothness, and they can not be expected to hold for all κ. For wavelengths which are much shorter than the Kolmogorov dissipation scale, $\kappa\eta \gg 1$, viscosity smooths the velocity, and (4.25) turns into a decay which is at least exponential.

As already mentioned in the introduction, the reason for the appearance of power laws such as (4.25) is that the inviscid equations are invariant to geometric scaling, and that the important relations are those between a given length scale and its multiples, rather than between scales which differ by a fixed amount. It is for this reason that spectra and structure functions are often plotted in logarithmic

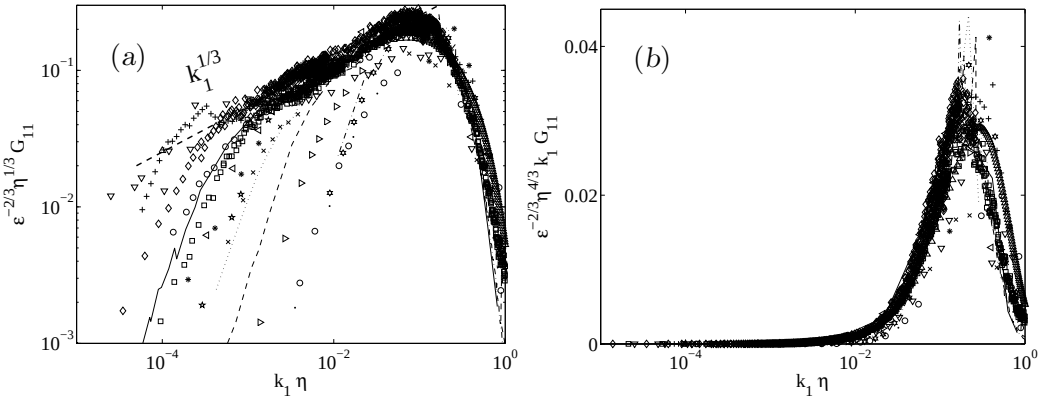

Figure 4.4: One-dimensional spectra of the streamwise derivatives of the streamwise velocity, $\partial_1 u_1$, for the same cases used in figure 4.3. Various turbulent flows and Reynolds numbers. (a) In logarithmic coordinates; (b) in premultiplied semilogarithmic coordinates. The plots are normalized in Kolmogorov units, which should collapse all the properties of the velocity gradients. The right-hand plot shows that most of the dissipation due to this velocity derivative resides around $\kappa\eta = 0.1$, or $\ell/\eta \approx 60$.

coordinates, such as in figures 1.6 and 4.4. The logarithm converts scaling factors into increments along the axes, and self-similar power laws are displayed as straight lines.

In doing so, that representation loses one of the useful graphic properties of the spectrum, which is to represent energies by integrals or by areas. To remedy that, it is sometimes useful to use semilogarithmic plots of the pre-multiplied spectrum, $\kappa_1 E_{11}(\kappa_1)$ versus $\log\kappa_1$. The extra factor in front of the spectrum compensates for the differential of the logarithm, and the integral property is restored,

$$\langle u_1^2 \rangle = \int_0^\infty \kappa_1 E_{11}(\kappa_1)\,\mathrm{d}(\log\kappa_1). \tag{4.34}$$

The areas underneath pre-multiplied spectra corresponds to energies, and spectral peaks show where the energy is concentrated. An illustration is given in figure 4.4, which displays spectra of the velocity derivative $\partial u_1/\partial x_1$. The spectrum of the latter is $G_{11} = \kappa_1^2 E_{11}$, because differentiation of a Fourier series is equivalent to multiplication by $\mathrm{i}\kappa_1$ [PROBLEM 4.6]. It then follows from (4.25) that

$$G_{11} \sim \varepsilon^{2/3}\kappa^{1/3}, \tag{4.35}$$

which increases with increasing wavenumber, and suggests that the velocity gradients should reside predominantly at the small scales (large wavenumbers). Since we have seen in previous chapters that the gradients are the cause of the viscous dissipation of the energy, and that they increase with decreasing length scale, this makes sense. In fact we saw in section 3.3 that at least one component of the velocity gradient, the vorticity, should reside near the Kolmogorov scale η. Figure 4.4(a) shows that

the experimental spectra of the velocity derivatives follow (4.35) within the inertial range, and that they collapse well in Kolmogorov units. The positive slope of the spectrum suggests that the gradients are concentrated at some small scale, but it is difficult to be precise where. The same data are shown premultiplied in figure 4.4(b), where the part of the spectrum contributing to the mean gradient, and therefore to the dissipation, is seen to be fairly narrow, centred near $\kappa\eta \approx 0.1$. Note that the length scales implied by this result are rather large, $\ell/\eta = 2\pi/(\kappa\eta) \approx 60$.

Problem 4.6: Spectra and correlation functions contain statistical information about the relative behaviour of the velocity field at two different points, and can therefore be manipulated to obtain statistical one-point moments for the derivatives. Consider for example how to compute the energy dissipation rate.

For a statistically homogeneous scalar function u of a three-dimensional space variable $\boldsymbol{x}$, whose correlation function is $R_{uu}(\boldsymbol{\ell})$, and whose spectrum is $E_{uu}(\boldsymbol{\kappa})$ show,

- That the correlation function of the derivative $\partial_j u = \partial u/\partial x_j$ is

$$R_{\partial_j u \partial_j u} = -\partial^2 R_{uu}/\partial \ell_j^2. \tag{P4.2}$$

- That the spectrum of the derivative $\partial_j u$ is

$$E_{\partial_j u \partial_j u} = \kappa_j^2 E_{uu}. \tag{P4.3}$$

Using the relations in appendix B for the spectral tensor of the isotropic velocity field in three-dimensional turbulence, show that the spectral density *per unit volume in wavenumber space* of the magnitude of the velocity gradient

$$|\nabla \boldsymbol{u}|^2 = \sum_i \sum_j (\partial_j u_i)^2,$$

is

$$D(\kappa) = \frac{E(\kappa)}{2\pi}, \tag{P4.4}$$

where $\kappa = |\boldsymbol{\kappa}|$, and $E(\kappa)$ is the three-dimensional isotropic energy spectrum. Derive from this the density $G(\kappa)$ of the magnitude of the gradient *per unit wavenumber magnitude*, and use this result to prove that the energy dissipation rate can be computed as

$$\varepsilon = \nu\langle|\nabla \boldsymbol{u}|^2\rangle = 2\nu \int_0^\infty \kappa^2 E(\kappa)\,\mathrm{d}\kappa. \tag{P4.5}$$

Use this formula to relate $E(\kappa)$ to the spectrum of vorticity magnitude.

Solution: To obtain (P4.2) write the correlation function for u and differentiate once with respect to ℓ_j

$$\partial R_{uu}/\partial \ell_j = \partial\langle u(\boldsymbol{x})u(\boldsymbol{x}+\boldsymbol{\ell})\rangle/\partial \ell_j = \langle u(\boldsymbol{x})\partial_j u(\boldsymbol{x}+\boldsymbol{\ell})\rangle. \tag{P4.6}$$

Because the problem is spatially homogeneous we can shift by $-\boldsymbol{\ell}$ the position where (P4.6) is applied, without changing its value,

$$\partial R_{uu}/\partial \ell_j = \langle u(\boldsymbol{x}-\boldsymbol{\ell})\partial_j u(\boldsymbol{x})\rangle. \tag{P4.7}$$

Differentiating again (P4.7) gives immediately (P4.2). Equation (P4.3) is then found by substituting this result into the Fourier formula (A.33), and integrating twice by parts with respect to ℓ_j,

$$E_{\partial_j u \partial_j u} = \frac{1}{(2\pi)^3} \int R_{\partial_j u \partial_j u}(\boldsymbol{\ell}) \exp(-\mathrm{i}\boldsymbol{\kappa}\boldsymbol{\ell})\,\mathrm{d}^3\boldsymbol{\ell}.$$

Applying (P4.3) to the derivative of u_i with respect to x_j, expressed in terms of the isotropic spectral density for u_i defined in appendix B, we get for the dissipation a spectral density per unit volume in three-dimensional wavenumber space

$$D(\boldsymbol{\kappa}) = \sum_i \sum_j \kappa_j^2 \phi_{ii} = \frac{E(\kappa)}{4\pi\kappa^4} \sum_i \sum_j \kappa_j^2 (\kappa^2 - \kappa_i^2) = \frac{E(\kappa)}{2\pi},$$

which is (P4.4). This spectral density satisfies that

$$\langle |\nabla \boldsymbol{u}|^2 \rangle = \iiint_\kappa D(\boldsymbol{\kappa}) \, \mathrm{d}^3\boldsymbol{\kappa}.$$

If we want to reduce it to an isotropic three-dimensional spectrum equivalent to $E(\kappa)$, defined in terms of the wavenumber magnitude, and satisfying

$$\langle |\nabla \boldsymbol{u}|^2 \rangle = \int_0^\infty G(\kappa) \, \mathrm{d}\kappa, \tag{P4.8}$$

we express the volume element in $\boldsymbol{\kappa}$ space as $4\pi\kappa^2 \, \mathrm{d}\kappa$, so that

$$G(\kappa) = 4\pi\kappa^2 D(\kappa) = 2\kappa^2 E(\kappa).$$

The energy dissipation rate is then found by integrating over all the wavenumbers κ,

$$\varepsilon = 2\nu \int_0^\infty \kappa^2 E(\kappa) \, \mathrm{d}\kappa.$$

Note that, from the result in remark 3.2, in the previous chapter, relating the dissipation to the vorticity magnitude, the integral in (P4.8) is also the mean value of the vorticity magnitude for *any* flow, $\langle |\omega^2| \rangle$, so that $G(\kappa) = E_{\omega\omega}$ can be interpreted as the three-dimensional spectrum of the modulus of the vorticity.

Chapter 5

The Kolmogorov cascade

Summary

In this chapter we begin to exploit the results of the cascade model using the quantitative tools developed in chapter 4. The chapter has two parts. In §5.1 we summarize the spectral representation of the turbulent energy, and classify the different spectral ranges. In §5.2 we extend the theoretical arguments to weakly anisotropic and inhomogeneous turbulence, and define the concepts of Reynolds decomposition and of Reynolds stresses. The tools developed in this chapter are the basis for all practical calculations of turbulent flows, and they arguably constitute the most important part of the whole course.

5.1 Spectral ranges in isotropic turbulence

While the discussion of the energy cascade could only be made qualitative in the introduction, we can now be more explicit. We saw in the last chapter that the power-law relation (1.18) can be expressed either in terms of the second-order structure function

$$S_2(\ell) = u_\ell^2 = C_1^2(\varepsilon\ell)^{2/3}, \tag{5.1}$$

or of the energy spectrum

$$E_{11}(\kappa_1) = C_2\varepsilon^{2/3}\kappa_1^{-5/3}, \tag{5.2}$$

and we computed the relation between the constants C_1 and C_2. Their value is most often given in terms of a third, isotropic, Kolmogorov constant C_K, which is the premultiplier of the isotropic three-dimensional energy spectrum introduced in section §4.3,

$$E(\kappa) = C_K\varepsilon^{2/3}\kappa^{-5/3}. \tag{5.3}$$

It follows from the isotropy relations given in appendix B that $C_1^2 \approx 1.3151\, C_K$. The experimental value is $C_K \approx 1.5 - 2$ (Monin & Yaglom 1975, 2: 351–355). Although no mathematical proof of these laws is known, we saw in chapter 3 that Kolmogorov's arguments were plausible, and we have also seen that his conclusions

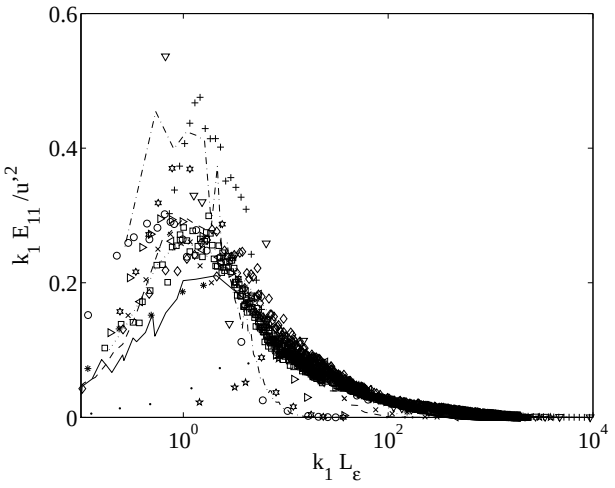

Figure 5.1: One-dimensional spectra of the longitudinal velocities for the same cases used in figure 4.4, displayed in premultiplied form, and in terms of the integral length scale. Various shear flows and Reynolds numbers.

agree reasonably well with the experimental evidence. Equations (5.1) and (5.2) remain the bases of turbulent theory.

We can now finish the classification, which was initiated in the introduction, of the different length scales found in turbulence, and recast it in terms of spectral distributions. Since we know that the energy spectrum generally decreases with increasing wavenumber, most of the energy is at low wavenumbers (large scales). It is for this reason that the velocity of the largest eddies can be characterized by the total kinetic energy, and is usually expressed in terms of the root-mean-square value of the fluctuations of one velocity component, $u' = \langle u_1^2 \rangle^{1/2}$. We assume in this section that $\langle u_j \rangle = 0$. For isotropic flows u' can be computed from the three-dimensional spectrum as

$$u'^2 = \frac{2}{3} \int_0^\infty E(\kappa)\, \mathrm{d}\kappa. \tag{5.4}$$

In the same way, we saw in problem 4.6 that the spectrum of the dissipation is proportional to $\kappa^2 E(\kappa)$, which increases with wavenumber as $\kappa^{1/3}$. The dissipation and the velocity gradients therefore reside in the small scales, of the order of the Kolmogorov length at which viscosity becomes important is

$$\eta = (\nu^3/\varepsilon)^{1/4}. \tag{5.5}$$

The characteristic magnitude of the velocity gradients is traditionally defined as the root-mean-square vorticity, which is given by (see comment 3.2 in chapter 3)

$$\omega'^2 = \langle |\boldsymbol{\omega}|^2 \rangle = \varepsilon/\nu = 2 \int_0^\infty \kappa^2 E(\kappa)\, \mathrm{d}\kappa. \tag{5.6}$$

At distances smaller than the Kolmogorov length viscosity is the dominant effect, and the flow is smooth. In that range of scales, the velocity field can be expanded

in Taylor series, and the velocity differences are of the order of

$$u_\ell \sim \omega' \ell. \tag{5.7}$$

In terms of the longitudinal second order structure function,

$$S_2(\ell) \approx \langle (\partial_{x_1} u_1)^2 \rangle \ell^2 = \omega'^2 \ell^2 / 15, \tag{5.8}$$

where the numerical factor can be derived exactly from the isotropy relations in appendix B. This equation was included as the dotted line in the compilation of structure functions in figure 1.6, and fits the data well.

At large distances, and generally wherever viscosity can be neglected, the energy transfer rate is of the order of $\varepsilon \approx u_\ell^3/\ell$, and we can use this relation to define an *integral* length L_ε, which characterizes the eddies at the large-scale end of the inertial range,

$$\varepsilon = \frac{u'^3}{L_\varepsilon}. \tag{5.9}$$

Since the cascade drains energy away from the large eddies, the maximum of the energy spectrum is always near those scales at which energy is injected into the flow by the external forces. The integral scale of an equilibrium turbulent flow is in this way determined by the energy injection mechanism, which also implies that the total dissipation is given by the velocity and by the length scales of the forcing, and is independent of viscosity. This is the essence of why the dissipation is independent of the Reynolds number, and probably one of the most important conclusions of the chapter; if the characteristic velocity and length of the driving forces are known, the energy dissipation rate can be estimated by (5.9), and from it all the characteristics of the inertial and dissipative ranges.

The scaling of the energy-containing eddies with the integral scale is checked in figure 5.1, which is compiled from the same data used in the last chapter to plot the spectra of the velocity derivatives. It is seen that the energy peak is indeed around $\kappa L_\varepsilon \approx 1$, but that the collapse of the different data is worse than it was for the gradients. Why this is so will be made clear later, after we discuss which features of the cascade are universal and which ones are not.

The ratio between the integral and the Kolmogorov lengths defines the extent of the inertial turbulent range. It follows from (5.9) and (5.5) that

$$L_\varepsilon/\eta = Re_L^{3/4}, \quad \text{where} \quad Re_L = u' L_\varepsilon/\nu, \tag{5.10}$$

is a large-scale Reynolds number. It is customary in isotropic turbulence to write this relation in terms of a different Reynolds number, defined for historical reasons as

$$Re_\lambda = (15 Re_L)^{1/2}. \tag{5.11}$$

This *microscale* Reynolds number can be written as $Re_\lambda = u'\lambda/\nu$ in terms of a length λ, intermediate between L_ε and η, which is called the Taylor microscale. The interest of this length scale is mainly historical, and it is seldom used except as in (5.11). Nothing special happens for example to the energy spectrum at $\ell \approx \lambda$. Note

that, if we consider each viscous eddy as a single object, (5.10) implies that the number of independent degrees of freedom in a volume L_ε^3 is

$$N_T \sim Re_L^{9/4} \sim Re_\lambda^{9/2}. \tag{5.12}$$

Fully turbulent flows require Re_λ to be larger than approximately 100, and one cannot speak of real turbulence below $Re_\lambda \approx 30$; the instabilities needed for the cascade do not develop in that regime. The highest Reynolds numbers, $Re_\lambda \approx 10^4$, have been measured in the atmospheric boundary layer, although indications of still higher ones have been found in astrophysical observations. Typical industrial flows have $Re_\lambda \approx 100 - 1,000$. The Reynolds number in the wake of a running person $Re_\lambda \approx 500$ and, in the boundary layer of a large commercial aircraft, $Re_\lambda \approx 3,000$. These are all large numbers, showing that most 'practical' flows are turbulent. They also imply that the number of degrees of freedom in most turbulent flows is large, potentially infinite in the high-Reynolds number limit.

Systems in which the number of degrees of freedom is finite are, in some sense, trivially solvable, since it is possible to write a computer program to simulate them as exactly as required. If the number is very large, that may be impractical, and a theoretical estimate might be more useful, but computers improve rapidly, and presently impractical simulations may become reasonable in the future. Problems like turbulence, in which the number of degrees of freedom can be made arbitrarily large by changing the parameters, cannot be fully solved in this way, and it is for them that genuine theories are required. The numerical techniques used to analyze turbulent flows at finite Reynolds numbers are described in chapter 7.

The Kolmogorov viscous length scales of high-Reynolds numbers flows are small, and get smaller as the viscosity decreases. It could be thought that, as $\nu \to 0$, the length η would tend to zero, and molecular effects should be taken into account. That is not true. We already saw in the introduction that the viscosity of gases is proportional to the mean path λ_m between the collisions of their molecules. Using the estimate for the viscosity of a gas given in comment 1.2, and the definitions of the different turbulent quantities, the ratio between the Kolmogorov scale and the mean free path is found to be

$$\frac{\eta}{\lambda_m} \approx Re_\lambda^{1/2} \frac{c}{u'}. \tag{5.13}$$

In most common cases the Mach number u'/c of the turbulent fluctuations is low, or at most of order unity, and this ratio is large. The result is that the Kolmogorov scale in subsonic turbulence is always much larger than the mean free path, and that, since the Navier–Stokes equations are valid in the limit in which the dimensions of the system are large with respect to λ_m, turbulence can be treated as a continuous phenomenon at all scales. The approximation becomes better at high Reynolds numbers.

Comment 5.1: Hypersonic turbulence. It could be thought that the previous conclusion could fail when Re_λ is not too high, or when the fluctuations are intense enough for their Mach number to be large. This may happen in hypersonic flows, especially since the viscosity of gases

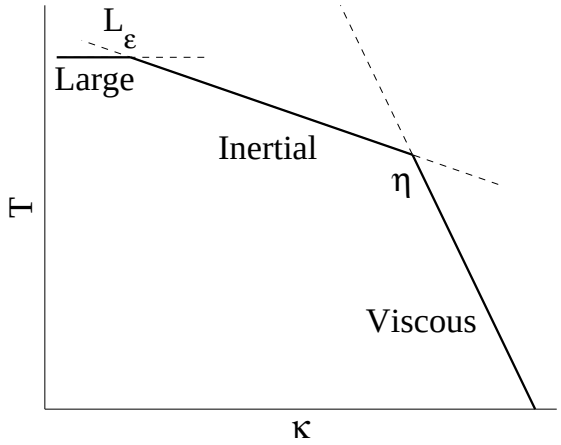

Figure 5.2: Time scales from table 5.1 for each of the different spectral ranges, plotted in terms of the wavenumber $\kappa \sim \Delta x^{-1}$. The different effects are active on all ranges, but the fastest one wins, and the relevant time scale for the flow is given by the heavy line.

increases with temperature, and hypersonic Reynolds numbers are not necessarily very large. This is also not true. An alternative way of expressing (5.13) in that case is

$$\frac{\eta}{\lambda_m} \approx \left(\frac{u'}{c}\,\frac{L_\varepsilon}{\lambda_m}\right)^{1/2}, \tag{5.14}$$

which shows that even hypersonic turbulence is described at all scales by the continuous equations as long as $L_\varepsilon \gg \lambda_m$. That is in any case the condition needed for the continuum approximation to be applicable to the largest scales.

The separation between the large scales containing the energy and the small ones responsible for the dissipation is what differentiates turbulent flows from other problems in which energy and dissipation are more closely associated. We can use that property to gain a better understanding of the form of the energy spectrum.

Consider the energy cascade as described in the introduction. When considering eddies small enough to be separated from the energy-injection scales by several instability steps, $\kappa L_\varepsilon \gg 1$, we can hope that all turbulent flows would be more or less similar. In this regime L_ε cannot be important, and in principle neither should be the Reynolds number. The spectrum should take the form,

$$E(\kappa) = u_K^2 \eta F_1(\kappa\eta), \tag{5.15}$$

where $u_K = \omega'\eta$ is the characteristic velocity difference across the Kolmogorov eddies, and F_1 should be universal.

Conversely, for eddies which are large enough for $\kappa\eta \ll 1$, viscosity cannot be important and the spectrum has to take a different universal form,

$$E(\kappa) = u'^2 L_\varepsilon F_2(\kappa L_\varepsilon). \tag{5.16}$$

Range	Length	Velocity	Velocity Gradient	Decay Time
Largest eddies	L_ε	u'	$u'/L_\varepsilon = \varepsilon/u'^2$	u'^2/ε
Inertial	ℓ	$u_\ell \approx 1.4(\varepsilon\ell)^{1/3}$	$u_\ell/\ell \sim (\varepsilon/\ell^2)^{1/3}$	$(\ell^2/\varepsilon)^{1/3}$
Kolmogorov	$\eta = (\nu^3/\varepsilon)^{1/4}$	$u_K = (\varepsilon\nu)^{1/4}$	$\omega' = (\varepsilon/\nu)^{1/2}$	$T_K = \omega'^{-1}$
Dissipative	ℓ	$\omega'\ell$	ω'	ℓ^2/ν

Table 5.1: Characteristics of the different spectral ranges of isotropic turbulence.

The spectrum of the eddies with are both large with respect to η and small with respect to L_ε cannot depend on any of the two length scales. The only available length is the wavenumber itself, and the only possible form of the spectrum is (5.3). The characteristic scales for the different spectral ranges are summarized in table 5.1. The time scales for the different eddy sizes are plotted in figure 5.2, and it is important to note that they decrease with decreasing eddy size. The consequence is that small scales tend to behave as if they were in equilibrium with the larger eddies which contain them. The small eddies evolve faster than the large ones, and have time to adjust to local equilibrium before the large eddies change appreciably. This is the theoretical justification for studying homogeneous turbulence as a building block for other flows, as well as the reason for the equilibrium approximation used in the cascade argument. It is also the reason why the Kolmogorov scaling (5.15) usually works well when collapsing experimental spectra from very different origins (see figure 4.3).

On the other hand, most real turbulent flows are driven by large scale forces, typically shear, which differ from one situation to another. Those driving mechanisms are not universal, and neither are the large scales that they produce. That is why the universality of the integral-length scaling (5.16) is not always as good as that of (5.15), as we can see by comparing the collapse of the different experiments in figures 5.1 and 4.4. On the other hand, it is true that the large-scale energy peak is independent of the Reynolds number.

Only when flows are forced in reasonably similar ways should their large and inertial scales collapse both in large- and in small-scale variables. This is illustrated in figure 5.3, which contains spectra from numerically-simulated forced turbulence at different Reynolds numbers. Since the forcing scheme is the same in all the simulations, both the large-scale normalization (5.16) and the Kolmogorov one (5.15) work well across the Reynolds number range. The main difference among the spectra is that the inertial range connecting the two limiting scales gets longer as the Reynolds number increases.

Problem 5.2: The decay of isotropic turbulence Even if the details of the large turbulent scales depends on the particular way in which the flow is forced, there are cases in which something can be said about their behaviour from general principles.

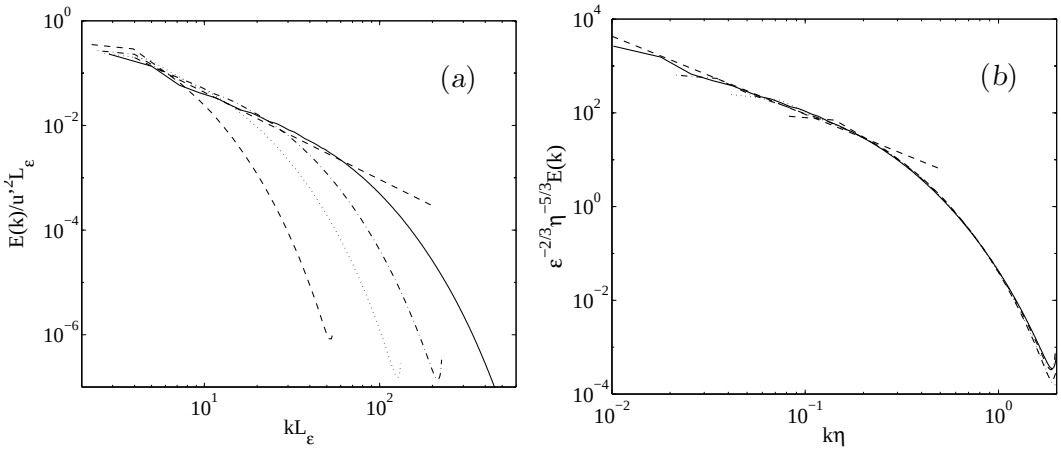

Figure 5.3: Three-dimensional spectra from a series of numerical simulations of approximately isotropic turbulence. Each simulation was forced at large scales and allowed to reach statistical equilibrium. $Re_\lambda = 40 - 180$, with longer spectra corresponding to higher Reynolds number. The straight dashed line is in both cases equation (5.3), with $C_K = 2$. (*a*) Large-scale normalization. (*b*) Kolmogorov normalization. Note that the large-scale ends of the spectra 'peel-off' at different locations in this representation. The 'hook' at the high-wavenumber end of the spectra is an artifact of the limited numerical resolution. Simulations from Jiménez & Wray (1998).

Consider for example the case in which the flow is created at $t = 0$ with approximately isotropic turbulent structures of size $L(0) = 2\pi/\kappa_0(0)$, and then left to decay. All that we initially know is that the spectral distribution of turbulent energy is approximately isotropic, and that the three-dimensional spectrum peaks near the shell $\kappa = \kappa_0$. As the decay progresses, the energy spreads through wavenumber space. The part of the energy moving towards higher wavenumbers (smaller scales) contributes to the regular Kolmogorov cascade and eventually feeds viscous dissipation. The energy diffusing towards lower wavenumbers (larger scales) cannot dissipate, because those eddies have high Reynolds numbers and are not affected by viscosity. The result is that the distribution of energy inside the spectral sphere bounded by $\kappa = \kappa_0$ tends to become uniform. After that happens, the decay consists of a slow draining, towards the high wavenumber dissipation mechanism, of the energy contained in that uniform low-wavenumber 'pool'.

The three-dimensional energy spectrum of the uniform low-wavenumber region is proportional to

$$E(\kappa) \sim \kappa^2, \tag{5.17}$$

because the three-dimensional spectrum measures the energy contained in all the Fourier modes within a spherical shell of radius κ, whose area is $4\pi\kappa^2$.

Because the large scales contain most of the energy, and because they are the ones with the slowest time scales, they control the rate at which the system evolves. As this problem shows, the decay law for the total energy in isotropic turbulence is determined solely by the form of its large-scale spectrum.

Consider the decay of isotropic turbulence. Assume that the initial three-dimensional energy spectrum is

$$E(k) = \begin{cases} A\kappa^\alpha & \text{if} \quad \kappa < \kappa_0, \\ C_K \varepsilon^{2/3} \kappa^{-5/3} & \text{if} \quad \kappa \geq \kappa_0. \end{cases} \tag{5.18}$$

As we saw above, the value to be expected for the exponent below $\kappa = \kappa_0$ is $\alpha = 2$, while the form used for $\kappa > \kappa_0$ assumes that the standard Kolmogorov cascade (5.3) has already been established. These forms are maintained during the decay, but the parameters κ_0 and ε are functions of time. It can be assumed that A is a constant, because the characteristic time scales of the large scales are much longer than those of the scales which are decaying, and the cascade has no time to change them.

Show that the turbulent kinetic energy per unit mass decays as

$$\frac{3}{2}u'^2 = k = \int_0^\infty E(\kappa)\,\mathrm{d}\kappa \sim t^{-\gamma}, \tag{5.19}$$

where the temporal exponent,

$$\gamma = 2\frac{\alpha+1}{\alpha+3}, \tag{5.20}$$

depends only on the large-scale spectrum. Determine also the decay law for the integral scale of the flow.

Solution: Continuity of the spectrum at $\kappa = \kappa_0$ links the three parameters of (5.18),

$$A\kappa_0^\alpha = C_K\varepsilon^{2/3}\kappa_0^{-5/3}, \quad \Rightarrow \quad \varepsilon = (A/C_K)^{3/2}\kappa_0^{(5+3\alpha)/2}. \tag{5.21}$$

The total kinetic energy per unit mass is found by integrating the spectrum,

$$k = A\int_0^{\kappa_0}\kappa^\alpha\,\mathrm{d}\kappa + C_K\varepsilon^{2/3}\int_{\kappa_0}^\infty \kappa_0^{-5/3}\,\mathrm{d}\kappa = \frac{3\alpha+5}{2(\alpha+1)}A\kappa_0^{\alpha+1}, \tag{5.22}$$

and its evolution equation is

$$\frac{\mathrm{d}k}{\mathrm{d}t} = -\varepsilon, \quad \Rightarrow \quad \frac{3\alpha+5}{2}\,\kappa_0^\alpha\frac{\mathrm{d}\kappa_0}{\mathrm{d}t} = -A^{3/2}\kappa^{(3\alpha+5)/2}, \tag{5.23}$$

which can be integrated to give

$$\kappa_0 \sim t^{-2/(\alpha+3)}, \quad \text{and} \quad k \sim t^{-2(\alpha+1)/(\alpha+3)}. \tag{5.24}$$

Suitable integration constants related to the initial time and energy spectrum have to be trivially included in these formulas. For the case $\alpha = 2$, the decay exponent is $\gamma \approx 1.4$.

The wavenumber of the peak of the spectrum is essentially the inverse of the integral length, as already noted when discussing spectra in general. In the present case it follows from (5.21) and (5.22) that

$$L_\varepsilon = \frac{u'^3}{\varepsilon} = \left[\frac{C_K(3\alpha+5)}{3(\alpha+1)}\right]^{3/2}\kappa_0^{-1} \sim t^{2/(\alpha+3)}. \tag{5.25}$$

The assumption that A remains constant during the decay is only an approximation, but it was shown by Saffman (1967) that it holds strictly in the limiting case in which (5.17) extends all the way to $\kappa = 0$, essentially because the largest scales contain most of the linear momentum in the flow, and boundary pressure forces, which are the only ones which could change it, become negligible as the surface-to-volume ratio vanishes in the very-large scale limit.

Problem 5.3: The dispersion of particles in turbulent flows. The knowledge of the scaling laws for the velocity fluctuations can be used to derive useful results on other important problems. Consider for example the way that two fluid particles separate from one another in a turbulent flow, which has obvious applications in the dispersion of contaminants. Assume either that the Reynolds number is infinite, so that the Kolmogorov scale η vanishes, or that the separations involved are in the inertial range of scales. Estimate how the mean distance between the two particle grows with time.

Solution: Write the equations of motion for both particles,

$$\mathrm{d}_t\boldsymbol{x} = \boldsymbol{u}(\boldsymbol{x}), \quad \text{and} \quad \mathrm{d}_t\boldsymbol{x}' = \boldsymbol{u}(\boldsymbol{x}'), \tag{5.26}$$

and subtract one from the other to get an equation for the separation $\boldsymbol{\delta} = \boldsymbol{x} - \boldsymbol{x}'$,

$$\mathrm{d}_t \boldsymbol{\delta} = \Delta \boldsymbol{u} \equiv \boldsymbol{u}(\boldsymbol{x}) - \boldsymbol{u}(\boldsymbol{x}'). \tag{5.27}$$

We discussed a similar problem in chapter 2, and argued that the velocity difference in the right-hand side of (5.27) could be approximated by $\nabla \boldsymbol{u} \cdot \boldsymbol{\delta}$, leading to an exponential growth of the separation.

The same cannot be done here, because turbulent velocity fields are not differentiable at inertial scales, and gradients cannot be taken. Instead of linearizing the velocity difference we have to use (5.1), which gives $|\Delta \boldsymbol{u}| \sim |\varepsilon \boldsymbol{\delta}|^{1/3}$. The result, after multiplying (5.27) by $\boldsymbol{\delta}$ and taking averages, is an equation of the type

$$\mathrm{d}_t |\boldsymbol{\delta}|^2 \sim \varepsilon^{1/3} |\boldsymbol{\delta}|^{4/3}, \tag{5.28}$$

whose solution is

$$|\boldsymbol{\delta}|^2 \sim \varepsilon t^3. \tag{5.29}$$

This diffusion law was first observed by Richardson (1926) in the atmosphere, and implies that a small parcel of contaminants spreads algebraically with time. It is the starting point for the theory of the turbulent diffusion of scalars, such as chemicals or heat. An interesting observation is that $|\boldsymbol{\delta}| = 0$ when $t = 0$. In differentiable fields, two trajectories only cross at singular points, so that, if $|\boldsymbol{\delta}|(0) = 0$, it remains zero at all times. What this result shows is that, at least in this approximation, all the points in a turbulent flow at infinite Reynolds number are singular, and that each of them is the origin for an infinite number of different particle trajectories, which become uncorrelated from each other after a short time.

Note that a rigorous derivation of (5.29) would involve a more complete discussion of the averaging operations implied, which would in principle also give us the numerical factor in its right-hand side. However, as it is usually the case in dealing with self-similar regimes in which there is no characteristic length, (5.29) can be derived directly from dimensional analysis. If the only parameter characterizing the flow in the self-similar range of scales is the dissipation ε, the only possible combination resulting in a length as a function of time is (5.29).

5.2 Inhomogeneity and anisotropy

Few turbulent flows are strictly isotropic or homogeneous, and we will see in the next chapter that most technologically important flows are neither. It is in fact difficult to create a statistically-steady turbulent flow that is close to isotropy, and most experimental approximations to isotropic turbulence are decaying, rather than equilibrium flows. Inhomogeneous flows are easier to maintain. We will see now that they draw energy directly from the inhomogeneity of the mean velocity, in what is essentially the first step of the energy cascade. We will concern ourselves first with their kinematic description.

In isotropic turbulence all the components of the spectral tensor can be expressed in terms of the three-dimensional spectrum $E(\kappa)$, and the cospectra vanish identically. In all other cases the cospectra can be used to measure anisotropy.

The cross products $\langle u_i u_j \rangle$ that appear in the normalization (4.23) of the cospectra were introduced by Reynolds (1894), and play an important role in turbulence theory. Consider a turbulent velocity field, and separate at each point the mean value and the fluctuation,

$$u_j(\boldsymbol{x},\, t) = U_j(\boldsymbol{x}) + \widetilde{u}_j(\boldsymbol{x},\, t), \tag{5.30}$$

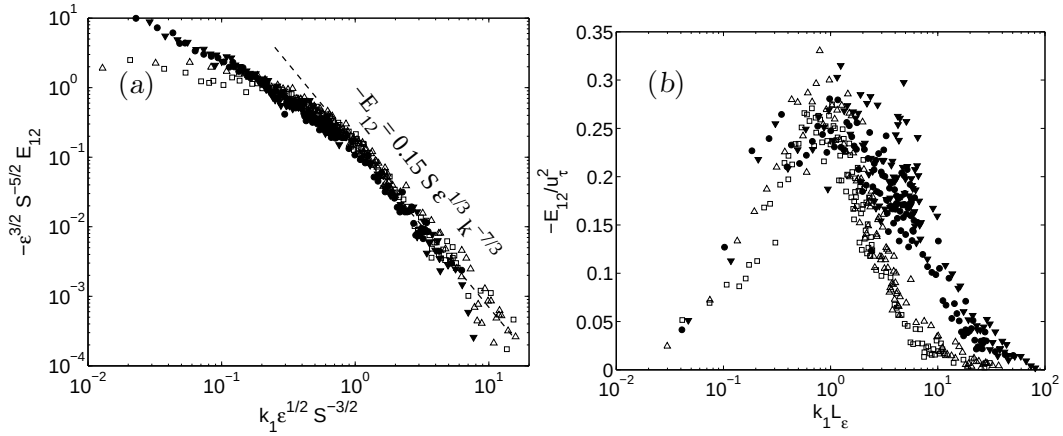

Figure 5.4: One-dimensional cospectra of $\langle u_1 u_2 \rangle$, for various shear flows at different Reynolds numbers. (*a*) In logarithmic coordinates to display the power law (5.34); (*b*) in premultiplied form normalized with the integral scale.

so that $\langle \widetilde{u}_j \rangle = 0$. We can average the Navier-Stokes equations to obtain the evolution of the mean velocities,

$$\partial_t U_i + \partial_j U_i U_j + \frac{1}{\rho}\, \partial_i P = \partial_j \left[\nu \partial_j U_i - \langle \widetilde{u}_i \widetilde{u}_j \rangle \right], \tag{5.31}$$

$$\partial_j U_j = 0. \tag{5.32}$$

In the first of these equations the unknown symmetric tensor

$$\tau_{ij} = -\langle \widetilde{u}_i \widetilde{u}_j \rangle, \tag{5.33}$$

plays a role comparable to the viscous stresses, although it actually represents a momentum flux due to the turbulent fluctuations. Estimating these 'Reynolds' stresses is the main problem in the practical computation of turbulent flows.

The cospectra (4.22) describe how the Reynolds stresses are distributed among the different length scales, and their general form can be estimated using dimensional arguments similar to those used for the energy spectrum. Consider, for example, the anisotropy induced by a simple shear $S = \partial U_1 / \partial x_2$. From symmetry considerations, all the off-diagonal Reynolds stresses vanish except for $\tau_{12} = \tau_{21}$. The latter also vanishes for $S = 0$, and changes sign with S. If the shear is not too strong we can therefore assume that the cospectrum E_{12} is linear in S and, in the self-similar inertial range, we can also assume that the only other relevant parameters are κ and ε. The only possible combination is, on dimensional grounds (Lumley, 1967),

$$E_{12}(\kappa_1) = -C_0 S \varepsilon^{1/3} \kappa_1^{-7/3}. \tag{5.34}$$

This behaviour in checked in figure 5.4(*a*) against experiments. The experimental value of C_0 is about 0.15.

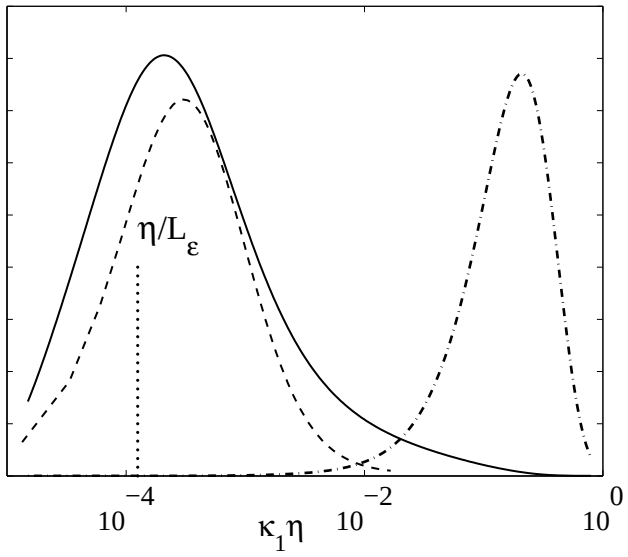

Figure 5.5: One-dimensional pre-multiplied spectra of: —— , energy spectrum, $\kappa_1 E_{11}(\kappa_1)$. ---- , dissipation spectrum, $\kappa_1 G_{11}(\kappa_1)$; —·— , Reynolds-stress cospectrum, $-\kappa_1 E_{12}(\kappa_1)$. Arbitrary units. The flow is a boundary layer from Saddoughi & Veeravali (1994). The vertical dotted line marks the location of the integral scale.

The negative exponent in (5.34) implies that the Reynolds shear stresses are large-scale quantities. Their cospectrum decays at high wavenumbers faster than the energy spectrum (5.2), and we can estimate when the former becomes negligible with respect to the latter by comparing (5.34) with (5.2). They become of the same order at the 'Corrsin' wavenumber,

$$\kappa_c \equiv \ell_c^{-1} = (S^3/\varepsilon)^{1/2}. \tag{5.35}$$

For scales $\ell \ll \ell_c$ smaller than the Corrsin limit, $E_{12} \ll E_{11}$, and the eddies can be considered isotropic, completing the justification for our implicit assumption that the inertial energy cascade is isotropic.

Intuitively what we need for eddies to be approximately isotropic is that the inertial turnover time of the eddy, $\ell/u_\ell = u_\ell^2/\varepsilon$, is short with respect to the characteristic time of deformation imposed by the shear, S^{-1}, so that the eddy can be assumed to be only slightly deformed by the shear during one rotation. This condition can be written in terms of a dimensionless shear parameter $\widehat{S}(\ell) = S u_\ell^2/\varepsilon$, which should be small. It is easy to check that $\widehat{S} \approx (\ell/\ell_c)^{2/3}$, so that the Corrsin length marks the limit between the large anisotropic scales dominated by the Reynolds stresses, and the smaller isotropic universal cascade.

We will see later that turbulence in shear flows is fed by the interaction between the Reynolds stresses and the mean shear, and that this implies that the Corrsin scale is of the order of the integral scale L_ε.

This allows us to complete the classification of the turbulent eddies according to their scales, at least for shear-driven flows (see figure 5.5). Energy and Reynolds

stresses reside at scales of the order of L_ε, which is where energy is fed into the flow. At scales somewhat smaller than L_ε the eddies become essentially isotropic, and the energy cascades into the still smaller scales without any further input from the shear. The energy contained in these small scales decreases with increasing wavenumber but, if the Reynolds number is large enough, no dissipation still occurs. It is only when $\ell \approx \eta$ that viscosity becomes important and energy is dissipated. The intermediate range of scales, in which neither energy or dissipation are important, but through which energy cascades at a constant rate ε, is the inertial range. The separation between the energy and the dissipation peaks increases as $Re_L^{3/4}$, and it is only when the Reynolds number is large enough that the two peaks become independent from each other, and the asymptotic theory presented up to now applies. This happens when $Re_\lambda \gtrsim 2000$ ($Re_L \gtrsim 2 \times 10^5$). Fully developed turbulent flow is essentially a phenomenon that only exists in the limit $Re \gg 1$.

5.2.1 *The eddy-viscosity approximation*

The assumption used in (5.34) that the cospectrum is proportional to the mean shear seems to imply, by integration, that the Reynolds stresses should also be proportional to S. This is not strictly correct, because the linearity assumption is only valid for the small eddies below the Corrsin scale on whom the effect of the shear is small. The Reynolds stresses are, on the other hand, dominated by the large scales with $\ell > \ell_c$, where the hypothesis of proportionality is less well founded. Nevertheless this linear approximation was one of the first to be tried in computing turbulent flows, and is still the basis of most of the engineering computational methods. It is expressed in tensor form as

$$\tau_{ij} - \frac{1}{3}(\tau_{ii})\,\delta_{ij} = 2\nu_\varepsilon S_{ij}, \quad \text{where} \quad S_{ij} = \frac{1}{2}(\partial_i U_j + \partial_j U_i), \tag{5.36}$$

which preserves both the symmetry of the stress tensor and the incompressibility of the velocity. The *eddy viscosity* ν_ε is in general unknown, and it is not in general constant throughout the flow. It is usually written, on dimensional grounds, either in terms of a velocity and length scales, as in $\nu_\varepsilon \sim u' L_\varepsilon$, or of a velocity and a time scale.

We will see in the rest of the course some ways of estimating the eddy viscosity. Here it is enough to remark that, even if its magnitude could be adjusted in an optimum way, the assumption (5.36) is still very strong, implying both the linear dependence of two tensors, and that they are coaxial. None of those assumptions are justified, and there are many examples in which they do not work, even to the point that the Reynolds stresses and the turbulent diffusion fluxes move 'countergradient', implying negative eddy viscosities. But there are also many examples in which the results are good, including some in which the shear parameter $\widehat{(S)}$ is of order unity. Eddy viscosity, at least in situations close to equilibrium, is probably the first approximation that should be used in estimating the behaviour of a turbulent anisotropic flow.

5.2.2 *The energy equation*

We have mentioned that in many cases turbulence is driven by the shear of the mean flow. We will now consider the details of how this happens, and in the process learn how to estimate the eddy viscosity introduced in (5.36).

Consider the Reynolds decomposition (5.30). By separating the energy equation for the complete flow into mean and fluctuating components, we can write an evolution equation for the kinetic energy of the turbulent fluctuations, $k = \langle \widetilde{u}_j^2 \rangle / 2$,

$$(\partial_t + U_j \partial_j) k + \partial_j \phi_j = \Pi - \varepsilon. \tag{5.37}$$

Note that the average $\langle\rangle$ used here can only in general be an ensemble average, taken at a given point and time over many statistically equivalent experiments. In inhomogeneous and unsteady flows no other average makes sense. However, as explained in chapter 4, it is possible in many occasions to use quantities averaged over some homogeneous directions, in which case the corresponding derivatives can be removed from the energy equation. With this precautions in mind, the left-hand side of (5.37) contains the total derivative of the energy and the divergence of an energy flux which is due to the velocity fluctuations and to the viscous diffusion, and which can be expressed as

$$\phi_j = \left\langle \widetilde{u}_j (\widetilde{p}/\rho + \widetilde{u}_i^2/2) \right\rangle - \nu \partial_j k. \tag{5.38}$$

In the right hand side we find the energy dissipation, as in isotropic turbulence,

$$\varepsilon = \nu \left\langle |\nabla \boldsymbol{u}|^2 \right\rangle, \tag{5.39}$$

and a new term which feeds energy into the fluctuations, and which is the work of the mean flow against the Reynolds stresses,

$$\Pi = \tau_{ij} \partial_j U_i. \tag{5.40}$$

It is this production term that is responsible for maintaining inhomogeneous turbulence. Since we have seen above that the Reynolds stresses are large-scale quantities, turbulent energy is fed directly into the large scales, and cascades towards dissipation through the usual Kolmogorov process. If the flow is not too far from isotropy or from equilibrium, production and dissipation are the dominant processes and most scales in the system can still be approximately described by the isotropic mechanisms. Most of the spectra used in figure 4.3, with their excellent collapse at small scales, were obtained from inhomogeneous shear flows.

We may note at this stage that, even if turbulent flows dissipate energy more efficiently than laminar ones, turbulent dissipation is still a comparatively weak phenomenon. The basic inertial relation (5.1) can be recast as a relation between the kinetic energy of the transverse velocity fluctuations and a local time scale,

$$\frac{u_{\ell,1}^2}{\varepsilon} \approx 1.4^3 \, \frac{\ell}{u_{\ell,1}}, \tag{5.41}$$

where $u^2_{\ell,j} = \langle [u_j(x_1+\ell) - u_j(x_1)]^2 \rangle$ is the second-order structure function of the j-th velocity component with respect to a displacement ℓ in the x_1 direction. This can be put in a more useful form using isotropy considerations similar to those given in appendix B,

$$\frac{k_\ell}{\varepsilon} \approx 10\,\frac{\ell}{u_{\ell,2}}, \quad \text{where} \quad k_\ell = \frac{1}{2}(u^2_{\ell,1} + u^2_{\ell,2} + u^2_{\ell,3}) = \frac{5}{4}u^2_{\ell,2} \tag{5.42}$$

is an estimate on the kinetic energy of the flow at size ℓ. The left-hand side of this equation is the time that it would take for the dissipation to damp an eddy, which is proportional, in its right-hand side, to the eddy turnover time. This proportionality agrees with our assumptions about the inertial range, but the coefficient is large, and the result is that an eddy can be sheared by a relatively large amount, $10\,\ell$, before the subgrid dissipation has time to damp it.

Energy considerations such as these can be used to derive a rough estimate for the eddy viscosity coefficient introduced in §5.2. If we use the energy production (5.40) as a surrogate for the dissipation ε, we can express it in terms of the eddy viscosity as

$$\varepsilon \approx \Pi = \tau_{ij} S_{ij} = 2\nu_\varepsilon S_{ij} S_{ij}. \tag{5.43}$$

If we then estimate the rate of strain as $S = u_{\ell,2}/\ell$, the relation (5.42) becomes

$$\nu_\varepsilon(\ell) \approx 0.125\,\ell\,u_{\ell,2}. \tag{5.44}$$

which can be written as

$$\frac{\ell\,u_{\ell,2}}{\nu_\varepsilon(\ell)} \approx \frac{u^3_{\ell,2}}{\varepsilon\ell} \approx 8. \tag{5.45}$$

This implies that the 'effective' Reynolds numbers of *any* turbulent eddy, based on the eddy viscosity due to still smaller scales, is constant. This argument, which is just a different way of expressing the self-similarity of the inviscid cascade, is the basis for a rule of thumb sometimes used in rough engineering estimates, which is that the effective Reynolds number of any turbulent flow, based on its eddy viscosity, is $\Delta U L/\nu_\varepsilon \approx 10 - 50$. The present derivation shows that the rule is a lowest-order approximation, still coarser and even less justified than the eddy viscosity assumption, but nevertheless useful for preliminary evaluations.

Note that the viscosity estimated above is a function of the scale at which it is measured. This is to be expected, because the eddy viscosity was introduced to represent the effect of the unknown velocity fluctuations on the mean flow and, if we had chosen to consider as known all the turbulent motions larger than a given size, the effect of the remaining 'sub-grid' fluctuations would have been different depending of how many of them had been neglected. The most common application of the eddy viscosity is however as a representation of *all* the turbulent fluctuations, which is how the Reynolds decomposition was defined in §5.2. In that case the above arguments are still approximately valid, and (5.44) gives us the two basic ways of estimating the eddy viscosity. If we consider a flow with a velocity fluctuation intensity u', and with an integral scale L_ε,

$$\nu_\varepsilon \sim u' L_\varepsilon, \quad \text{or} \quad \nu_\varepsilon \sim u'^2 \frac{L_\varepsilon}{u'}. \tag{5.46}$$

Both estimates are of course identical, and should be supplemented with empirical proportionality coefficients. They represent two ways of expressing the same idea, and we will see later that engineering methods use one or the other depending on the basic variables that they choose to model. In the first case the eddy viscosity is estimated as the product of a velocity and of a length scale, which is reminiscent of the expression derived in comment 1.2 in the introduction for the viscosity of a gas. The second expression in (5.46) uses the same idea to express ν_ε as the product of an energy and of a time scale, which is how we have derived it in this section.

We can now come back to the question, deferred after (5.35), of how to estimate the Corrsin scale. Assume a shear flow with velocity fluctuations of order u'. Since the Reynolds stresses are averages of products of the velocity components, we can assume that $\tau = O(u'^2)$, so that the energy production rate is $\Pi = O(Su'^2)$. If the flow is approximately in energy equilibrium, the production and the dissipation are of the same order, and

$$\ell_c = (\varepsilon/S^3)^{1/2} \approx u'^3/\varepsilon = L_\varepsilon. \tag{5.47}$$

This scaling is checked in the premultiplied spectra in figure 5.4(b) in which the abscissae, even if referring to the Reynolds stresses, are normalized with L_ε.

It is important to realize that ν_ε is much larger than the molecular viscosity. It follows from (5.46) that the ratio between the two is the (molecular) Reynolds number, and that the molecular viscosity is always negligible. This is the main property of turbulence from the applications point of view, and extends to the diffusion of scalar contaminants. One example might help to bring it into focus. The time L^2/κ that the molecular diffusivity κ needs to mix a drop of milk into a cup of coffee is about one day, while we are all familiar with how much faster is mixing with even moderate levels of stirring.

Chapter 6

Turbulence in Shear Flows

Summary

Most of our discussion up to now has been centred on isotropic or at least on homogeneous flows, on the grounds that they describe the universal behaviour of the small scales. In practice few flows are either homogeneous or isotropic, and the rest of these lectures will be devoted to the study of shear-driven turbulence. Since we have seen that only the largest turbulent scales are affected by the driving mechanism, our discussion from now on will be devoted to them.

This chapter is a phenomenological description of archetypical shear flows, both away and near walls. The simplest ones are those away from walls, including shear layers, jets and wakes behind bodies. They are described in §6.1. Wall-bounded flows, described in §6.2, are perhaps even more interesting, not only because they include such technologically important examples as pipes and boundary layers around moving bodies, but because there are still some questions about them which are not completely understood. They are therefore a fertile source of research problems. These two sections are the application to the real world of the theory that has been developed up to now. Each of them consists of two parts: an elementary description of the flows, and of where they are found in science and in technology, and a more advanced subsection describing their structure and some of their applications. The discussion of free shear flows also includes a short introduction to hydrodynamic stability theory.

6.1 Free-shear flows

We saw in the introduction that it was in shear flows that turbulence was first recognized. Those flows have continued to be the subject of technological attention because they are closer to problems of practical interest than isotropic turbulence, and a lot is known about their behaviour. Much of that information is found in engineering collections of experimental data, some of which, such as AGARD (1998), were designed with physics as well as with engineering in mind.

The defining characteristic of these flows is the presence of a mean velocity

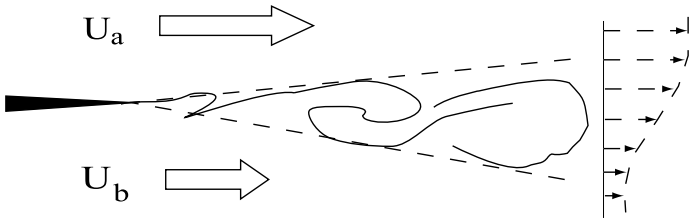

Figure 6.1: Sketch of a plane shear layer.

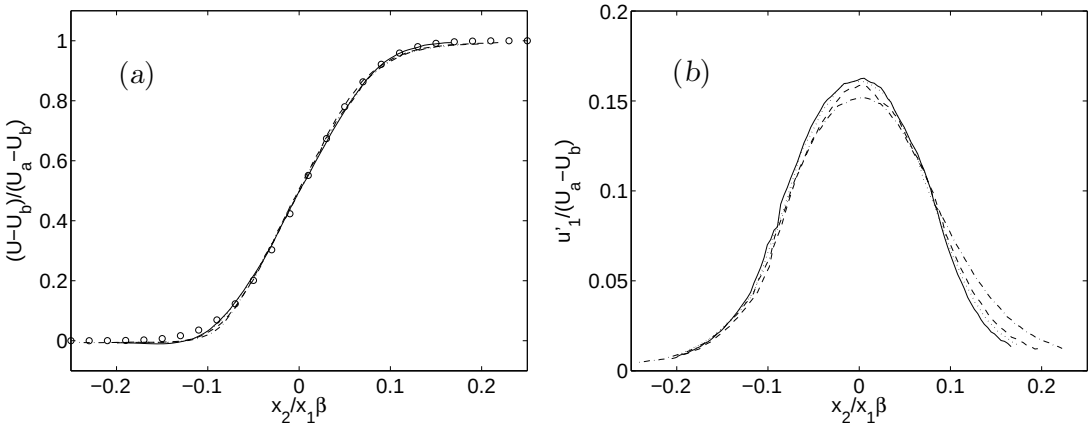

Figure 6.2: Plane shear layer. (a) Mean streamwise velocity, (b) Root mean square streamwise velocity. $\beta = 0.3$, $(U_a - U_b)\theta_0/\nu = 2900$, where θ_0 is the initial momentum thickness. —·— , $\beta x_1/\theta_0 = 40$; - - - - , 60; ····· , 90; —— , 135, from Delville, Bellin & Bonnet (1988); ∘ in (a) is the constant eddy viscosity approximation.

gradient, which makes the large scales anisotropic and, as we saw in §5.2.2, provides a continuous source of turbulent kinetic energy.

The plane shear (or mixing) layer is the classical example of a turbulent shear flow away from walls. Two parallel streams of different velocities are separated by a thin plate and come together as the plate ends. The layer grows from the resulting velocity discontinuity and thickens downstream (figure 6.1). Shear layers appear in the initial regions of many other flows, such as jets and separation regions. They are technologically important because they generate noise and dissipate energy, and are therefore a source of drag, but also because, if the two streams contain different fluids, it is in the shear layer that the mixing occurs. Most industrial combustors, and a lot of the mixers in chemical industry, are designed around shear layers. It is probably because of this that the shear layer was one of the first turbulent flows to be understood in detail, and also one of the first to be controlled.

A lot can be said about the mixing layer from dimensional considerations. An ideal layer grows from a discontinuity of zero thickness and, in the absence of viscosity, has no length scale except for the distance to the origin. The only other parameters are the velocities of the two free streams, $U_a > U_b$. The mean velocity,

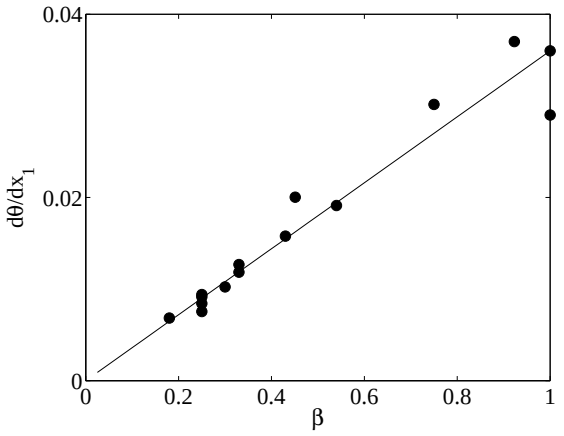

Figure 6.3: Growth rate of experimental shear layers, from various sources. The solid line is $\mathrm{d}\theta/\mathrm{d}x_1 = 0.036$.

or the r.m.s. fluctuations, must therefore take the form

$$\frac{U(x_2)}{U_a - U_b}, \frac{u'}{U_a - U_b}, \ldots = f(x_2/x_1, \beta) \tag{6.1}$$

where $\beta = (U_a - U_b)/(U_a + U_b)$ is a parameter characterizing the velocity ratio, and x_1 and x_2 are the streamwise and transverse coordinates. The similarity laws (6.1) are tested against experiments in figure 6.2 at several distances downstream for the splitter plate, and both work well. In real flows the thickness of the boundary layers on both sides of the splitter plate provides a length scale for the initial development of the mixing region. A useful definition is the momentum thickness,

$$\theta = \int_{-\infty}^{\infty} \frac{(U - U_b)(U_a - U)}{(U_a - U_b)^2} \, \mathrm{d}x_2, \tag{6.2}$$

which is related to the momentum deficit with respect to a sharp discontinuity. The self-similar behaviour (6.1) is typically achieved in shear layers at distances from the plate of the order of several hundred times the initial momentum thickness, although the precise value depends on the Reynolds number and on the details of the initial boundary layers. The origin of coordinates in (6.1) should for this reason be taken at some distance from the end of the splitter plate, to account for the initial development of the layer.

It should be clear from the small values of x_2/x_1 in figure 6.2 that the layer spreads slowly. This is a common property of shear flows which could have been anticipated from the observation in §5.2.2 that turbulent dissipation is a weak process. The turbulent region cannot spread without dissipating energy, and the result is that the flow is slender, much longer than it is wide. This allows it to be approximated as quasi-parallel. For shear layers, for example, we can think of the flow as spreading laterally while being advected downstream with a mean velocity $U_c = (U_b + U_a)/2$. The downstream coordinate is thus converted to an evolution

time $t = x_1/U_c$ and, in that moving frame of reference, the only velocity scale is the difference $\Delta U = U_a - U_b$. The lateral spreading rate must then be proportional to

$$\frac{\mathrm{d}\theta}{\mathrm{d}x_1} \approx \frac{1}{U_c}\frac{\mathrm{d}\theta}{\mathrm{d}t} = C_L \frac{U_a - U_b}{U_a + U_b} \tag{6.3}$$

This analysis is only approximate, as shown in detail in problem 6.1, but the prediction that the spreading rate should be proportional to the parameter β is well satisfied, with $C_L \approx 0.035 - 0.045$ (see figure 6.3).

The shape of the profile is also well represented by a crude eddy-viscosity approximation. Assume an eddy viscosity which is constant across the layer and that, on dimensional grounds, has the form

$$\nu_\varepsilon = C' \Delta U \theta \tag{6.4}$$

Neglecting longitudinal gradients and transforming the problem to a temporal one in the advective frame of reference, the mean velocity satisfies a diffusion equation whose solution is an error function [PROBLEM 6.1]. It agrees quantitatively with the measured velocity profiles if $C' \approx 0.063$ (figure 6.2.a). The 'Reynolds number' of the turbulent shear layer, based on its momentum thickness, on the velocity difference, and on that eddy viscosity, is about 15, which is of the same order as the effective turbulent Reynolds numbers predicted in §5.2.2. Note that this is independent of the actual molecular Reynolds number, underscoring again that molecular viscosity is negligible for the large scales of turbulent flows, and therefore for the Reynolds stresses and for the velocity profiles.

Problem 6.1: Write the approximate equation for a slowly growing free shear layer. Justify the limit in which the mean advection approximation holds, integrate the resulting equation, using the uniform eddy viscosity model (6.4), and relate its proportionality constant C' to the experimental growth rate C_L of the momentum thickness.

Solution: The slow-growth approximation means that streamwise dimensions are much longer than transverse ones, so that streamwise derivatives of similar quantities can be neglected with respect to transverse ones. Such simplifications are often the key to solving problems in fluid mechanics, which are otherwise too complex to allow simple solutions, and it is important to gain some familiarity with them.

Assume that the ratio of x_2 to x_1 is of the order of a small quantity $\epsilon \ll 1$. The continuity equation for the longitudinal and transverse mean velocities, U and V, is

$$\partial_1 U + \partial_2 V = 0, \tag{6.5}$$

which, since $\partial_1 = O(\epsilon\partial_2)$, implies that $V = O(\epsilon U)$. Choose units such that ∂_2 is $O(1/\epsilon)$ and V is $O(\epsilon)$, while U and and ∂_1 are $O(1)$. This implies that $x_2 = O(\epsilon)$ and $x_1 = O(1)$. The two mean momentum equations are

$$U\partial_1 U + V\partial_2 U + \partial_1 p = \partial_1(\nu_\varepsilon \partial_1 U) + \partial_2(\nu_\varepsilon \partial_2 U), \tag{6.6}$$

and

$$U\partial_1 V + V\partial_2 V + \partial_2 p = \partial_1(\nu_\varepsilon \partial_1 V) + \partial_2(\nu_\varepsilon \partial_2 V). \tag{6.7}$$

In both equations the longitudinal derivatives in the right-hand sides are $O(\epsilon^2)$ with respect to the transverse ones, and can be neglected. In the transverse momentum equation (6.7) the first two terms are $O(\epsilon)$, and the equation reduces to $p = O(\nu_\varepsilon)$. When this is substituted in (6.6),

the pressure gradient is seen to be of order $\partial_1 p = O(\nu_\varepsilon)$, and can be neglected when compared with the Reynolds stresses in the right-hand side, which is $O(\nu_\varepsilon/\epsilon^2)$. The simplified momentum equation is then

$$U\partial_1 U + V\partial_2 U = \partial_2(\nu_\varepsilon \partial_2 U), \tag{6.8}$$

in which all the terms in the left-hand side are $O(1)$, while the one in the right-hand side is $O(\nu_\varepsilon/\epsilon^2)$. This shows that the condition for the spreading rate to be slow is that the eddy viscosity also has to be small, $\nu_\varepsilon = O(\epsilon^2)$, and anticipates that the proportionality constant C' in (6.4) will be found to be $O(\epsilon)$.

Equation (6.8) has to be solved together with the continuity equation (6.5), and the two constitutive equations (6.3) and (6.4). We can now remove most of the parameters by defining new variables

$$U = U_c + \Delta U u, \qquad x_2 = \epsilon x_2', \qquad V = \epsilon \Delta U v, \tag{6.9}$$

where $\epsilon = (2C_L C')^{1/2}\beta$. This change of variables implements the scalings discusses above, and leaves the continuity equation invariant. The momentum equation becomes

$$\partial_1 u + 2\beta(u\partial_1 u + v\partial_2' u) = \partial_2'(x_1 \partial_2' u), \tag{6.10}$$

where $\partial_2' = \partial/\partial x_2'$. This equation is still complicated, and only simplifies when $\beta \ll 1$. The limit in which terms of $O(\beta)$ are neglected is the mean advection approximation discussed in (6.3), since x_1 can then be treated as a time, and the shear layer thickens as the 'time' increases downstream. The final simplified equation is

$$\partial_1 u = \partial_2'(x_1 \partial_2' u). \tag{6.11}$$

The boundary conditions are that $u = \pm 1/2$ when $x_2 \to \pm\infty$, and u is initialized at $x_1 = 0$ with a velocity discontinuity in which $u = 1/2$ if $x_2 > 0$, and $u = -1/2$ otherwise. There is no length scale in this problem, as seen from the property that (6.11) is not changed by rescaling x_1 and x_2' by a common factor, and the solution can be expected to depend only on the dimensionless group $\xi = x_2'/x_1$. The equation satisfied by this *similarity* solution is found by substitution to be

$$\xi \partial_\xi u + \partial_{\xi\xi} u = 0, \tag{6.12}$$

which can be integrated directly to

$$u = \frac{1}{2}\,\mathrm{erf}(\xi/\sqrt{2}). \tag{6.13}$$

Using this solution in the definition (6.2) of the momentum thickness, and transforming back into dimensional variables, we finally obtain,

$$\theta = \int_{-\infty}^{\infty} \left(\frac{1}{4} - u^2\right) \mathrm{d}x_2 = \epsilon x_1 \int_{-\infty}^{\infty} \left(\frac{1}{4} - u^2\right) \mathrm{d}\xi \approx 0.798 (C' C_L)^{1/2} \beta x_1. \tag{6.14}$$

When this is compared with the experimental growth law (6.3), it provides a relation between the experimental results and the empirical modelling coefficient,

$$C' \approx 1.57 C_L, \tag{6.15}$$

which is the one used in the text and in figure 6.2(a). The form (6.13) is however an honest prediction which does not depend on the adjustable parameter C', and it agrees well with the experimental profiles even if the value of β (= 0.3) is not very small. Note that the full equation (6.10) also admits a similarity solution depending only of ξ, but that the dependence of its growth rate on β is not as simple as (6.3) (although the difference is in practice fairly small.)

6.1.1 *The large scales*

Given the success of this crude approximation, which essentially substitutes turbulence by a homogeneous fluid with a modified viscosity, it was a surprise to find that

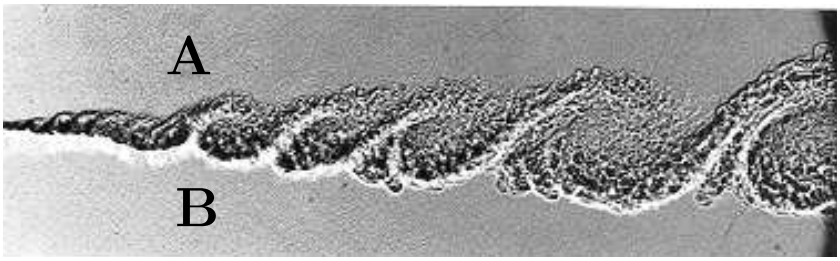

a

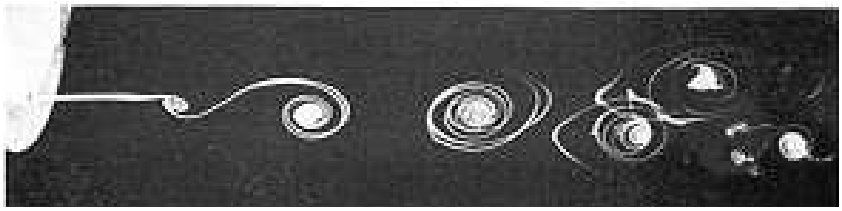

a

Figure 6.4: (*a*) Turbulent shear layer at high Reynolds number between two streams of different gases, Brown & Roshko (1974). The Reynolds number based on maximum visual thickness is $Re \approx 2 \times 10^5$ (*b*) Initial development of a low Reynolds number velocity discontinuity, Freymuth (1966). $Re \approx 7,500$

the largest scales of the plane shear layer are not homogeneous at all, and that the flow can be understood, to a large extent, in terms of linear stability theory.

The key observation was made by Brown & Roshko (1974), who found that the interface between the two streams takes the form of large, organized, quasi-two-dimensional structures, which span essentially the whole width of the layer (figure 6.4.*a*), and which are strikingly reminiscent of the linear Kelvin–Helmholtz instability waves of a two-dimensional vorticity layer (figure 6.4.*b*), already mentioned in chapter 2.

This is actually a good point in which to discuss flow instabilities, which we have repeatedly invoked in previous chapters, but never analyzed in detail. Hydrodynamic stability is similar to that of other mechanical systems. Small perturbations to stable equilibrium states remain small, and die in the presence of friction. Unstable perturbations grow until the system moves far from its original state. Instabilities are most important in the transition to turbulence of steady laminar flows, which is a subject beyond these notes, but the concept can be extended to more complicated dynamical structures, such as turbulent flows, as long as the times involved are faster than other time scales of the basic flow.

Flow instabilities are studied by linearizing the equations of motion about some mean equilibrium solution. The procedure is similar to the Reynolds decomposition introduced in §5.2, but the perturbations are assumed to be infinitesimal, and all the quadratic terms are neglected, including the Reynolds stresses. Even so an energy equation similar to (5.37) can be obtained by contracting the linearized momentum equation with the perturbation velocities $\widetilde{\boldsymbol{u}}$, and it contains an energy production term $\Pi = -\widetilde{u}_k \widetilde{u}_j \partial_j U_k$ which is identical to (5.40). The linearized fluctuations can extract energy from the mean flow through this term, or lose it, and as a consequence

they can grow or decay in times scales which, if Π is interpreted as a ratio between an energy and a characteristic evolution time, are of the order of the inverse of the mean velocity gradient. The only simplification that linearization brings to the energy equation is the disappearance of the cubic terms from the energy flux (5.38).

Linear processes can be important in some turbulent flows because, as we saw in §5.2.2, turbulent dissipation is weak. The velocity fluctuations in figure 6.2(b), for example, are small compared with the velocity difference between the two streams. If we assume that there are structures of the size of the shear layer thickness, θ, their internal deformation times would be of the order θ/u', while the shearing time due to the mean flow $\theta/\Delta U$ would be shorter. The shortest time controls the dynamics of the flow, and the large scales are controlled by the linear processes due to the mean flow, instead of by their nonlinear self-deformation. The internal times of the turbulent eddies decrease with their size, and any linear process that we may identify as important for the larger flow scales does not necessarily remain relevant for the smaller ones; the linear approximations considered in this section are typically restricted to structures which are larger than the Corrsin scale introduced in the previous chapter.

A serious study of stability theory is beyond the scope of these notes, but a simple example would clarify its application to free shear flows. It is enough for that purpose to consider two-dimensional inviscid situations in which the base flow

$$\boldsymbol{U} = [U(x_2),\, 0,\, 0]. \tag{6.16}$$

depends only on x_2, and the superimposed infinitesimal fluctuations $\widetilde{u}$ are only functions of x_1, x_2 and time. Slender flows, like the free shear layer, can be approximated in this way if the growth times for the fluctuations are short compared with the time needed by the base flow to change appreciably. Consider for example the quasi-parallel approximation of the shear layer leading to (6.3). We can expect the turbulent fluctuations within the layer to be at most of wavelength $O(\theta)$, while the energy argument given above suggests that they grow or decay in times which are of the order of the inverse of the mean shear $T_s = O(\theta/\Delta U)$. During that time the fluctuations are advected by the mean flow over a distance $x_1 = O(U_c T_s) = O(\theta/\beta)$, and move to regions in which the mean profile has thickened by an amount $C_L \beta x = O(C_L \theta)$. Since the empirical value for C_L was found to be small, that implies that the mean profile changes little during the characteristic evolution time of the fluctuations. Their behaviour can then be *approximately* analyzed using a steady parallel velocity profile such as the one found in problem 6.1,

$$U = \mathrm{erf}(x_2). \tag{6.17}$$

The hydrodynamic stability of such parallel flows is a well-developed field, and those interested should consult the textbooks by Drazin & Reid (1981) and by Schmid & Henningson (2001). Several of the books mentioned in the introduction devote chapters to this topic, specially those by Monin & Yaglom (1975) and by Lesieur (1997). The review article by Huerre (2000) deals with instabilities in free shear flows, and is specially relevant to the present discussion.

The linearized evolution equations can be expressed in terms of the vorticity fluctuations as,

$$(\partial_t + U\partial_1)\widetilde{\omega}_3 - U''\widetilde{u}_2 = \nu\nabla^2\widetilde{\omega}_3, \tag{6.18}$$

where U' and U'' stand for $\mathrm{d}U/\mathrm{d}x_2$ and $\mathrm{d}^2U/\mathrm{d}x_2^2$. The dependence on ω_3 can be eliminated by differentiating (6.18) with respect to x_1, and using continuity to obtain an equation which involves only u_2,

$$(\partial_t + U\partial_1)\Phi - U''\partial_1\widetilde{u}_2 = \nu\nabla^2\Phi, \quad \text{where} \quad \Phi = \partial_1\widetilde{\omega}_3 = \nabla^2\widetilde{u}_2. \tag{6.19}$$

This 'Orr-Sommerfeld' equation forms the basis for the analysis of the linear stability of parallel flows. We will only consider here the inviscid limit in which its right-hand side vanishes, in which case (6.19) is known as Rayleigh's equation.

Equation (6.19) is linear and can be solved by superposition of elementary solutions, which are harmonic along the directions in which the basic flow is homogeneous. Moreover, if the basic flow is steady, the temporal behaviour of each individual mode can be expanded in terms of exponentials. Thus in the parallel case (6.16) the perturbations can be expanded in terms of functions of the form

$$\widetilde{u} = \widehat{u}(\kappa,\, x_2)\exp[\mathrm{i}\kappa(x_1 - ct)]. \tag{6.20}$$

If we substitute (6.20) into (6.19), Rayleigh's equation reduces to the ordinary differential equation

$$(U - c)\widehat{\Phi} - U''\widehat{u}_2 = 0, \tag{6.21}$$

where

$$\widehat{\Phi} = \left(\frac{\mathrm{d}^2}{\mathrm{d}x_2^2} - \kappa^2\right)\widehat{u}_2. \tag{6.22}$$

It has to be supplemented with boundary conditions which usually require that the perturbation velocities vanish at the walls or at infinity, and only has non-vanishing solutions if a certain eigencondition,

$$c = c(\kappa), \tag{6.23}$$

is satisfied. We will only concern ourselves here with the (simplest) temporal problem, in which the wavenumber κ is real and the temporal eigenvalue, $c = c_r + \mathrm{i}c_i$, can be complex. Eigenfunctions whose eigenvalues c have positive imaginary parts grow exponentially in time, while those whose eigenvalues have negative imaginary parts decay. Any initial condition has to be expanded in terms of all the spatial wavenumbers but, after a while, only those with unstable eigenvalues grow, and the stable ones disappear. From the point of view of long-term behaviour, only the former have to be studied.

The instabilities of steady parallel flows can be classified into two groups. 'Inertial' ones are essentially independent of viscosity, and are unstable as long as the Reynolds number is above some low threshold, $Re \approx 1 - 10$. Their growth rates, κc_i, are of the same order as the shear of the base flow, and they grow in times comparable to a single turnover time of the basic flow. The instabilities of

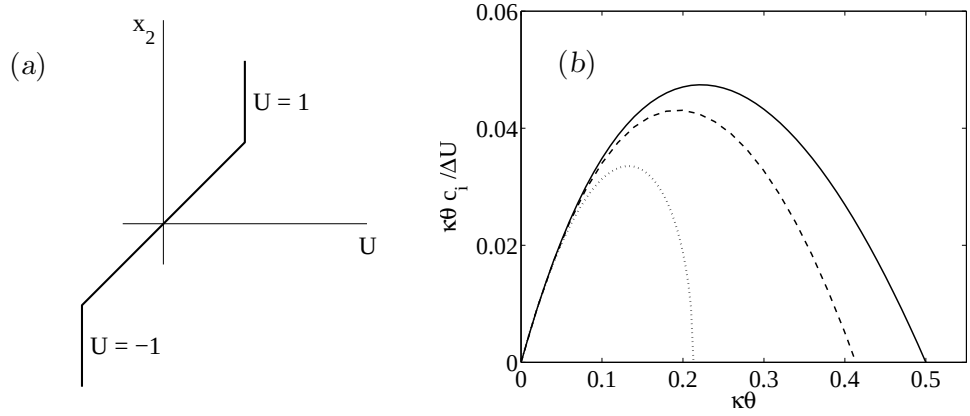

Figure 6.5: (*a*) Straight-line approximation (6.25) to the mean velocity profile (6.17). (*b*) Growth rate σ_r of the unstable waves for different models of the shear layer velocity profile. ——— , $U = \tanh(x_2)$; - - - - , $U = \mathrm{erf}(x_2)$; ····· , straight-line approximation (*a*).

the second group appear in flows which are stable to perturbations of the first type, and depend on the viscosity for their destabilization mechanism. These flows are typically stable for very low and for very high Reynolds numbers, and unstable only in some intermediate range. The growth rates of this second class of instabilities tend to be much slower than those of the inertial type, and are therefore not important in turbulence, where they have to compete with faster nonlinear processes. The defining characteristic of free shear flows is that their mean velocity profiles are inertially unstable to large-scale perturbations.

It was first shown by Rayleigh (1880) that, in the absence of rotation and of body forces, the inviscid instabilities of the first kind always arise, in parallel flows, in layers of stronger vorticity in a weaker background. This is the basic Kelvin–Helmholtz instability discussed in §2.2, in which the vorticity layer breaks down, essentially by wrinkling, in times which are of the order of its internal shear time. The following problem shows how to compute the unstable eigenvalues in the simplified model case of a layer of uniform vorticity in an irrotational background.

Problem 6.2: Instability of a uniform vortex layer. Many of the complications of Rayleigh's equation can be avoided by studying profiles such as the one in figure 6.5(*a*), which are formed by straight line segments. On each of these segments, $U'' = 0$, and equation (6.21) reduces to $\widehat{\Phi} = \mathrm{d}^2\widehat{u}_2/\mathrm{d}x_2^2 - \kappa^2\widehat{u}_2 = 0$, whose solutions are $\widehat{u}_2 \sim \exp(\pm\kappa x_2)$. At the corners the second derivative is infinite, but the normal velocity has to be continuous across the corner, and equation (6.21) can be integrated across the singularity to obtain a second jump condition which contains all the required information,

$$(U - c)\,[\mathrm{d}\widehat{u}_2/\mathrm{d}x_2]^+_- = \widehat{u}_2\,[U']^+_-. \tag{6.24}$$

Use piecewise-exponential eigenfunctions, and the jump condition (6.24) to compute the stability eigenvalues for the straight-line profile

$$U = \begin{cases} 1, & x_2 > 1 \\ x_2, & -1 \le x_2 \le 1 \\ -1, & x_2 < -1 \end{cases} . \tag{6.25}$$

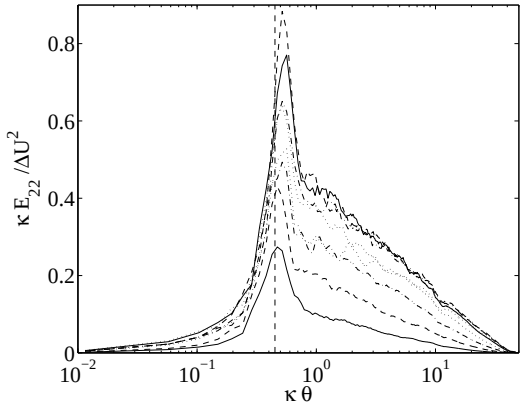

Figure 6.6: Energy spectra of the transverse velocity component in a free shear layer, plotted against the wavenumber normalized with the local momentum thickness, from Delville, Bellin & Bonnet (1988). The dashed vertical line is the limit of instability for a parallel error function velocity profile, $\kappa\theta = 0.42$. The different spectra correspond to different positions across the layer. $\beta = 0.3$. $\Delta U\theta/\nu = 1.2 \times 10^4$, $\beta x/\theta_0 = 140$.

Answer: Because of the boundary conditions, the velocities in the three regions are

$$\widehat{u}_2 = \begin{cases} \exp(-\kappa x_2), & x_2 > 1 \\ A\exp(-\kappa x_2) + B\exp(\kappa x_2), & -1 \le x_2 \le 1 \\ D\exp(\kappa x_2), & x_2 < -1 \end{cases} .$$

The jump conditions at $x_2 = 1$ are, for example,

$$\begin{aligned} \textbf{Continuity of } \widehat{u}_2\textbf{:} \qquad & 1 - A = B\mathrm{e}^{2\kappa}. \\ \textbf{(6.24):} \qquad & \kappa(1-c)\left(1 - A + B\mathrm{e}^{2\kappa}\right) = 1. \end{aligned}$$

Together with two similar conditions at $x_2 = -1$, they provide four equations for A, B, D, and c, and finally

$$c = \frac{\left[(2\kappa-1)^2 - \mathrm{e}^{-4\kappa}\right]^{1/2}}{2\kappa}.$$

The velocity profile in the previous problem is only unstable for long waves in the range $\kappa\theta \lesssim 0.21$, with a growth rate which is plotted with dotted line in figure 6.5(b). More realistic smooth profiles have a wider range of instability, $\kappa\theta \lesssim 0.45$, and are also plotted in figure 6.5(b). The result of this instability are easily seen in the spectra of natural turbulent free shear layers, as shown in figure 6.6. There are two regions in those spectra. To the left of the theoretical linear instability limit the energy grows exponentially, while to the right, where the shorter waves are linearly stable, its decays algebraically through the usual turbulent cascade. It has moreover been shown that not only the intensity and wavelengths of the structures, but also their internal organization, agree remarkably well with the two-dimensional stability results which one would expect only to apply for laminar mixing layers. The reason is that the Kelvin-Helmholtz instability is essentially inviscid, and that its development is only weakly modified by viscosity. The large structures see the

effect of the smaller ones as an eddy viscosity, which is obviously different from the molecular viscosity, but which has only a small effect on them.

6.1.2 *Mixing and control*

The presence of coherent structures has important consequences. Perhaps the most obvious is the possibility of control. It is clear that, if the large structures determine the energy dissipation rate (see section 5.1), and are therefore responsible for the growth of the layer, and if they in turn originate from the amplification of small initial perturbations, it should be possible to control the characteristics of the layer by manipulating the initial conditions. This was shown to be true in early experiments by Oster & Wygnanski (1982), and has since then been used in practical manipulations of flows which include shear layers, jets, wakes and separating flows.

The second important effect of the coherent structures is their influence on turbulent mixing which, as we noted at the beginning of this section, is one of the important applications of this particular flow. Before the discovery of the structures it was known that the mean concentration profile of two mixing streams was similar to that of the velocity, and it was believed that it reflected the molecular mixing of the two species. This turns out not to be the case in the presence of well-defined coherent structures. They move large parcels of unmixed fluid across the layer without actually mixing them, and decrease the rate of any chemical reaction between the two streams. See for example in figure 6.4 how large tongues of almost pure fluid A cross into stream B, and viceversa. True mixing only occurs once these large-scale excursions have been broken to molecular size by the cascade process.

The large scales can however be modified to some extent by the amount of three-dimensionality in the small scale structure, which controls the effective eddy viscosity. Several mixing control strategies have been based on introducing three-dimensional vorticity at the splitter plate, thus promoting secondary instabilities and preventing the coherence. This has been used, for example, to increase the level of molecular mixing and to decrease noise.

In general, and although aspects such as the influence of compressibility, of density differences, and of the three-dimensionality of the mean flow, are still subjects of active research, it can be said that free shear flows are amongst the best understood, and most easily controlled, turbulent flows.

6.2 Wall-bounded flows

In contrast to the isotropic turbulent cascade, and to free shear flows, wall-bounded turbulence is the subject of a lot of current research, and the excuse for some outstanding controversies. Those flows, which include boundary layers, pipes and channels, include some of the main open problems in turbulence, but they are very important technologically. Most of the pressure loses in pipes, rivers, and canals, as well as most of the friction drag of moving vehicles, are due to wall-bounded turbulence.

We outline here the classical theory. Consider a circular pipe of radius R,

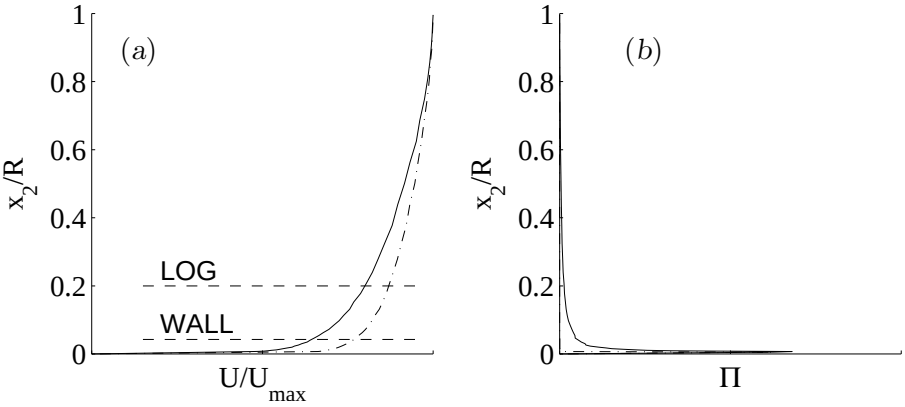

Figure 6.7: Profiles from a turbulent pipe. (a) Mean velocity. (b) Turbulent energy production. ——— , $Re_\tau \approx 2,000$; —·— , 5×10^5. Zagarola & Smits (1997). The dashed lines in (a) mark the classical upper limits for the logarithmic and wall regions; the latter for $Re_\tau \approx 2,000$.

whose mean velocity profile is shown in figure 6.7(a) as a function of the distance x_2 from the wall. It is tempting to normalize the profile with the velocity U_{max} at the centreline, which is also the maximum velocity difference across the flow, but it is clear from the figure that most of that difference is concentrated in a thin layer near the wall, and that it may not be relevant to the central part of the pipe. This is even clearer when the two Reynolds numbers in the figure are compared. They suggest that the scaling in the core of the pipe should apply to relative, rather than absolute, velocities, and that the latter are isolated from the wall by what can almost be considered a velocity discontinuity across a thin layer.

The classical velocity scaling is based on the turbulent shear stress. Consider the equilibrium of the forces acting on the fluid within a radius r,

$$2\pi r \tau_{12} = -\pi r^2 \partial_x p = \frac{2\pi\tau_w}{R} r^2, \tag{6.26}$$

where τ_{12} is the total shear stress at radius r, and τ_w is the stress at the wall. It follows that

$$\tau_{12} = \tau_w (1 - x_2/R), \tag{6.27}$$

If the Reynolds number is high enough, the viscous contribution is negligible except in the immediate neighbourhood of the wall, and $\tau_{12} \approx -\langle \widetilde{u}_1 \widetilde{u}_2 \rangle$ almost everywhere. It then makes sense to use the friction velocity, defined by $u_\tau^2 = \tau_w$, as a scale for the velocity fluctuations and for the differences in the mean velocity. The latter is based on the idea that the mean velocity gradient is due to the large turbulent eddies whose intensity we have just seen to be $O(u_\tau)$. The same scaling applies very near the wall, where the Reynolds stresses go to zero, and the viscous expression of the wall stress, $\tau_w = \nu \partial U/\partial x_2$, is equivalent to

$$U/u_\tau = x_2 u_\tau/\nu. \tag{6.28}$$

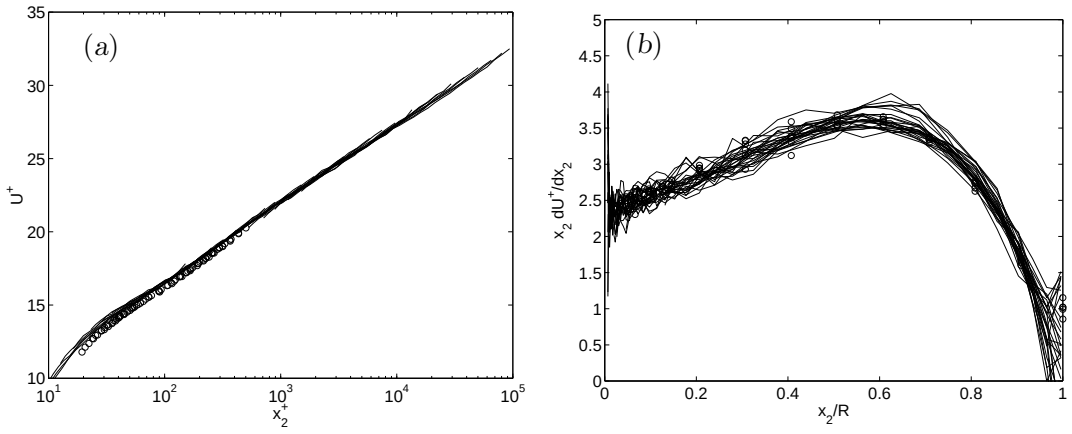

Figure 6.8: The logarithmic velocity profile in smooth pipes. (a) Mean velocity in wall scaling, $x_2/R < 0.2$; (b) Inverse of the Kármán constant in outer scaling. ——— , $Re_\tau = 1,700 - 10^6$, Zagarola & Smits (1997); ∘ , $Re_\tau = 1,600 - 3,900$, Perry, Henbest & Chong (1986).

The right-hand side of this equation is a Reynolds number based on the distance to the wall, and introduces a viscous length scale $\delta_\tau = \nu/u_\tau$. Quantities normalized with u_τ and δ_τ are said to be in 'wall units', and are denoted by a $^+$ superscript, so that (6.28) is written $U^+ = x_2^+$. Wall scaling is essentially the same as Kolmogorov's, since $\delta_\tau \approx \eta$ at the wall. The friction Reynolds number, $Re_\tau = u_\tau R/\nu$, is equivalent to the large-scale Reynolds number Re_L used for isotropic turbulence.

The presence of two length scales, δ_τ and R, makes the velocity profile inhomogeneous. Although they are the same lengths as the Kolmogorov and integral scales in homogeneous turbulence, the wall segregates them in space as well as in size. We can think of the core of the pipe as 'normal' turbulence, with a full cascade and a full range of length scales. As we approach the wall, however, the large scales don't 'fit' anymore, and only the Kolmogorov range is left.

In between these two extremes there is an overlap region, where $x_2^+ \gg 1$ and $x_2/R \ll 1$, in which some of the large eddies are present, while others are excluded by the wall. In the classical picture the only possible length scale in this region is x_2, and the mean velocity profile is logarithmic. There are several arguments that lead to this conclusion, but the following is specially instructive. It follows from (6.27) that, in this region, $\tau_{12} \approx u_\tau^2$. Assume as a first approximation the integral length of the largest eddies that participate in the cascade at wall distance x_2 is $K_a x_2$, and that their characteristic velocity is $u' \approx u_\tau$. Assume also that the local energy transfer rate is given by the Kolmogorov argument as $u_\tau^3/K_a x_2$, is in equilibrium with the production. This gives a differential equation for U,

$$\Pi = u_\tau^2 \frac{\partial U}{\partial x_2} = \frac{u_\tau^3}{K_a x_2}, \tag{6.29}$$

which can be immediately integrated to

$$U^+ = \frac{1}{K_a} \log x_2^+ + A. \tag{6.30}$$

The Kármán constant K_a is universal, essentially related to the dynamics of the cascade, and has been measured in different wall flows to be $K_a \approx 0.4$. The additive constant A depends on the details of the flow near the wall, because (6.29) is only valid when $x_2^+ \gg 1$, and cannot be extended to satisfy the wall boundary condition. Its experimental value for smooth walls is $A \approx 5$, but it may change by orders of magnitude if the wall is rough, or by the effect of certain manipulations of the near-wall region.

Comment 6.3: An alternative derivation of (6.30) is based on using an eddy viscosity. The simplest form of the argument is that, in a region of the flow which is too near the wall for the pipe radius to be important, and too far for viscosity to be relevant, the only available velocity and length scales are u_τ and x_2. This can for example be used to argue that the eddy-viscosity has to have the form

$$\nu_\varepsilon = K' u_\tau x_2. \tag{6.31}$$

The momentum equation (6.27) then reduces to

$$\tau_{12} = u_\tau^2 = \nu_\varepsilon \partial_2 U_1, \tag{6.32}$$

which can be integrated directly to obtain the logarithmic law (6.30), and which shows that K' is identical to the Kármán constant K_a.

The integration of (6.32) cannot be used to impose the no-slip condition $U_1(0) = 0$, because the assumptions that lead to (6.31) are not valid near the wall. A slightly better model, that can in principle be carried to the wall, and which therefore allows the computation of the additive constant A in (6.30), is given in the next chapter as part of comment 7.1.

The contrast with free-shear flows is clear; in problem 6.1 we were able to use a single length scale for the eddy viscosity across the full flow thickness, because the same (large) structures were dominant across the whole flow. Here, in a more inhomogeneous situation, that is no longer possible.

Figure 6.8 shows that the logarithmic profile is very well satisfied experimentally, approximately between $x_2^+ > 100$ and $x_2/R < 0.2$. Those limits have been overlaid in figure 6.7, showing that most of the velocity drop occurs in the near-wall layer, and that the core of the pipe is in reality a very weak shear flow.

A rough estimate of u_τ can be obtained by extrapolating (6.30) to the centre of the pipe,

$$\frac{U_{max}}{u_\tau} = U_{max}^+ = \frac{1}{K_a} \log Re_\tau + A. \tag{6.33}$$

Because of the logarithmic dependence on the Reynolds number, the velocity at the centreline does not change much, and is always $U_{max}/u_\tau \approx 20 - 30$. Of this velocity difference, the drop in the near-wall viscous layer below $x_2^+ = 100$ is already $U/u_\tau = 16$. The logarithmic law can be integrated across the pipe to estimate the bulk velocity U_b, whose value is directly related to the friction coefficient used in the introduction, which can be written as

$$c_f = \frac{\tau_w}{\frac{1}{2} U_b^2} = \frac{2 u_\tau^2}{U_b^2} = \frac{2}{U_b^{+2}}. \tag{6.34}$$

	Scales	Profile	Limits
Near-wall	u_τ, δ_τ	$U^+ = x_2^+$	$x_2^+ < 100$
Overlap	u_τ, x_2	$U^+ = K_a^{-1} \log x_2^+ + A$	$x_2 \ll R$ and $x_2^+ \gg 1$
Core	u_τ, R	$U^+_{max} - U^+ = f(x_2/R)$	$x_2/R > 0.1 - 0.2$

Table 6.1: Classical scaling of wall flows.

The result is also a slow logarithmic dependence of c_f with the Reynolds number.

Problem 6.4: The logarithmic law (6.30) can be approximately used in pipes well beyond the overlap region towards the centre of the pipe. Use this approximation to compute the mean velocity

$$U_b^+ = \frac{2}{R^2} \int_0^R r U_1^+ \, \mathrm{d}r,$$

as a function of the Reynolds number $Re = U_b R/\nu$. Relate this quantity to the friction coefficient defined in chapter 1, and solve numerically the resulting implicit transcendental equation, to find $c_f(Re)$. Compare the results of your approximation with the experimental values in figure 1.1, which can be found in the web site `ftp://torroja.dmt.upm.es/polyturb/chap1/`. The friction coefficients for rough pipes are in the files `niku*.dat`, and those for smooth pipes are in `zaga.dat`. The same approximation works less well for boundary layers and for other external flows, because the logarithmic velocity does not apply in the external region where the flow is only partly turbulent.

In the classical view the near-wall viscous layer corresponds to the dissipative range of scales of isotropic turbulence, the core plays the role of the energy-containing eddies, and the logarithmic region that of the inertial range, but the analogy is not complete. In the isotropic case the small scales are net recipients of energy, which they dissipate. The wall region is different. Because the mean velocity gradient is highest near the wall, the production of turbulent energy has a very sharp maximum there (figure 6.7.*b*). Even when the dissipation, which is also maximum near the wall, is taken into account, the region below $x_2^+ \approx 30$ is a net source of turbulent energy, which it exports to the rest of the flow as a spatial energy flux. Other parts of the flow, specially the centre of the pipe, where $\Pi = 0$ because $\partial U/\partial x_2 = 0$, are energy sinks. The global balance is between energy generated near the wall at the Kolmogorov scale, which is transported across the logarithmic layer to the large-scale eddies in the centre of the pipe, and which is finally dissipated there by the local, isotropic, Kolmogorov cascade. This spatial inverse cascade is a relatively small fraction (10–15%) of the classical, quasi-isotropic, local energy production and dissipation but it is crucial in maintaining turbulence in the core of the flow.

A summary of the classical scalings and velocity laws for the different layers is given in table 6.1.

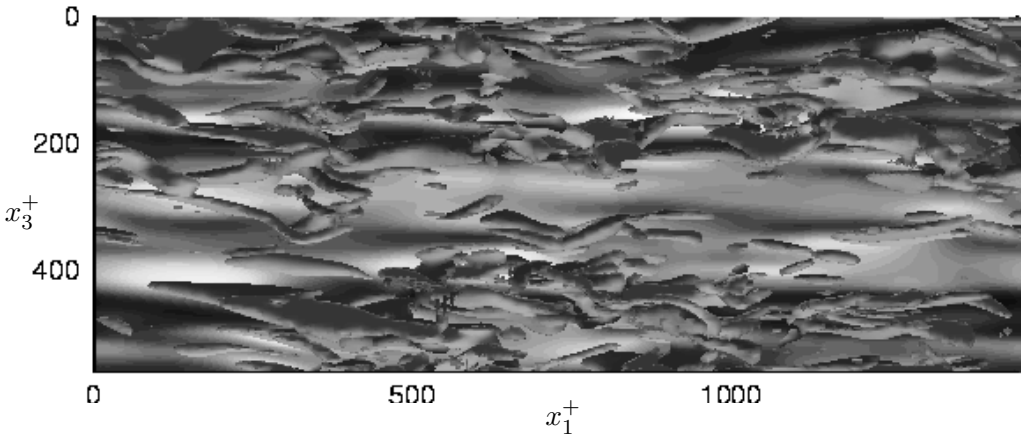

Figure 6.9: Structures in the wall region of a plane turbulent channel. The view is from the interior of the channel into the wall, with the flow from left to right. The shades of gray in the background are $\partial_{x_2} u_1$ at the wall, and may be used as a measure of the streamwise velocity near the wall. Dark regions label low shear, and therefore the low velocity streaks. The shaded three-dimensional objects are isosurfaces of streamwise vorticity $\omega_1 = \pm 0.2$. Only the region below $x_2^+ = 80$ is represented. Axes are labelled in wall units. $Re_\tau = 180$. Numerical simulation by A. Pinelli and M. Uhlmann.

6.2.1 *Flow structures*

In parallel to the statistical information discussed above, a lot is known about the dynamical structures of wall flows.

The best understood region is that very near the wall, below $x_2^+ \approx 100$, where viscosity is important and the flow, if not laminar, is at least relatively smooth. As we have said above, this layer is roughly equivalent to the dissipative range in the cascade, but acts as a source, rather than as a sink, of turbulent energy. It is dominated by two types of structures: streamwise velocity streaks, and quasi-streamwise vortices (figure 6.9). The former were first recognized by Kim, Kline & Reynolds (1971), and are long ($x_1^+ \approx 1000$) sinuous arrays of alternating streamwise jets superimposed on the mean shear, with an average spanwise separation $x_3^+ \approx 100$. At the spanwise locations where the jets point forward, the wall shear is higher than the average, while the opposite is true for the 'low velocity' streaks where the jets point backwards. The quasi-streamwise vortices are slightly tilted away from the wall, and each one stays in the near-wall region only for $x_1^+ \approx 200$. Several vortices are associated with each streak, with a longitudinal spacing of the order of $x_1^+ \approx 400$. Some of the vortices are connected to the trailing legs of coherent vortex arches (hairpins) which are present in the outer part of the boundary layer, but most merge into disorganised vorticity after leaving the immediate wall neighbourhood.

It is known that the vortices cause the streaks by deforming the mean velocity gradient, moving high-speed fluid towards the wall and low-speed fluid away from it. There is less agreement on the mechanism by which the vortices are produced,

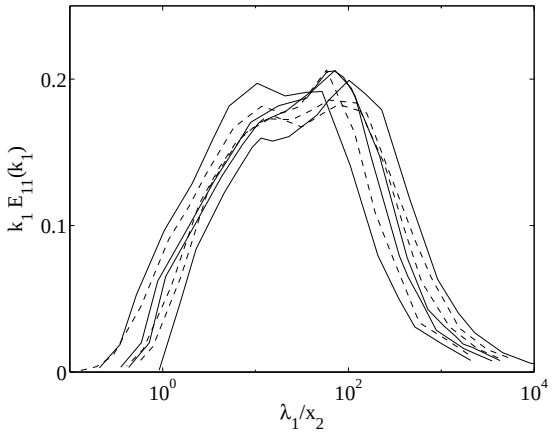

Figure 6.10: Premultiplied longitudinal energy spectra in the logarithmic region of smooth pipes. Note that the abscissae are normalized with the distance to the wall, and that the κ_1^{-1} part of the spectrum, which in this representation appears as approximately constant, is always at wavelengths $\lambda_1 = 2\pi/\kappa_1$ which are much longer than the distance to the wall. Note also that most of the energy in the spectra, which is the area underneath the plots, is contained in that region. —— , $Re_\tau = 4900$; ---- , $Re_\tau = 2300$. Data from Perry & Abell (1977).

but it is generally believed that they are the result of the instability of the streaks, thus creating a closed turbulence generation cycle near the wall. The details of the near-wall cycle itself have been increasingly clarified in recent years, specially through the analysis of numerical simulations. It is for example known that the cycle is an autonomous feature of the wall region, able to generate turbulent fluctuations without the assistance of the core, and this part of the flow has been the target of several attempts to decrease the friction drag by damping the structures just described.

The other interesting region is the logarithmic layer. What makes it different from other turbulent flows is the presence of so-called 'inactive' motions (Townsend 1967), which are large in the directions parallel to the wall, but which are forced by the impermeability of the wall to be much thinner in the wall-normal direction. It is clear that these modes may be very anisotropic, and that the normal Kolmogorov cascade may not work for them. Since they are much longer than x_2, while we have seen that the logarithmic profile can be written as a balance between the instability of the eddies of size x_2 and the local energy production, these eddies are too slow to participate in that process. They reside *above* the normal energy cascade, which is only carried by eddies which are smaller than x_2. On the other hand, being very anisotropic, they carry Reynolds stresses, and they are the seat of the spatial inverse cascade mentioned above. This can be used to estimate their energy spectrum, which is different from Kolmogorov's. The dimensional argument is the following. Near the wall, and outside the Kolmogorov isotropic regime, the conserved quantity is the Reynolds stress u_τ^2, and the spectrum can only depend on it, on the wavenumber

κ_1, and possibly on x_2 and R. But if we concern ourselves only with scales which are much longer than x_2 and much shorter R, neither x_2 nor R may therefore enter the spectrum, and the only possible combination is

$$E_{11}(\kappa_1) \sim u_\tau^2 \kappa_1^{-1}. \tag{6.35}$$

The κ^{-1} spectrum is observed in most wall flows for $\kappa_1 x_2 \ll 1$, and has been carefully documented by Perry, Henbest & Chong (1986) (see figure 6.10). Note that the argument only works if $x_2/R \ll 1$, and coincides in space with the logarithmic region. In fact, the κ_1^{-1} spectrum, the logarithmic similarity profile, and the inverse spatial cascade, are different aspects of the same phenomenon. Note also that, since κ^{-1} is not integrable near $\kappa = 0$, this spectral range contains most of the fluctuating turbulent energy.

These eddies are responsible for a significant difference between wall-bounded and other turbulent flows. In most other cases the integral scale is uniform across the flow, and the eddies not subject to Kolmogorov scaling are only those which are larger than a given fraction of L_ε. The number of non-Kolmogorov modes per integral volume is therefore $O(1)$, and it could be argued that the only role of a theory of those flows is to understand the isotropic cascade, which contains a potentially infinite number of degrees of freedom as $Re \to \infty$. The number of large-scale modes is always finite, and can in principle be handled by sufficiently powerful numerical simulations.

The situation near walls is different. The integral scale is $L_\varepsilon \sim x_2$, and all the modes larger than x_2 are anisotropic. The number of those modes in a volume $R^2 \mathrm{d}x_2$ is $\mathrm{d}N \sim R^2 \mathrm{d}x_2/x_2^3$. Integrating between $x_2 = \delta_\tau$ and R, the total number of non-Kolmogorov modes in a volume R^3 is

$$N \sim Re_\tau^2, \tag{6.36}$$

which is infinite in the high-Reynolds number limit, and only slightly smaller than the total number of turbulent degrees of freedom, $N_T \sim Re_L^{9/4}$. This implies that a statistical theory is needed for the large-scale structures of wall flows, as much as for the small-scale ones, and that this theory is fundamentally different from Kolmogorov's.

Chapter 7

The numerical computation of turbulence

Summary

The important sections in this chapter are §7.2 to §7.4, which describe the three levels of detail at which turbulence is usually computed. It is difficult in such a limited space to give many details on subjects which by themselves constitute independent and interdisciplinary fields of study. The aim of the chapter can only be to familiarize the reader with the requirements of each of the three techniques and with the results that can be expected from them. The final result should at least be to allow him or her to determine which method to use in a particular situation. For a worked example of how this is done, see problem 7.2

A subject such as this cannot be discussed without some reference to numerical analysis, which is the tool used in simulation. This is specially true in the case of turbulence, where we have seen that the flow fields are not smooth, and are therefore not easy to represent numerically. The minimum information on numerics needed to understand the present chapter is summarized in a few sentences in §7.2, and it should be enough for a first reading. A slightly more detailed treatment has been collected in the two supplementary exercises 7.3 and 7.4, which are intended as a two-page 'course' on the numerical integration of evolution equations. Any reader seriously interested in computing turbulent flow should, of course, familiarize her or himself as much as possible with the details of the numerical techniques.

7.1 The reasons for computing turbulence

Although we have seen in the previous chapters that turbulence is a complex phenomenon, we have also noted that it is a natural consequence of the deterministic Navier-Stokes equations. Given the proper initial and boundary conditions, there should therefore be no difficulty in computing numerically any particular turbulent flow. In this chapter we shall see that this is only true in an abstract sense. The number of degrees of freedom of the flow is usually so large that the cost of direct

computations is high enough to make them impractical. We also saw in chapter 2 that it is not always necessary to know everything about a particular realization of a flow, and that it is in many cases more useful to consider it as a random sample from a larger set of equivalent flows, of which we only need a statistical characterization. A large part of the art of turbulence computation is therefore how to *approximate* some aspects of a turbulent flow using only limited resources, rather than how to compute the flow in detail.

Computing something does not mean understanding it, although it certainly helps, but there are fundamental reasons why being able to compute a phenomenon is important. In the first place, putting numbers in a theory is a prerequisite for making predictions. The main difference between science and philosophy is that, while the latter is generally content with giving a view of the World which is intellectually coherent and personally satisfying, the former insists on testable theories. The core of the scientific method is to develop theories, derive predictions from them, and *test* those predictions. The last step implies estimating what happens if we manipulate our system in some particular way, and it is most convincing when it is done quantitatively. Until that has been accomplished, a theory cannot be accepted as science.

We have developed in the previous chapters a 'philosophical' model of turbulence which is coherent and which explains the observations. This is a necessary first step, but we cannot be content until we have tools to compute what would happen if we changed the flow in ways which are different from those of the original experiments, and until we have checked that the results of those computations are true.

This has traditionally been difficult to do for complex systems. Classical mechanics initially concerned itself with analytic solutions. The mathematics of the motion of a rigid body are within the reach of pencil and paper calculations. We can find closed-form solutions for the motion of a cannonball, and use them to predict what would happen if we changed the angle of the shot. We can then use the confidence gained in that way to send a spacecraft to Mars with a reasonable expectation that it will get there. But even this example soon gets complicated. Without including the perturbations due to the Earth, the Sun, the Moon, and Jupiter, we would miss Mars by an impractical margin. Other apparently negligible effects, such as the pressure of the solar wind, or the differential radiation emitted by the spacecraft from its warmer sunward side compared to its cooler shaded face, are also important. Very simple systems, formed by elements which are perfectly understood, can be too complicated for analytic solutions. We saw in chapter 2 that as few as four vortices become chaotic and, even if the rules of chess are few and clear, the game is interesting precisely because we cannot analytically deduce from them which is the optimum strategy in each particular situation.

Such complex systems used to be considered games, or at most questions to be treated by engineers using rules of thumb derived from experience. They were not considered proper subjects for science, precisely because no quantitative predictions could be done from their theories.

Turbulent flows used to be in that category, and a lot of effort has been spent

in finding theoretical results that could be cast in closed form. We have referred in the previous lectures to a good fraction of the analytical results known to date, but there are not many. This failure to find simple solutions frustrated some of those working in the field, and convinced them that there was something special, and even 'mysterious', about turbulence that had to be cracked before the problem could be considered understood.

Although analytic work will always have an important place in scientific study, most obviously in providing asymptotic results for extreme values of the parameters, and in proving the generality of the results, the availability of ever more powerful computers has completely changed the classical view of what it means to understand something. Complex systems can now be simulated numerically, essentially exactly, and theories for them can be tested even when no analytic results are known. It has always been possible to test turbulence theories by doing experiments in which a parameter is changed to see whether its effects agree qualitatively with a given model. Most of the concepts introduced in the previous lectures have been confirmed in that way. But computers allow us to do more than that. We can now change the constitutive equations, and quantitatively compute the consequences. In this way we can also check whether our understanding of the importance of a particular term, or of a particular structure, is correct or not.

This of course does not mean that there is no role left for classical turbulence theory. We have already mentioned that, although numerical experiments are possible, many are too expensive to be practical. The latter include most cases of industrial interest, and simple theories are crucial in providing a bridge between what we can, and what we want to compute.

This leads us to the second reason for computing turbulence, which is technological. We noted in the introduction to these lectures that turbulent flows are extraordinarily common, and we have seen that they differ qualitatively from laminar ones. We would not be able to fly aeroplanes, or to build efficient power plants, without understanding to a good approximation what a turbulent flow does. Turbulence theories, embodied in the form of turbulence models, are the core of the approximate computational methods needed by industry, and better theories sooner of later lead to better models.

In this chapter we briefly survey the problems involved in computing turbulence, starting with 'exact' methods, which are at present used mainly for testing scientific theories, and moving towards the approximations which have to be made in industrial applications.

7.2 Direct numerical simulations

We saw in chapter 5 that one of the defining characteristics of high-Reynolds number turbulence is that the kinetic energy and the Reynolds stresses are associated with length scales which are much larger than those responsible for the energy dissipation, and that both are linked by a quasi-equilibrium inertial range which is isotropic and universal. The different strategies for computing turbulent flows differ in which

scales they compute explicitly and which ones they model.

At one end of the spectrum of computational methods is direct numerical simulation (DNS), which explicitly computes everything up to, and including, the energy dissipating scales. The velocity field is smooth at those sizes, so that derivatives and Taylor series expansions can be used, and standard numerical analysis applies. For a low-order numerical method the smallest relevant details of the functions that are being computed should have no less than five or six grid points [PROBLEM 7.3] and, since we have seen that the turbulent velocities are only smooth for distances shorter than $\approx 10\eta$ (see for example figure 1.6 in chapter 1), it follows that the grid spacing of a simulation using these methods should not be much larger than the Kolmogorov scale. Higher-order numerical schemes allow somewhat coarser resolutions, but it is shown in problem 7.3 that all differentiation formulas fail at distances shorter than two grid points, implying that the flow field should at least be smooth at those scales. When the grid spacing is shorter than those minimum requirements the accuracy of numerical schemes increases quickly, and the results of the simulations differ from the analytic ones by negligible amounts.

Note on the other hand that it would make no sense to use discrete approximations with grid spacings lying in the inertial range, since there $\Delta u \sim \Delta x^{1/3}$, and the numerical estimate of the derivative

$$\frac{\Delta u}{\Delta x} \sim \Delta x^{-2/3}, \tag{7.1}$$

does not converge as Δx decreases. This behaviour continues at least until $\Delta x \approx \eta$, at which point we are back into the sub-Kolmogorov DNS range.

With these precautions, the quality of DNS is only limited by how much one is willing to spend in resolution, domain size, and running time to collect statistics. When they can be obtained, the results of DNS are indistinguishable from laboratory experiments, and the scatter among careful simulations is generally smaller than among comparable experiments.

Unfortunately their price is high. Since the ratio between the integral and the dissipation lengths is $O(Re_\lambda^{3/2})$, the number of grid points needed to simulate a cube whose size is of the order of the integral scale is

$$N_g \sim (L_\varepsilon/\eta)^3 = O(Re_\lambda^{9/2}), \tag{7.2}$$

which determines the amount of computer storage that should be used. Direct simulations are the numerical equivalent of experiments. The flow fields are unsteady, as in real flows, and the compilation of statistics requires that they should be run at least for a few turnover times, L_ε/u', while considerations of numerical accuracy limit the time step to be shorter than the time it takes for a fluid particle to cross one grid element, $\Delta x/u'$ [PROBLEM 7.4]. The number of time steps needed is then of the order of $N_T \sim L_\varepsilon/\Delta x = O(Re_\lambda^{3/2})$, and the total number of operations is

$$N_g N_T = O(Re_\lambda^6). \tag{7.3}$$

Even for very moderate Reynolds numbers, $Re_\lambda \approx 100$, this means 10^{12} operations, and memory requirements of 10^9 variables. Other considerations, such as the need

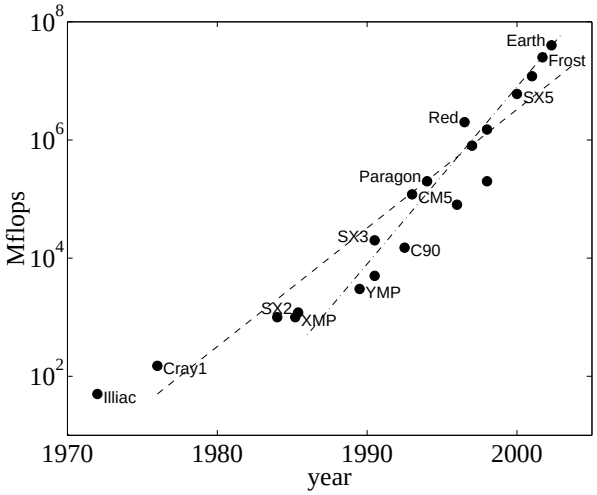

Figure 7.1: Computer speed of selected research machines as a function of year of installation. The shallower regression line is the classical growth law for single-processor machines, and doubles approximately every 18 months. The steeper one doubles every year, and has held for multi-processor parallel machines over the last twenty years. If it continues to hold in the future, it implies an increase of computer power of three orders of magnitude every decade.

for several variables per grid point and of several operations per variable, add one or two orders of magnitude.

Modern commercial computers process 10^9 floating-point operations per second (one Gigaflops), and multi-Teraflops (10^{12}) demonstration machines already exist. Petaflops (10^{15}) commercial machines are expected by the year 2020. Computer memories, measured in bytes, have traditionally been of the same order as the computing speed in flops. Simple direct simulations, with grids of a few million points, are therefore now possible. They run in a few hours on commercial computers, and in a few seconds on prototypes. They are expected to run in milliseconds in twenty years. These are reasonable times, and DNS is a very useful tool for studying simple flows at low or moderate Reynolds numbers.

Flows that have been computed directly include isotropic turbulence up to $Re_\lambda \approx 1000$, turbulent pipes and channels up to $Re_\tau \approx 2000$, and mixing and boundary layers up to similar Reynolds numbers. A review of what was possible a few year ago was given by Moin & Mahesh (1998), but Reynolds numbers have at least doubled since then.

Simulations have several advantages over laboratory experiments. An obvious one is that, once a flow has been simulated, it is completely accessible to observation, including three-dimensional views and variables which are difficult to obtain in any other way. Even more important is the possibility of simulating 'imaginary' flows, using equations and boundary conditions which differ from the real ones in almost arbitrary aspects, and allowing us to check partial processes or hypothetical mechanisms, or to test proposed control strategies. Direct simulations have already

made important contributions to turbulence research, and will undoubtedly be used increasingly as improved hardware and algorithms extend their capabilities. Many of the results in the previous chapters have either been derived or supported by direct numerical simulations.

They are however limited in scope, and are likely to remain that way for some time. Note that all the examples cited above refer to simple idealized geometries, and that geometrical complexity has to be traded for Reynolds number. The exponent in (7.3) is high, and a small increase in Reynolds number implies a large one in operation count. Industrial turbulent flows have Reynolds numbers in the range of $Re_\lambda \approx 10^3$, and atmospheric turbulence, of 10^4. Computer speed has historically increased by a factor of 10 every seven years (figure 7.1) and, assuming that the same trend continues to hold, it will take 50 years until direct numerical simulations of complete *simple* industrial flows are possible, and a century before we can tackle geophysical ones.

7.3 Large-eddy simulations

Fortunately, other strategies are available. The isotropic inertial range is more or less universal, and can be parameterized only by the energy transfer rate. If we can estimate that rate, and use it to model the effect of the inertial range, we should be able to avoid computing not only the dissipation scales, but all those which are approximately isotropic and in equilibrium. This is the principle of large eddy simulations (LES). The large scales are computed directly, and the dissipation scales, and most of the inertial cascade, are substituted by a 'subgrid' model.

Large eddy simulations are implemented in terms of filtered variables, defined as

$$\overline{u}_i = \int Q(\boldsymbol{x}-\boldsymbol{y}) u_i(\boldsymbol{y}) \mathrm{d}\boldsymbol{y}, \qquad \text{etc.} \tag{7.4}$$

where $Q(\boldsymbol{x})$ is a smoothing kernel. A common example is the 'box' filter

$$Q(x) = \begin{cases} 1/\sigma & \text{if} \quad |x| < \sigma/2, \\ 0 & \text{otherwise.} \end{cases} \tag{7.5}$$

Another one is the Gaussian filter,

$$Q(x) = \frac{1}{\sigma\sqrt{2\pi}} \mathrm{e}^{-x^2/2\sigma^2}. \tag{7.6}$$

These are essentially local averages, and the result is a local version of the Reynolds decomposition of the flow into a mean value and fluctuations. In Fourier space, smoothing filters damp the spectrum for wavenumbers $\kappa \gtrsim 1/\sigma$, while leaving lower wavenumbers relatively unaffected. Since we have seen that the higher wavenumbers are responsible in turbulent flows for the gradients and for the dissipation, while the energy resides in the lower ones, what the filtering operation does is to separate the turbulent velocity into a 'large-eddy' component containing the energy and the Reynolds stresses, and a 'sub-grid' component containing the dissipation (see figures 7.2 and 7.3).

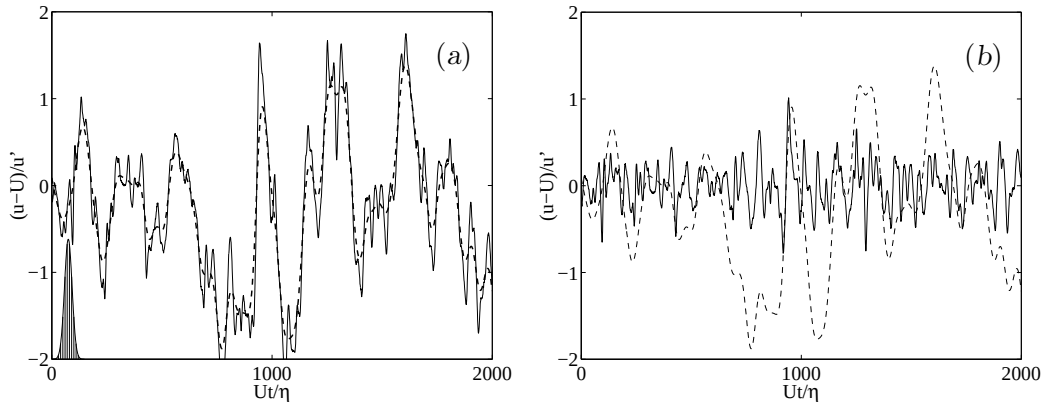

Figure 7.2: A typical turbulent velocity signal, u, and its filtered version $\overline{u}$. (a) ——— , original velocity; ---- , filtered. The filter is a Gaussian window, $Q \sim \exp(-x^2/2\sigma^2)$, with a standard deviation of $\sigma = 17\eta$, and is plotted in the bottom-left corner of the figure. (b) ---- , filtered velocity, as in (a); ——— , subgrid component, $u - \overline{u}$. Note that the subgrid components has much less energy than the filtered velocity, but contains all the short wavelengths, and therefore most of the gradients.

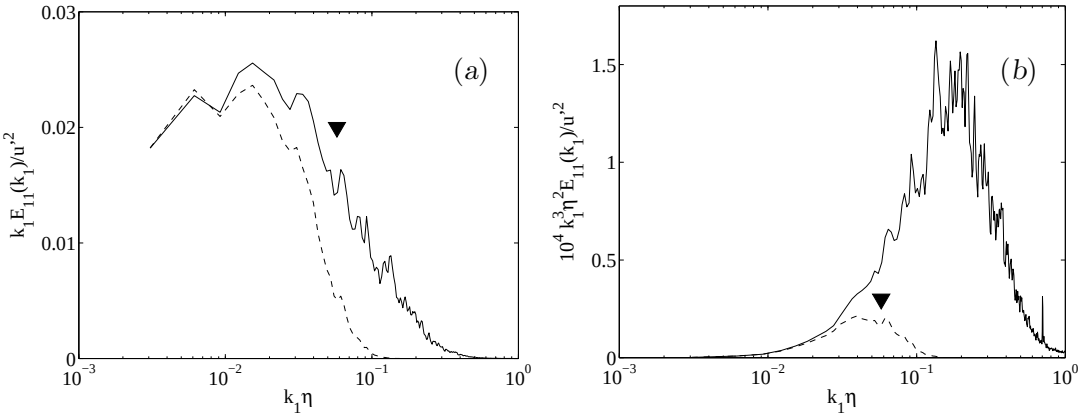

Figure 7.3: Premultiplied spectra of the filtered signal in figure 7.2 (a) Velocity. (b) Velocity gradients. Lines are as in figure 7.2, and the arrowhead marks the width of the filter $k_1 = 1/\sigma$.

Another effect of smoothing is to permit the differentiation of the filtered field, which would not have been possible otherwise in the inertial range of scales. Assume that the filter commutes with differentiation, which is strictly true only when the filter width is constant, but which is nevertheless a good approximation in most cases. Applying it to the incompressible Navier–Stokes equations, we obtain

$$\begin{gathered} \partial_t \overline{u}_i + \partial_j(\overline{u}_i\overline{u}_j) + \rho^{-1}\partial_i p^* = \partial_j(\nu\partial_j\overline{u}_i + \overline{\tau}_{ij}), \\ \partial_i \overline{u}_i = 0, \end{gathered} \tag{7.7}$$

which are similar to the Reynolds averaged equations (5.31)–(5.32) with a modified subgrid stress tensor. The latter has been separated into a trace-free component

$$\overline{\tau}_{ij} = T_{ij} - (T_{kk}/3)\delta_{ij}, \quad \text{where} \quad T_{ij} = \overline{u}_i\overline{u}_j - \overline{u_i u_j}, \tag{7.8}$$

and an isotropic one that has been absorbed into a modified pressure

$$p^* = \overline{p} - \rho\, T_{kk}/3, \tag{7.9}$$

where repeated indices imply summation. If we think of the filter as a local average, and of the velocity as separated into its smoothed part and a subgrid fluctuation, the subgrid stresses are the momentum fluxes due to the fluctuations across the 'walls' of the filter, while the correction to the pressure is the subgrid kinetic energy. The latter needs no explicit modelling. The role of pressure in incompressible flows is to insure continuity, and its only physical constraint is that the inviscid interactions between fluid particles should not involve torques, which requires that the pressure forces should be irrotational, and therefore that they should be the gradient of a scalar. Within these limits any scalar would do, and the correct pressure follows from the requirement that the velocity remains incompressible. The correction term in (7.9) is due to the difference between enforcing continuity for the true velocity field or for the filtered one and, if this is done correctly, the effective pressure is computed automatically. The true pressure only has to be computed if it is needed for some reason, such as in acoustics or in liquids involving cavitation (local boiling due to low pressures). In those cases a separate model is needed to estimate the subgrid kinetic energy in (7.9).

The divergence of the subgrid shear stresses, on the other hand, always has to be modelled. One of the most popular models was introduced by Smagorinsky (1963), and is an extension of the eddy-viscosity idea. The subgrid stresses are assumed to be proportional to the filtered rate-of-strain tensor,

$$\overline{\tau}_{ij} = 2\nu_\varepsilon \overline{S}_{ij}, \tag{7.10}$$

and the eddy viscosity is written as

$$\nu_\varepsilon = C_S \Delta^2 |\overline{S}|, \tag{7.11}$$

where Δ is a measure of width of the filter, $\overline{S}_{ij}$ is the rate-of-strain tensor computed with the filtered velocity $\overline{u}$, and $|\overline{S}|^2 = \overline{S}_{ij}\overline{S}_{ij}$. In this equation Δ has been used as the length scale for the eddy viscosity, and $|\overline{S}|^{-1}$ as a time scale. As with other eddy-viscosity formulations, there is little reason to believe that (7.10) is true, and in particular that the tensors $\overline{\tau}_{ij}$ and $\overline{S}_{ij}$ are parallel. In fact, checks on real flows show that both tensors are only weakly correlated, in spite of which (7.10) works well in many situations. The reason seems to be that all that is needed by the large scales is to have a mechanism that dissipates the correct amount of energy at the end of the cascade.

If an equation for the kinetic energy of the filtered velocities is obtained from (7.7), the product $-\Pi_S = -\overline{\tau}_{ij}\overline{S}_{ij}$ appears in the right-hand side as an energy sink.

If the Reynolds number is large, and if the filter is far enough from the Kolmogorov scale, the large-scale viscous dissipation $\nu|\nabla \overline{\boldsymbol{u}}|^2$ is negligible, and Π_S acts as a substitute for ε. The energy is transferred to the sub-grid scales, where viscosity would normally get rid of it. In the simulation, the dissipation is done by the model.

This interpretation can be used to estimate the Smagorinsky constant C_S. The dissipation is written as

$$\varepsilon = \Pi_S = 2C_S\Delta^2|\overline{S}|^3 \tag{7.12}$$

and the magnitude $|\overline{S}|$ is expressed in terms of the energy spectrum. We saw above that any filtering operation such as (7.4) is equivalent to a multiplication of the spectral tensor by a window in Fourier space which, for smoothing filters, damps the high wavenumbers. The norm $|\overline{S}|^2$ becomes a weighted integral over a neighbourhood of the origin in Fourier space which, because the spectrum of the velocity gradients increases with increasing wavenumbers, is dominated by scales whose sizes are $O(\Delta)$ (see figure 7.3). If the filter is narrow enough for those scales to be isotropic, that allows us to compute $|S|$ as a function of the filter width Δ, and of the inertial-range spectrum, which only depends on ε. When that estimate is plugged back into (7.12), the result is an equation for C_S which depends only on the filter shape. For the particular case in which the filtering operation is local averaging over a cubic box of side Δ, $C_S \approx 0.03$. In practice the filter is seldom cubical but, because we are essentially integrating a spherically symmetric spectrum over a volume in Fourier space, anisotropic filters can be used with the same value of C_S as long as we take $\Delta^3 = \Delta_1\Delta_2\Delta_3$.

In shear flows, which is where LES is really needed, the corrections due to anisotropy are fairly large, and more sophisticated strategies have been developed. The reader should consult recent reviews by Lesieur & Metais (1996) and Moin (1997) for details, as well as for successful applications. Basically LES can be used for simulations of quasi-industrial flows with non-trivial geometries. Examples that have been computed include wakes behind simple obstacles and separating flows, such as diffusers and the trailing edge of wings. There are technical problems involved in the boundary conditions near walls, but most flows in which walls are not important, such as jets, mixing layers and the injectors for combustion systems, can be simulated, essentially independent of their Reynolds number. More complicated geometries in which the Reynolds number is not too high, such as blade cascades in turbines and compressors, are also beginning to be possible.

That subgrid models work well in spite of their known shortcomings is a demonstration of the idea, which we have implicitly used up to now, of a predominantly one-directional cascade. Causality is from large to small scales, and how the energy is dissipated in the latter does not influence the former, as long as the amount is correct. An even more dramatic demonstration was given by Brachet *et al.* (1998), who experimentally generated isotropic turbulence in superfluid Helium. Dissipation in that system is not due to viscosity, but to the random reconnection of quantized vortex lines, in spite of which the energy spectrum in the inertial range was indistinguishable from the normal one, including the value of the Kolmogorov constant.

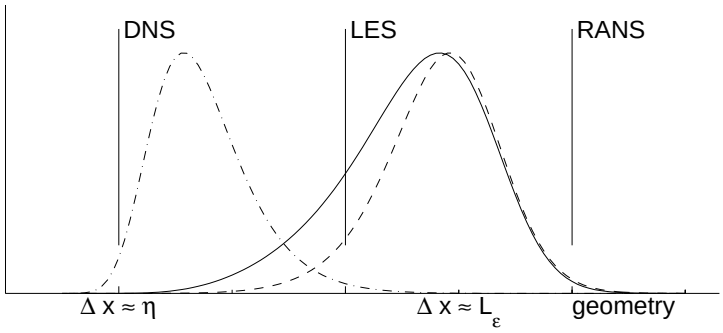

Figure 7.4: Sketch of the resolution requirements for the different simulation schemes for turbulent flows. The three curves are pre-multiplied spectra for, —— , turbulent kinetic energy; - - - - , shear stress; —·— , energy dissipation. Note that the abscissae, $\Delta x \sim \kappa^{-1}$, are plotted in the opposite direction to those in figure 5.5

It is interesting to note that, in spite of this one-directionality of the flow of causality, the cascade itself is not really one-directional. The subgrid transfer Π_S provides a definition for the point-wise energy transfer, which can be measured by explicitly filtering fully resolved simulations. The result is that the cascade is only direct (large to small) in about 60% of the points, and inverse in the rest (Piomelli *et al.*, 1991). The overall direct energy transfer is the difference between two large opposing fluxes. This is the reason for the main limitation of eddy viscosity models, including Smagorinsky's, which is that, as long as $\nu_\varepsilon > 0$ the cascade is direct everywhere. Locally negative eddy viscosities are generally forbidden by numerical considerations, and the result is that eddy viscosity models need too little stress to produce a given dissipation (Jiménez & Moser, 2000). It is therefore generally impossible to produce with them the right dissipation and the right stresses at the same time, and LES using these models only works if the filter is chosen narrow enough that just the dissipation has to be modelled. The stresses have to be carried by the resolved field.

This still makes LES a practical alternative for the computation of free-shear flows, even at very high Reynolds numbers. We saw in chapter 5 that the stresses are carried by scales which are at most one order of magnitude smaller than L_ε. Including them requires only that $\Delta \approx L_\varepsilon/10$, so that a large-eddy simulation does not need more that a few thousand grid points per cubic integral scale. While this is a large number, it is independent of the Reynolds number, and can therefore be applied equally well to research flows and to industrial ones.

7.4 Reynolds-averaged Navier–Stokes simulations

The oldest and least general scheme for computing turbulent flows is to solve directly the Reynolds-averaged Navier–Stokes (RANS) equations (5.31)–(5.32). These equations are not 'closed', because of the presence of the unknown Reynolds stresses.

It is possible to write evolution equation for those terms, but they contain triple products which cannot be expressed in term of simpler quantities, etc. This process leads to an infinite hierarchy of equations of higher moments, which has to be closed at some point with a model. We have used several times in these notes 'one-point' closures, in the form of eddy viscosities, which we have estimated in ad-hoc ways. It would be remembered that our choices were different for free-shear flows and for the wall layer, although we were able to give a-posteriori physical reasons for them in each case. This is in general the problem with RANS. Since they try to model *all* the turbulent scales, including the non-universal energy-containing ones, RANS models are not universal, and have to be adapted to the different cases.

The development of RANS models, either in the form of eddy viscosity formulas, or in the more sophisticated one of evolution equations for the Reynolds stresses, is an industry in itself, and has been quite successful in providing approximations for flows of practical interest. Good introductions can be found in the books of Launder & Spalding (1972) and Wilcox (1993).

A typical example is the popular k–ε method. It solves two 'evolution' equations: one for the fluctuating kinetic energy k, which has relatively few arbitrary assumptions, and another one for the dissipation ε, which is written in an ad-hoc way using the same structure as in the first one. The diffusion fluxes in both equations are assumed to be proportional to the gradients of the respective variables. The kinetic energy provides a velocity scale, and the dissipation a length scale. The eddy viscosity is then chosen proportional to $\nu_\varepsilon \sim k^2/\varepsilon$, which is the product of an estimated large-scale velocity, $k^{1/2}$, and of an approximation to the integral length scale $u'^3/\varepsilon \approx k^{3/2}/\varepsilon$. There are various empirical coefficients which are adjusted to give the right results for canonical flows, such as decaying turbulence, the logarithmic velocity profile, etc. (see comment 7.1). Despite the crudeness of this procedure, this model is extraordinarily successful in computing the mean velocity profiles of industrial flows, and most aeroplanes, cars, or air-conditioners have been computed, at best, using a k–ε model.

Part of the reason is that the way of adjusting the empirical coefficients is designed to give the right results for flows which are not too different from the ones used for calibration. It is an accepted procedure in RANS to use slightly different sets of coefficients for different flows, if the results are better that way. In this sense RANS models are sophisticated interpolation tables, but the best ones are based on sound physical reasoning, paying attention to such requirements as conservation properties in the non-dissipative limit, tensor invariance, etc., which go a long way towards guaranteeing the correct physics. Even if RANS is mostly seen today as an industrial device, it has a distinguished history in turbulence research, and many of the intuitive concepts of time and length scales have been honed by their application to it.

Comment 7.1: Consider the following example of the use of a RANS model in a turbulent parallel flow in which the mean velocity U depends only on the transverse coordinate x_2. From the transverse momentum equation, the pressure gradient is constant in x_2. The streamwise momentum equation is then

$$U\partial_1 U = 0 = -\partial_1 p/\rho + \partial_2[(\nu + \nu_\varepsilon)\partial_2 U], \tag{7.13}$$

where p is the effective pressure introduced in (7.9), and ν_ε is an eddy viscosity that we will derive from the k–ω RANS model. This turbulence model is a modification by Wilcox (1988) of the standard k–ε. The energy equation is the same as in the latter and, in the one-dimensional case, becomes

$$U\partial_1 k = 0 = \nu_\varepsilon(\partial_2 U)^2 - \varepsilon + \partial_2[(\nu + \nu_\varepsilon/2)\partial_2 k]. \tag{7.14}$$

Since the turbulent stress has been defined in (7.13) as $\tau = \nu_\varepsilon \partial_2 U$, the first term in the right-hand side is the production of turbulent energy, $\tau_{ij}S_{ij}$, and the second one is the energy dissipation. The third term is an empirical energy diffusion term whose justification is less obvious. Note in particular the empirical factor of $1/2$ in the eddy viscosity.

The k–ω method uses, instead of the dissipation ε, a specific dissipation per unit energy, which has units of an inverse time scale, and which is defined as

$$\omega = \epsilon/C_3 k. \tag{7.15}$$

The eddy viscosity is then written in terms of the energy and time scales as

$$\nu_\varepsilon = k/\omega. \tag{7.16}$$

The model uses an evolution equation for ω,

$$U\partial_2\omega = 0 = C_1(\partial_2 U)^2 - C_2\omega^2 + \partial_2[(\nu + \nu_\varepsilon/2)\partial_2\omega], \tag{7.17}$$

which is loosely modelled on the evolution equation for the vorticity magnitude. The constants are adjusted empirically to match different canonical experiments. Their recommended values are

$$C_1 = 0.555, \qquad C_2 = 0.075, \qquad C_3 = 0.09. \tag{7.18}$$

Consider the particular case of a wall-bounded flow, such as a pipe. Consider the region in which the distance to the wall is small enough for the pressure gradient to be neglected, but large enough for the effect of the molecular viscosity to be negligible. We saw in section §6.2 that this corresponds to the logarithmic layer, and that the momentum equation can then be approximated by

$$\tau_{12} = \nu_\varepsilon \partial_2 U = u_\tau^2. \tag{7.19}$$

It is easy to check that there exists in this limit a similarity solution to equations (7.13) to (7.16) in which

$$\partial_2 U = \frac{u_\tau}{K_a x_2}, \tag{7.20}$$

and

$$\nu_\varepsilon = u_\tau K_a x_2, \qquad \varepsilon = \frac{u_\tau^3}{K_a x_2}, \qquad k = C_3^{-1/2}u_\tau^2, \quad \text{and} \quad \omega = \frac{C_3^{-1/2}u_\tau}{K_a x_2}. \tag{7.21}$$

The expression in (7.20) can be integrated to the logarithmic velocity profile in (6.30), and K_a plays the role of the Kármán constant. The remaining equation (7.17) reduces to

$$K_a^2 = 2C_3^{1/2}\left(\frac{C_2}{C_3} - C_1\right), \quad \Rightarrow \quad K_a = 0.409,$$

which is in excellent agreement with the experimental value given in chapter 6. Before being impressed by this result, be aware that the logarithmic layer was one of the experiments used to calibrate the constants in (7.18).

Note that the previous solution does not allow boundary conditions at the wall. Those should have been the no-slip condition for the mean velocity, $U(0) = 0$, and similar no-slip conditions for the fluctuations, $k(0) = 0$, and $\partial_2 k(0) = 0$. The last one recognizes that k is a sum of squares of velocity fluctuations, and that the derivative of a square, such as $\partial_2(u^2)$, vanishes whenever $u = 0$. Both boundary conditions require that the viscosity should be included as the wall is approached.

The resolution requirements for RANS are not different, in principle, from LES, but they are quite cheaper in practice. Since all the turbulence fluctuations are included in the model, there is usually no need to consider the flow as being unsteady, and it is enough to look for equilibrium solutions. It is also not necessary to choose the grid based on the integral turbulent scales, and the resolution is solely controlled by the geometry of the flow. The geometry also controls the integral scales, so that the requirements for RANS and LES are proportional to one another, independent of the Reynolds number. But the proportionality constant may be $O(10-100)$ in each direction, for a total saving of three to six orders of magnitude. In exchange for these savings, RANS methods are ad-hoc, work poorly in non-equilibrium situations, and cannot be trusted if calibration experiments are not available.

The resolution requirements for the three simulation methods are summarized in figure 7.4, relative to the turbulence spectrum. DNS has to resolve the dissipation peak, LES the energy and stress peaks, while RANS only has to resolve the geometry.

Problem 7.2: The kinematic viscosity of air at room temperature is $\nu \approx 1.5 \times 10^{-5}\mathrm{m}^2/\mathrm{s}$, and that of water, $\nu \approx 10^{-6}\mathrm{m}^2/\mathrm{s}$. Estimate representative sizes, velocities, and Reynolds numbers for the following flows. Use in each case the smallest cross-flow dimension as an estimate for the integral scale, and express the results in terms of Re_λ. Estimate which of these flows are probably turbulent and which ones are not. Estimate in each case which is the total number of degrees of freedom which would be needed for a direct simulation, as well as the computational requirements for a large-eddy simulation and RANS.

- Your finger scratching your nose.
- Your hand clapping
- A person walking
- A car at 100 Km/h.
- A commercial aeroplane at 1,000 Km/h.
- A plastic stick, 1 mm in diameter, being used to stir coffee.
- A tea spoon used for the same purpose.
- A kitchen faucet.
- A kitchen gas burner (cold).
- The same burner at 1000°K. Remember that the kinematic viscosity of a gas at a given pressure increases with the absolute temperature roughly as $T^{3/2}$ (can you explain in a simple way why it increases?).
- An industrial power burner with a diameter of 50 cm, an exit velocity of 100 m/s, and a temperature of 500°K.
- A re-entering spacecraft at a Mach number of 25, at an altitude of 50 Km. Estimate carefully the density and temperature of the incoming flow after it has lost most of its kinetic energy in a normal shock wave in front of the craft.

Solution: Consider for example the case of a walking person. The minimum cross dimension is of the order of $0.4m$, and a typical velocity is $1m/s$. Assuming an integral scale in the wake of the order of half the cross section, $L_\varepsilon = 0.2m$, the characteristic Reynolds number is

$$Re_L \approx \frac{0.2 \times 1}{1.5 \times 10^{-5}} \approx 1.3 \times 10^4,$$

which corresponds to a microscale Reynolds number $Re_\lambda \approx 450$. This is well above the minimum threshold needed for transition to turbulence, $Re_\lambda \approx 30$. The flow should then be assumed to be turbulent, and we should estimate the Kolmogorov scale as

$$\eta = L_\varepsilon Re_\lambda^{-3/2} \approx 20\mu m.$$

DNS: Assume a direct numerical simulation in a grid surrounding the person with a box of $1m \times 1m \times 2m$. A resolution of $25\mu m$, of the order of η, would result in total number of points of the order of $40,000 \times 40,000 \times 80,000$, or 10^{14}. Since about $40,000$ time steps would be needed for a fluid particle to cross the the grid across its narrower dimension, and since at least a few crossings should be computed to collect statistics of the turbulent flow, the total number of operations would be of the order of $10^{19} - 10^{20}$. Such grids and operation counts are outside the scope present computers. Note however that a Petaflops computer, such as those expected in the next decade, should be able to process this problem in about $10^4 - 10^5 s$, which is no more than a few hours.

LES: We have seen that that the smallest structures that have to be represented in LES are of the order of $L_\varepsilon/10$, which is in this case about $2cm$. Assuming a further factor of four to provide some numerical accuracy, the grid spacing would be of the order of $5mm$. The same computational box as in the previous case now has $200 \times 200 \times 400$, or 16 million points. The crossing time would be about 200 time steps, so that the total number of time steps would not be more than a few thousands, for a total count of 10^{11} operations. This would not take more than a few minutes in a Gigaflops-class workstation.

RANS: We have seen that the resolution requirements for RANS are similar to those for LES. The numerical grid defined above for LES puts 80 points across the shoulders of the walker, which is not an unreasonably large number given the complexity of the geometry. The number of iterations needed is however smaller than in LES, since there is no need to compile statistics of the fluctuations over time. There is still a minimum number of iterations needed for the solution to converge which, for numerical reasons, is typically of the order of the maximum grid dimension. In this case it would be about 500. This results in an operation count ten times smaller than for LES, and which would be feasible in a large personal computer. Note however that, since RANS is an essentially steady approximation, the walking person should not be allowed to bend while moving.

SUPPLEMENTARY PROBLEMS

Problem 7.3: The derivative of the function $u = \sin \kappa x$ is

$$\partial_x u = \kappa \cos \kappa x.$$

Consider a numerical representation in which u is given on a discrete grid with spacing h, so that $x_j = jh$, $j = -\infty \ldots, -1, 0, \ldots \infty$, and $u_j = u(x_j)$. Consider the numerical approximation to the derivative

$$D_j^{(2)} u = \frac{u_{j+1} - u_{j-1}}{2h}.$$

Note that this formula corresponds to expanding u in Taylor series of $x - x_j$, and neglecting terms which are of order $(x - x_j)^3$. The error done by this approximation can be measured by comparing the magnitude of the real and of the approximate derivatives,

$$T_j^{(2)} = \frac{|D_j^{(2)} u|}{|\partial_x u(x_j)|}.$$

Show that $T^{(2)}$ is independent of j for all harmonic functions, and compute it as a function of κ (see figure 7.5). Show that only the range $0 \leq \kappa h \leq \pi$ has to be considered because

$$\sin(\kappa + 2\pi/h) x_j = \sin \kappa x_j,$$

for all the points of the grid, and $T^{(2)}(-\kappa) = T^{(2)}(\kappa)$.

Note from the plot of $T^{(2)}$ that this particular formula for the derivative should not be used for functions with $\kappa h > \pi/3$, which have wavelengths shorter than approximately $6h$. Generalize this observation to conclude that such *second order* derivative formulas should not be used unless

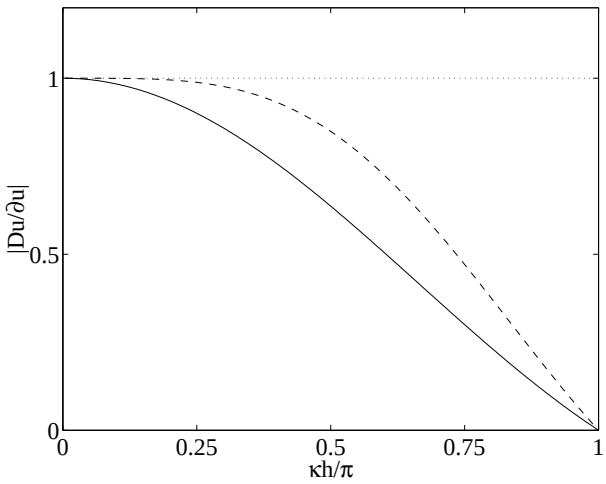

Figure 7.5: Ratio between the discrete and exact first derivatives for two numerical differentiation schemes, applied to $u = \sin \kappa x$. ····· , exact value; —— , the second-order formula discussed in problem 7.3; - - - - , the fourth-order formula, $Du = [8(u_{j+1} - u_{j-1}) - (u_{j+2} - u_{j-2})]/12h$.

all the important details of our functions are longer than approximately six grid points. Check this conclusion by numerically computing the derivatives of functions of the form

$$v(x) = \exp(-x^2/2s^2h^2),$$

for different values of the width parameter s.

The 'second order' label used above for the derivative formula refers to the behaviour of $T^{(2)}$ for smooth functions in which $|\kappa| \ll 1$, where $T^{(2)} = 1 - O(\kappa^2)$.

It is possible to construct 'higher order' numerical schemes for which the error for smooth functions is smaller than κ^2 (figure 7.5). Show however that, for any fully antisymmetric formula such as the one considered above, the numerical derivative vanishes in the limiting case $\kappa h = \pm\pi$. The error for short waves is therefore always large, and the use of finite difference formulas of this type implies that the details of the function have to be at least longer than two grid points (this requirement is sometimes called the Nyquist criterion). Show that formulas which are not antisymmetric, in the sense that the coefficient of u_{j-m} is not minus the coefficient of u_{j+m}, distort not only the amplitude but also the phase of the derivative.

Problem 7.4: The temporal equivalent of the spatial smoothness requirement discussed in the previous problem is that the time evolution of the solutions to our equations should be smooth with respect to the time step. Consider for example the ordinary differential equation

$$\frac{\mathrm{d}u}{\mathrm{d}t} = \mathrm{i}\sigma u,$$

where σ is real. Its solution is $u = \mathrm{e}^{\mathrm{i}\sigma t}$, save for an arbitrary amplitude. Discretize the solution with a time step τ, so that it is defined as $u_k = u(t_k) = u(k\tau)$, and approximate the equation by

$$\frac{u_{k+1} - u_k}{\tau} = \mathrm{i}\sigma u_k.$$

Show that the solution of the discrete equation is $u_k = (1 + \mathrm{i}\sigma\tau)^k$. The error committed by this numerical approximation can be measured by the ratio

$$\frac{1 + \mathrm{i}\sigma\tau}{\mathrm{e}^{\sigma\tau}},$$

in which the denominator is the value of u_{k+1}/u_k in the solution of the exact equation, and the numerator is the one obtained by the numerical approximation. Analyze this ratio, and observe that the error is small only if $\sigma\tau \ll 1$, and that the discrete approximation corresponds to expanding u as a Taylor series of $t - t_k$, and neglecting second order terms. Intuitively, the requirement that $\sigma\tau$ should be small means that the function should change only little during the time step.

Consider next the advection equation

$$\partial_t u + c\,\partial_x u = 0,$$

which is a linear 'model' for the Euler equations, and whose solution is $u = F(x - ct)$, for any arbitrary function F. Consider the discrete approximation

$$\frac{u_{j,k+1} - uj,k}{\tau} + c\,\frac{u_{j+1,k} - u_{j-1,k}}{2h} = 0,$$

where $u_{j,k} = u(x_j,\, t_k)$, and analyze it in terms of the Taylor series expansion of u in $x - x_j$ and $t - t_k$. Prove that, for the error to be small, it should both be true that F is a smooth function at the scale h, and that

$$\frac{c\tau}{h} \ll 1.$$

This dimensionless ratio is usually called the CFL number (after the mathematicians Courant, Friedrich and Lewis, who first noted its importance). The requirement that the CFL number should be small implies that the solution should not move more than a fraction of the spatial grid spacing in one time step. As with the approximate derivatives of the previous problem, better numerical methods allow longer time steps for a given error, but in no case can the CFL be very large if the error is to be kept small.

Appendix A

Fourier analysis

In this section we will assume that all functions are defined in a segment $x \in (0,\, L)$, or in an equivalent region in three-dimensional space, and that they extend periodically outside it. The extension to functions defined over all space involves the theory of distributions, but is essentially straightforward; a useful introduction is given by Lighthill (1958). Functions can be considered vectors of infinite dimension, and we will represent them in bold face when doing so but, whenever calculations are done, they have to be expressed in terms of their components with respect to some basis. The most common one is the 'collocation' basis, in which functions are described by their values at each point, $f(x)$. Other bases are formed by infinite sequences of vectors (functions) and the most useful are those which are orthonormal with respect to some properly defined inner product, such as

$$\boldsymbol{f} \bullet \boldsymbol{g} = \frac{1}{L} \int_0^L f(x) g^*(x)\, \mathrm{d}x, \tag{A.1}$$

where the asterisk stands for complex conjugation, and which is a natural generalisation of the familiar formula of vector analysis, $\boldsymbol{f} \bullet \boldsymbol{g} = \sum f_i g_i^*$. A basis formed by the functions $\boldsymbol{\phi}^{(j)}(x)$ is called orthogonal if it satisfies

$$\boldsymbol{\phi}^{(i)} \bullet \boldsymbol{\phi}^{(j)} = |\boldsymbol{\phi}^{(i)}|^2 \delta_{ij}, \tag{A.2}$$

where the Kronecker delta is defined as $\delta_{ij} = 1$ if $i = j$, and zero otherwise (repeated indices do not imply summation in this appendix). This definition generalizes the usual one for sets of orthogonal vectors, and the length of $\boldsymbol{\phi}^{(i)}$ is defined as

$$|\boldsymbol{\phi}| = (\boldsymbol{\phi} \bullet \boldsymbol{\phi})^{1/2}. \tag{A.3}$$

If all the vectors in the basis have unit length, the basis is called orthonormal. If we express a function in an orthonormal basis,

$$\boldsymbol{f} = \sum_j f_j \boldsymbol{\phi}^{(j)}, \tag{A.4}$$

it follows from taking the inner product with any of the basis functions that the coefficients are the inner products of the function with the basis. In Cartesian geometry,

this rule is the familiar one that the component of a vector along a coordinate axis is its projection along it,

$$\boldsymbol{f} \bullet \boldsymbol{\phi}^{(i)} = \sum_j f_j \, \boldsymbol{\phi}^{(j)} \bullet \boldsymbol{\phi}^{(i)} = \sum_j f_j \delta_{ij} = f_i. \tag{A.5}$$

A very useful basis is formed by the complex exponentials

$$\phi^{(k)}(x) = \exp(2\pi \mathrm{i} kx/L), \qquad k = 0, \, 1, \ldots, \tag{A.6}$$

which are periodic with period L, and orthonormal with respect to (A.1). The expressions (A.4) and (A.5) define then the

Fourier series and inversion formulas:

$$u(x) = \sum_{k=-\infty}^{\infty} \hat{u}_k \exp(2\pi \mathrm{i} kx/L), \quad \Rightarrow \quad \hat{u}_k = \frac{1}{L} \int_0^L u(x) \exp(-2\pi \mathrm{i} kx/L) \, \mathrm{d}x. \tag{A.7}$$

If $u(x)$ is a real function, its Fourier coefficients are complex, but they satisfy the symmetry relation

$$\hat{u}_{-k} = \hat{u}_k^*, \tag{A.8}$$

and it is customary to work only with the components $k \geq 0$.

If the inner product of two functions is expanded in terms of their coefficients using (A.2), we obtain Parseval's formula

$$\boldsymbol{u} \bullet \boldsymbol{v} = \frac{1}{L} \int_0^L u(x) v^*(x) \, \mathrm{d}x = \sum_{k=-\infty}^{\infty} \hat{u}_k \hat{v}_k^*, \tag{A.9}$$

which is often used to express the norm of the function

$$\frac{1}{L} \int_0^L |u(x)|^2 \, \mathrm{d}x = \sum_{k=-\infty}^{\infty} |\hat{u}_k|^2. \tag{A.10}$$

This is the generalisation to infinite dimensions of the classical result (Pythagoras' theorem) for the length of a vector in terms of its components, applied in two different systems of coordinates. Because the left hand side of (A.9) is the average 'power' of the function u, the square of the norm of the Fourier coefficients is sometimes called the 'power' spectrum. There is some confusion in the use of this term, since the kinetic energy is $u^2/2$, and the convention is sometimes to use the name power spectrum for

$$E_0 = |\hat{u}_0|^2, \qquad E_k = 2|\hat{u}_k|^2, \quad \text{for} \quad k \neq 0, \tag{A.11}$$

and to reserve the term 'energy', and the $1/2$ factor, for the three-dimensional spectrum that will be defined later. We will not follow here that naming convention, which originates from electrical engineering, but we will keep the definition (A.11) for the one-dimensional energy spectrum, and use the $1/2$ factor only for the three-dimensional one. Note that the definition (A.11) only makes sense for real functions,

and that an extra factor of two has been incorporated in all harmonics, except $k = 0$, to obtain a formula which involves only the nonredundant non-negative wavenumbers,

$$\frac{1}{L}\int_0^L |u(x)|^2 \,\mathrm{d}x = \sum_{k=0}^{\infty} E_k. \tag{A.12}$$

Another useful application of Parseval's theorem is the derivation of inversion formulas for the energy spectrum. It is clear from (A.7) that the Fourier coefficients for $u(x+\ell)$ are $\hat{u}_k \exp(2\pi \mathrm{i} k\ell/L)$, and it follows from (A.9) that

$$\frac{1}{L}\int_0^L u(x+\ell)u^*(x)\,\mathrm{d}x = \sum_{k=-\infty}^{\infty} |\hat{u}_k|^2 \exp(2\pi \mathrm{i} k\ell/L), \tag{A.13}$$

which shows that the Fourier transform of the correlation function is the energy spectrum.

Although the form of Fourier analysis that we have given here is the one used most often in the manipulation of physical data defined over finite domains, the same results can be expressed in ways which are free from the assumption of periodicity.

Consider the limit $L \to \infty$. The difference between consecutive wavenumbers in the Fourier series tends to zero, and it is convenient to define a continuous variable κ instead of the discrete index k. The Fourier series then becomes an integral and, if

$$\int_{-\infty}^{\infty} |u(x)|^2 \,\mathrm{d}x, \tag{A.14}$$

exists, we can dispense with L, and the previous formulas become an

Integral Fourier transform:

$$u(x) = \int_{-\infty}^{\infty} \hat{u}(\kappa) \exp(\mathrm{i}\kappa x)\,\mathrm{d}\kappa, \quad \Rightarrow \quad \hat{u}(\kappa) = \frac{1}{2\pi}\int_{-\infty}^{\infty} u(x)\exp(-\mathrm{i}\kappa x)\,\mathrm{d}x, \tag{A.15}$$

where the correspondence with the previous section is

$$\kappa \Leftrightarrow \frac{2\pi k}{L}, \qquad \hat{u}(\kappa) \Leftrightarrow \frac{L}{2\pi}\hat{u}_k \tag{A.16}$$

Parseval's formula becomes

$$\int_{-\infty}^{\infty} u(x)v^*(x)\,\mathrm{d}x = 2\pi \int_{-\infty}^{\infty} \hat{u}(\kappa)\hat{v}^*(\kappa)\,\mathrm{d}\kappa, \tag{A.17}$$

Although this formulation is widely used in mathematics, it is not very useful for the analysis of statistical series, which are conceptually infinite in time, and are not square-integrable. It is easy to see, for example, that the Fourier transform of a pure sine wave is a delta function. Parseval's formula, which is the basis for spectral analysis, becomes then ambiguous, since singular distributions have no square.

Spectral transform:

The formulation used in these notes is intended for the case in which the functions are not integrable, but where integrals such as (A.12) and (A.13) can be interpreted as averages taken over long segments (or large volumes),

$$\langle f \rangle = \lim_{L\to\infty} \frac{1}{L} \int_0^L f(x)\,\mathrm{d}x. \tag{A.18}$$

The emphasis is then not so much in providing a nice–looking transform pair, but in a formulation giving a simple expression for Parseval's theorem. The correspondence with the Fourier series is then

$$u(x) = \lim_{L\to\infty} \left(\frac{2\pi}{L}\right)^{1/2} \sum_{-\infty}^{\infty} \hat{u}(\kappa_k) \exp(\mathrm{i}\kappa_k x), \tag{A.19}$$

$$\hat{u}(\kappa) = \lim_{L\to\infty} \frac{1}{(2\pi L)^{1/2}} \int_0^L u(x) \exp(-\mathrm{i}\kappa x)\,\mathrm{d}x, \tag{A.20}$$

where

$$\kappa_k = \frac{2\pi k}{L}, \qquad \hat{u}(\kappa) \Leftrightarrow \left(\frac{L}{2\pi}\right)^{1/2} \hat{u}_k \tag{A.21}$$

Parseval's formula and its applications become

$$\langle u(x) v^*(x) \rangle = \int_{-\infty}^{\infty} \hat{u}(\kappa)\hat{v}^*(\kappa)\,\mathrm{d}\kappa, \tag{A.22}$$

$$R(\ell) = \langle u(x+\ell) u^*(x) \rangle = \int_{-\infty}^{\infty} |\hat{u}(\kappa)|^2 \exp(\mathrm{i}\kappa\ell)\,\mathrm{d}\kappa. \tag{A.23}$$

It is in this form, rather than as in (A.10), that the spectrum is usually defined,

$$E(\kappa) = 2|\hat{u}(\kappa)|^2, \quad \text{so that} \quad \langle |u(x)|^2 \rangle = \int_0^{\infty} E(\kappa)\,\mathrm{d}\kappa. \tag{A.24}$$

Equation (A.23) can then be inverted to

$$E(\kappa) = \frac{1}{\pi} \int_{-\infty}^{\infty} R(\ell) \exp(-\mathrm{i}\kappa\ell)\,\mathrm{d}\ell = \frac{2}{\pi} \int_0^{\infty} R(\ell) \cos(\kappa\ell)\,\mathrm{d}\ell, \tag{A.25}$$

where the symmetry of the correlation function has been used in the second part of the equation.

The reader should be aware that the theory of Fourier transforms is more general than the simple limits defined here, and she should consult some of the many books on the subject to get a full feeling of its flavour. The form presented here is however enough for our purpose.

A final form of the Fourier transform is given next for completeness. It is used in numerical analysis and signal processing, where functions are only defined at discrete points on a uniform grid, and where all records are finite.

Discrete Fourier transform:

Consider a function described by its values u_j at N points, which are assumed equidistant. Although it is not needed in the definitions, it helps to think of the sample points as separated in x by a uniform distance $h = L/N$. As for the Fourier series, we need to assume that the function repeats itself with period N. The functions are now vectors of finite dimension N, and the natural definition of the inner product is

$$\boldsymbol{f} \bullet \boldsymbol{g} = \sum_{j=0}^{N-1} f_j g_j^*. \tag{A.26}$$

The resulting Fourier transform pair is

$$u_j = \sum_{k=0}^{N-1} \hat{u}_k \exp(2\pi \mathrm{i} kj/N), \quad \Rightarrow \quad \hat{u}_k = \frac{1}{N} \sum_{j=0}^{N-1} u_j \exp(-2\pi \mathrm{i} kj/N). \tag{A.27}$$

Note that, except for the $1/N$ factor, this transform pair is symmetric, one of the consequences being that the Fourier coefficients should also be properly considered a periodic function of k. There are efficient algorithms (FFT, see Press *et al.* 1986) to compute both sides of (A.27), and they use this periodicity to interpret the coefficients which should correspond to $k = -\frac{N}{2} + 1, \ldots, -1$, as being identical to those located in $k = \frac{N}{2} + 1, \ldots, N-1$. That has become the standard interpretation.

Parseval's formulas become

$$\frac{1}{N} \sum_{j=0}^{N-1} u_j v_j^* = \sum_{k=0}^{N-1} \hat{u}_k \hat{v}_k^*, \tag{A.28}$$

$$\frac{1}{N} \sum_{j=0}^{N-1} u_{(j+q)} u_j^* = \sum_{k=0}^{N-1} |\hat{u}_k|^2 \exp(2\pi \mathrm{i} kq/N), \tag{A.29}$$

where the left hand sides have been put in the form of averages, and correspond directly to the integrals in the previous formulations.

The correspondence between the discrete samples and the continuous functions is

$$u_j \Leftrightarrow u(jh), \qquad \kappa \Leftrightarrow 2\pi k/L, \qquad \hat{u}_k \Leftrightarrow \hat{u}(\kappa), \tag{A.30}$$

and the power spectrum is restricted to $k \in (0,\ \frac{N}{2})$,

$$E(\kappa) = \frac{L}{2\pi} |\hat{u}_0|^2, \quad \text{if } k = 0 \text{ or } N/2 \qquad E(\kappa) = \frac{L}{\pi} |\hat{u}_k|^2, \quad \text{otherwise.} \tag{A.31}$$

Generalization to higher dimensions:

The previous discussion can easily be extended to more than one dimensions. Consider a real vector function $\boldsymbol{u}$ of an N-dimensional variable $\boldsymbol{x}$. A Fourier transform such as (A.20) is then defined as a function of the N-dimensional wavenumber $\boldsymbol{\kappa}$, and Parseval's formula becomes a relation between the correlation tensor

$$R_{ij}(\boldsymbol{\ell}) = \langle u_i(\boldsymbol{x}) u_j(\boldsymbol{x}+\boldsymbol{\ell}) \rangle, \tag{A.32}$$

where the average is now over some large volume, and a spectral density tensor

$$\Phi_{ij}(\boldsymbol{\kappa}) = \frac{1}{(2\pi)^N} \int R_{ij}(\boldsymbol{\ell}) \exp(-\mathrm{i}\boldsymbol{\kappa}\boldsymbol{\ell}) \, \mathrm{d}^N \boldsymbol{\ell}, \quad \Rightarrow \quad R_{ij}(\boldsymbol{\ell}) = \int \Phi_{ij}(\boldsymbol{\kappa}) \exp(\mathrm{i}\boldsymbol{\kappa}\boldsymbol{\ell}) \, \mathrm{d}^N \boldsymbol{\kappa}. \tag{A.33}$$

It is also useful to define, by integrating over $N-1$ components of $\boldsymbol{\kappa}$, a one-dimensional counterpart of Φ, which depends only on one component of the wavenumber, and which can be computed as a one-dimensional Fourier transform of the correlation function,

$$\Theta_{ij}(\kappa_1) = \iint \Phi_{ij}(\boldsymbol{\kappa}) \, \mathrm{d}\kappa_2 \, \mathrm{d}\kappa_3 \ldots = \frac{1}{2\pi} \int R_{ij}(\ell_1, 0, 0, \ldots) \exp(-\mathrm{i}\kappa_1 \ell_1) \, \mathrm{d}\ell_1. \tag{A.34}$$

The one-dimensional spectra defined in chapter 4 are related to these ones by

$$E_{ij}(\kappa_1) = \Theta_{ij}(\kappa_1) + \Theta_{ij}(-\kappa_1), \tag{A.35}$$

which acknowledges the symmetry of the diagonal spectra, and integrates to the correct energy over the positive wavenumbers. Note however that the cospectra, for which $i \neq j$, are not necessarily even functions of κ_1, and that the full definition (A.34) may be more useful for them.

In isotropic fields, all these quantities can be expressed in terms of a single function, $E(\kappa)$, which represents the kinetic energy contained in the wavenumber 'shell' $|\boldsymbol{\kappa}| \in (\kappa, \kappa + \mathrm{d}\kappa)$. This in done in appendix B.

Appendix B

Isotropic tensor relations

Isotropic flows are those whose statistics remain invariant to arbitrary rotations of the frame of reference. We will also assume that they are also homogeneous, i.e. independent of translations, and invariant to reflections with respect to a plane. Note that some important quantities, such as vorticity correlations, may change sign under reflection even in reflectionally symmetric fields. Isotropic vectors and tensors satisfy especial relations which simplify their analysis. For example a scalar function of the separation vector $\boldsymbol{\ell}$, such as the mean-square magnitude of the velocity increments $\langle|\boldsymbol{v}(\boldsymbol{\ell})|^2\rangle$, should at most depend of the distance, $\ell = |\boldsymbol{\ell}|$, if the flow is isotropic. We have collected here some useful relations satisfied by the statistics of velocity products of isotropic flow fields. A more detailed account can be found in the book by Batchelor (1953, §3.3–3.4), which should be consulted for the derivations, and where they are attributed to Robertson (1940). Note however that our notation is not always identical to Batchelor's and that, in particular, our discussion is based on structure functions rather than on correlations.

Consider a tensor $Q^{(m)}_{ij\ldots}$ formed from products of m vectors, such as velocities, each of which transforms under rotation in the same way as the separation vector $\boldsymbol{\ell}$. Examples could be the velocity correlation tensors or the second-order tensor structure functions of the velocity increments. Such a tensor can only depend on combinations of the components of $\boldsymbol{\ell}$ which are themselves invariant under rotation. In particular

$$Q_i(\boldsymbol{\ell}) = A(\ell)\,\ell_i, \tag{B.1}$$

$$Q_{ij}(\boldsymbol{\ell}) = A(\ell)\,\ell_i\ell_j + B(\ell)\,\delta_{ij}, \tag{B.2}$$

where δ_{ij} is the Kronecker delta and the coefficients are even functions of ℓ.

Incompressible three-dimensional turbulence:

Consider the case of the second-order velocity structure function in isotropic incompressible turbulence. It should be expressible in the form (B.2),

$$T_{ij}(\boldsymbol{\ell}) = \langle v_i v_j\rangle = \frac{F(\ell) - G(\ell)}{\ell^2}\ell_i\ell_j + G(\ell)\,\delta_{ij}, \tag{B.3}$$

where $\boldsymbol{v}(\boldsymbol{x}, \boldsymbol{\ell}) = \boldsymbol{u}(\boldsymbol{x}+\boldsymbol{\ell}) - \boldsymbol{u}(\boldsymbol{x})$ is the velocity increment, and the averaging is over $\boldsymbol{x}$. Note that F and G are respectively the second order longitudinal and transverse velocity structure functions defined in chapter 4. It follows from continuity and homogeneity that $\partial_{\ell_i} T_{ij} = \partial_{\ell_j} T_{ij} = 0$, from where it is derived that

$$G = F + \frac{\ell}{2}\frac{\mathrm{d}F}{\mathrm{d}\ell}. \tag{B.4}$$

Isotropic spectral tensors:

The relations in the previous section can also be expressed in terms of the correlation tensor $R_{ij} = \langle u_i(\boldsymbol{x}+\ell) u_j(\boldsymbol{x})\rangle$, which is related to T_{ij} by

$$T_{ij} = 2\tau_{ij} - R_{ij} - R_{ji}, \tag{B.5}$$

where $\tau_{ij} = \langle u_i u_j \rangle$ is the one-point Reynolds stress tensor. It is true for all homogeneous flows that $R_{ij}(\boldsymbol{\ell}) = R_{ji}(-\boldsymbol{\ell})$. For isotropic flows it is also true that $R_{ij}(\boldsymbol{\ell}) = R_{ij}(-\boldsymbol{\ell})$, and (B.5) simplifies to

$$T_{ij} = 2(\tau_{ij} - R_{ij}). \tag{B.6}$$

From the relations (A.33)–(A.34) in appendix A we can relate the isotropy relations given above to the spectral tensor $\Phi_{ij}(\boldsymbol{\kappa})$, and to its one-dimensional counterpart $\Theta_{ij}(\kappa_1)$. The equivalent of (B.3) is

$$\Phi_{ij}(\boldsymbol{\kappa}) = A(\kappa)\kappa_i\kappa_j + B(\kappa)\delta_{ij}, \tag{B.7}$$

and continuity requires that $\kappa_i\Phi_{ij} = \kappa_j\Phi_{ij} = 0$, giving

$$B = -\kappa^2 A. \tag{B.8}$$

The spectral tensor can then be described in terms of a single quantity which can be interpreted as the kinetic energy density per unit wavenumber

$$E(\kappa) = \frac{1}{2}\Phi_{ii}\, 4\pi\kappa^2 = -4\pi\kappa^4 A(\kappa). \tag{B.9}$$

Finally we obtain

$$\Phi_{ij}(\boldsymbol{\kappa}) = \frac{E(\kappa)}{4\pi\kappa^4}(\kappa^2\delta_{ij} - \kappa_i\kappa_j), \tag{B.10}$$

$$E(\kappa) = \kappa^3 \frac{\mathrm{d}}{\mathrm{d}\kappa}\left[\kappa^{-1}\frac{\mathrm{d}\Theta_{11}(\kappa)}{\mathrm{d}\kappa}\right], \tag{B.11}$$

$$\Theta_{22}(\kappa_1) = \frac{1}{2}\left(\Theta_{11} - \kappa_1\frac{\mathrm{d}\Theta_{11}}{\mathrm{d}\kappa_1}\right). \tag{B.12}$$

Two-dimensional turbulence:

The isotropy relations can be generalized to any spatial dimension N. Equations (B.3), (B.7) and (B.8) apply without modification, but (B.4) becomes

$$G = F + \frac{\ell}{N-1}\frac{\mathrm{d}F}{\mathrm{d}\ell}, \tag{B.13}$$

In the two-dimensional case, $N = 2$, the spectral relations become

$$\Phi_{ij}(\boldsymbol{\kappa}) = \frac{E(\kappa)}{\pi\kappa^3}(\kappa^2\delta_{ij} - \kappa_i\kappa_j), \tag{B.14}$$

$$\Theta_{11}(\kappa_1) = \frac{2}{\pi}\int_{\kappa_1}^{\infty}\frac{E(\kappa)}{\kappa^2}(\kappa^2 - \kappa_1^2)^{1/2}\,\mathrm{d}\kappa, \tag{B.15}$$

$$\Theta_{22}(\kappa_1) = -\kappa_1\frac{\mathrm{d}\Theta_{11}}{\mathrm{d}\kappa_1}, \tag{B.16}$$

although there does not seem to be in this case a clean inversion formula for (B.15), equivalent to (B.11).

References

Books

Batchelor, G.K. 1953 *The theory of homogeneous turbulence*. Cambridge U. Press.

Batchelor, G.K. 1967 *An introduction to fluid dynamics*. Cambridge U. Press.

Drazin, P.G. & Reid, W.H. 1981 *Hydrodynamic stability*, Cambridge Univ. Press.

Feller, W. 1971 *An introduction to probability theory and its applications* (second edition), vols. 1 & 2, Wiley.

Frisch, U. 1995 *Turbulence. The legacy of A.N. Kolmogorov*. Cambridge U. Press.

Launder, B.E. & Spalding, D.B. 1972 *Mathematical models of turbulence*, Academic.

Lesieur, M. 1997 *Turbulence in fluids*. Kluwer, third edition.

Lighthill, M.J. 1958 *Fourier analysis and generalised functions*, Cambridge U. Press.

Lorenz, E.N. 1993 *The essence of chaos*, Univ. of Washington Press, chapters 1–2.

Mandelbrot, B.B. 1983 *The fractal geometry of nature*, W.H. Freeman.

Monin, A.S. & Yaglom, A.M. 1975 *Statistical fluid mechanics*, MIT Press.

Ottino, J.M. 1989 *The kinematics of mixing: stretching, chaos and transport*, Cambridge University Press.

Pope, S.B.. 2000 *Turbulent flows*, Cambridge University Press.

Press, W.H., Teukolsky, S.A., Vetterling, W.T. & Flannery, B.P. 1986 *Numerical recipes*, Cambridge U. Press.

Saffman, P.G. 1992 *Vortex dynamics*, Cambridge Univ. Press. p. 241–252.

Schlichting, H. 1968 *Boundary layer theory*. McGraw-Hill, sixth edition.

Schmid, P.J. & Henningson, D.S. 2001 *Stability and transition in shear flows*. Springer.

Schroeder, M. 1991 *Fractals, chaos and power laws*, §9. W.H. Freeman.

Tennekes, H. & Lumley, J.L. 1972 *A first course in turbulence*. MIT Press.

Townsend, A.A. 1976 *The structure of turbulent shear flow*. Cambridge U. Press, second edition.

Wilcox, D.C. 1993 *Turbulence modelling for CFD*. DCW Industries.

Reviews

AGARD 1998 A selection of test cases for the validation of large-eddy simulations of turbulent flows. *Advisory Rep.* 345.

Aref, H. 1983 Integrable, chaotic, and turbulent vortex motion in two-dimensional flows. *Ann. Rev. Fluid Mech.* **15** 345–389.

Huerre, P. 2000 Open shear flows instabilities, in *Perspective in fluid mechanics* (eds. G.K. Batchelor, H.K. Moffatt and M.G. Worster) Cambridge University Press. pp. 159–229.

Jiménez, J. & Moser, R.D. 2000 LES: where are we and what can we expect? *AIAA J.* **38**, 605–612.

Lesieur, M. & Metais, O. 1996 New trends in large-eddy simulations of turbulence, *Ann. Rev. Fluid Mech.* **28**, 45–82.

Moin, P. 1997 Progress in large eddy simulation of turbulent flows, *AIAA Paper* **97–0749**.

Moin, P. & Mahesh, K. 1998 Direct numerical simulation: A tool in turbulence research, *Ann. Rev. Fluid Mech.* **30**, 539–578.

Historical References

Darcy, H. 1857 *Recherches expérimentales relatives au mouvement de l'eau dans les tuyaux*, Mallet-Bachelier, Paris.

Hagen, G. 1854 Über den Einfluss der Temperatur auf die Bewegung des Wassers in Röhren *Math. Abh. Akad. Wiss. Berlin*, 17–98.

Kolmogorov, A.N. 1941 The local structure of turbulence in incompressible viscous fluids at very large Reynolds numbers. *Dokl. Akad. Nauk. SSSR*, **30**, 301–305. Reprinted in *Proc. R. Soc. London.* A **434**, 9–13 (1991).

Kolmogorov, A.N. 1962, A refinement of previous hypotheses concerning the local structure of turbulence in a viscous incompressible fluid at high Reynolds number, *J. Fluid Mech.* **13**, 82–85. Also Obukhov, A.M. 1962 *J. Fluid Mech.* **13**, 77–81.

Rayleigh, Lord 1880 On the stability, or instability, of certain fluid motions, *Proc. London Math. Soc.* **11**, 57-70.

Reynolds, O. 1883 An experimental investigation of the circumstances which determine whether the motion of water shall be direct or sinuous, and of the law of resistance in parallel channels, *Phil. Trans. Royal Soc. London* **174**, 935-982 (Papers, ii, 51.)

Reynolds, O. 1894 On the dynamical theory of incompressible viscous fluids and the determination of the criterion, *Phil. Trans. Royal Soc. London* **186**, 123–164 (Papers, ii, 535.)

Richardson, L.F. 1922 *Weather prediction by numerical process*, Cambridge University Press.

Richardson, L.F. 1926 Atmospheric diffusion shown on a distance neighbour graph, *Proc. Royal Soc. London*, A **110**, 709–737.

Robertson, H.P. 1940 The invariant theory of isotropic turbulence, *Proc. Camb. Phil. Soc.* **36**, 209–

Smagorinsky, J. 1963 General circulation experiments with the primitive equations, *Mon. Weather Rev.* **91**(3), 99–164.

Other references cited

Brachet, M.E., Nore, C. Abid, M., Maurer, J. & Tabeling, P. 1998 Low-temperature superfluid turbulence: experimental and numerical results, in *Advances in Turbulence VII* (U. Frisch editor), Kluwer. 377–380.

Brown, G.L. & Roshko, A. 1974 On the density effects and large structure in turbulent mixing layers, *J. Fluid Mech.* **64**, 775–816.

Comte-Bellot, G. & Corrsin, S. 1971 Simple Eulerian time correlation of full and narrow-band velocity signals in grid generated 'isotropic' turbulence, *J. Fluid Mech.* **48**, 273–337.

Delville, J., Bellin, J.H. & Bonnet, J.P. 1988 Analysis of structures in a turbulent mixing layer using a pseudo-flow visualization method based on hot-wire anemometry,

in *Advances in Turbulence II*, (H.H. Fernholz and H. Fiedler, editors), Springer. 251–256. Case SHL04 in AGARD (1998).

Freymuth, P. 1966 On transition in a separated laminar boundary layer, *J. Fluid Mech.* **25**, 683–704.

Gawedzki, K. 1998 Intermittency of passive advection, in *Advances in Turbulence VII* (U. Frisch, editor), Kluwer. 493–502.

Grant, H.L., Stewart, R. W. & Moilliet, A. 1962 Turbulence spectra from a tidal channel, *J. Fluid Mech.* **12**, 241–268.

Jiménez, J. & Pinelli, A. 1999 The autonomous cycle of near-wall turbulence, *J. Fluid Mech.* **389**, 335–359.

Jiménez, J. & Wray, A.A. 1998 On the characteristic of vortex filaments in isotropic turbulence, *J. Fluid Mech.* **373**, 255–285.

Kim, H.T., Kline, S.J. & Reynolds, W.C. 1971 The production of turbulence near a smooth wall in a turbulent boundary layers. *J. Fluid Mech.* **50**, 133–160.

Kraichnan, R.H. 1971 Inertial range transfer in two- and three- dimensional turbulence, *J. Fluid Mech.*, **47**, 525–535.

Lumley, J.L. 1967 Similarity and turbulent energy spectrum, *Phys. Fluids* **10**, 855–858.

Oster, D. & Wygnanski, I. 1982 The forced mixing layer between parallel streams, *J. Fluid Mech.* **123**, 91-130.

Perry, A.E., & Abell, C.J. 1977 Asymptotic similarity of turbulence structures in smooth- and rough-walled pipes *J. Fluid Mech.* **79**, 785–799.

Perry, A.E., Henbest, S. & Chong, M.S. 1986 A theoretical and experimental study of wall turbulence. *J. Fluid Mech.* **165**, 163–199. Case PCH02 in AGARD (1998).

Piomelli, U., Cabot, W. H., Moin, P. & Lee, S. 1991 Subgrid-scale backscatter in turbulent and transitional flows, *Phys. Fluids* A **3**, 1766–1771.

Saddoughi, S.G.& Veeravali, S.V. 1994 Local isotropy in turbulent boundary layers at high Reynolds numbers, *J. Fluid Mech.* **268**, 333–372.

Saffman, P.G. 1967 The large-scale structure of homogeneous turbulence. *J. Fluid Mech.* **27**, 581–593.

Wilcox, D.C. (1988) Reassesment of the scale-determining equation for advanced turbulence models. *AIAA J.* **26**, 1299–1310.

Wray, A.A. 1997 A simulation of decaying isotropic turbulence: Case HOM02 in AGARD (1998).

Zagarola, M.V. & Smits, A.J. 1997 Scaling of the mean velocity profile for turbulent pipe flow, *Phys. Rev. Lett.* **78**, 239–242. Case PCH04 in AGARD (1998).